Lorenzo Carlo Pansana

Transmit-Receive Beamforming for 60 GHz Indoor Wireless Communications

Faculty of Electronics, Communications and Automation

Thesis submitted for examination for the degree of Master of Science in Technology.

Espoo August 6, 2010

Thesis supervisor:

Prof. Visa Koivunen

Thesis instructor:

Stefano Cervini, M.Sc.

Aalto University
School of Science
and Technology

to my Family

Lorenzo Carlo Pansana

AALTO UNIVERSITY
SCHOOL OF SCIENCE AND TECHNOLOGY

ABSTRACT OF THE
MASTER'S THESIS

Author: Lorenzo Carlo Pansana

Title: Transmit-Receive Beamforming for 60 GHz Indoor Wireless Communications

Date: August 6, 2010 Language: English Number of pages:13+87

Faculty of Electronics, Communications and Automation

Department of Electrical and Communications Engineering

Professorship: Signal Processing Code: S-88

Supervisor: Prof. Visa Koivunen

Instructor: Stefano Cervini, M.Sc.

The vast unlicensed bandwidth available in the 60 GHz band is an attractive solution to provide multi-gigabit bit-rates over short distances in indoor environments. One of the crucial problems of the 60 GHz band is the limited link budget. In order to improve the link budget, antenna beamforming techniques are employed at least at one end of the transceiver system.

This thesis studies the topic of transmit-receive (Tx-Rx) beamforming, investigating the impact of the array size and the nature of the channel (LOS/NLOS) on the system performance. The scope of the investigation is limited to uniform rectangular arrays (URA) and to analog beamforming with one scalar weight per antenna. In order to evaluate the Tx-Rx system, a multiple-input multiple-output (MIMO) Semi-Deterministic Channel Model (SDCM) is introduced, based on a combination of ray-tracing and the well-known Saleh-Valenzuela statistical model. The MIMO channel is then applied to a beamforming system based on beam-switching. With this technique, the Tx-Rx beam-vector pair that maximizes the average output SNR is selected within a codebook of pre-defined orthogonal beam-vectors spanning the whole 3-D space. The system performance is evaluated in terms of beamforming gain, coherence bandwidth of the beamformed channel, and average spectral efficiency in a band of 2 GHz.

The simulation results show that the beam-switching technique improves the system performance; the improvement is proportional to the array size and is observed both in LOS and NLOS cases (where the LOS path is obstructed). The average spectral efficiency is compared to that of an optimal beamforming scheme, showing an acceptable performance penalty. Finally, alternative analog beamforming techniques are investigated and compared against the beam-switching method. The investigation shows that within the class of analog beamforming, and for the considered channel, beam-switching is a valid cost-performance trade-off.

Keywords: 60 GHz, Beamforming, Beam-switching, MIMO, Channel Modeling, Antenna Arrays, Capacity, Ray-Tracing

Preface

This thesis is the result of a 12-month research project carried out in the AST (Advanced System Technology) section of STMicroelectronics S.p.a., Agrate Brianza, Italy. I would like to thank AST R&D for providing facilities and nice atmosphere throughout the period of my project. My thanks go especially to my instructor Stefano Cervini for his patience and perseverance in tutoring me, and to my team-mates Alessandro Tomasoni, Fabio Osnato, Teo Cupaiuolo, Massimiliano Siti, Daniele Lo Iacono, Ermano Picco and Raffaele Riva for their support. I am also very grateful to the interns Andrea Agnoletto, Alessandro Morabito and Luigi Andolfi for their good humour and friendship that cheered me up in numerous issues.

I wish to thank Prof. Arnaldo Spalvieri from Politecnico di Milano and Prof. Visa Koivunen from Helsinki University of Technology for their guidance and support.

I am very grateful to all my friends in Finland, with whom I shared two fantastic years of my life. My thought goes especially to my classmates Kaisa Korhonen, Olli Pekka Pyysalo, Juho Mooses Paaso and Florian Dupuy for their ever-lasting good mood and friendship, along with the unforgettable MF coffee breaks.

I would also like to thank my friends Roberto Mauri, Valentina Muraretto, Luca Zambonin, Stefano Arosio, Stefano Scuratti and Alex Giacomo Scilironi for their unique friendship, help, support and good humor throughout the long time we have known each other.

Lastly, but more importantly, I wish to thank my wonderful family: Mariarosa Parravicini, Pierangelo Pansana and Matteo Pansana for their constant understanding, love and advice.

Otaniemi, August 6, 2010

Lorenzo Carlo Pansana

Contents

List of Figures

List of Tables

Symbols and Abbreviations

Symbols

(ρ, θ, ϕ)	Spherical coordinates
$(\tau^{(i,k)}, \theta_{rx}^{(i,k)}, \phi_{rx}^{(i,k)}, \Theta_{tx}^{(i)}, \Phi_{tx}^{(i)})$	Time-angular coordinates of the k-th ray of the i-th cluster
(θ_{rx}, ϕ_{rx})	Direction of arrival (elevation and azimuth)
(θ_{tx}, ϕ_{tx})	Direction of departure (elevation and azimuth)
(i, k)	cluster index and ray index (within a given cluster)
(L, W, H)	Room length, width and height
$(T^{(i)}, \Theta_{rx}^{(i)}, \Phi_{rx}^{(i)}, \Theta_{tx}^{(i)}, \Phi_{tx}^{(i)})$	Time-angular coordinates of the i-th cluster
(u_x, u_y, u_z)	Direction cosines
(x, y, z)	Cartesian coordinates
$\alpha^{(i,k)}$	Complex-valued amplitude of the k-th ray of the i-th cluster
Γ, γ	Cluster and ray decay factors
$\hat{b}_k$	Estimated bit-sequence
λ_0	Operating wavelength
Λ, λ	Cluster and ray inter-arrival rates
$\mathbf{B}(f)$	Fading matrix
$\mathbf{c}$	Rx combiner weights column-vector
$\mathbf{C}(f)$	General Rx beamformer weights column-vector
$\mathbf{H}(\tau), \mathbf{H}(f)$	Frequency-selective MIMO Channel matrix
$\mathbf{k}_s$	Wave-vector corresponding to direction (θ_s, ϕ_s)
$\mathbf{n}(t), \mathbf{N}(f)$	Noise samples column-vector
$\mathbf{p}_n$	Position column-vector of the n-th array element
$\mathbf{V}_{rx}(\mathbf{k})$	Rx Steering matrix
$\mathbf{V}_{tx}(\mathbf{k})$	Tx Steering matrix
$\mathbf{v}(\mathbf{k}_s)$	Steering column-vector
$\mathbf{V}(\theta_{tx}, \phi_{tx}), \mathbf{V}(\theta_{rx}, \phi_{rx})$	Tx and RX steering matrix
$\mathbf{w}$	Tx beamformer weight column-vector
$\mathbf{x}(t), \mathbf{X}(f)$	Rx snapshot column-vector
$\mu_S^{(i)}, \sigma_S^{(i)}$	Reflection coefficient mean and RMS
$\overline{\beta^{(i,k)}}$	Average power of the k-th ray of the i-th cluster
$\overline{N_C}, \overline{N_R^{(i)}}$	Average number of clusters and rays
σ_{ang}	Ray angular RMS
σ_{look}	RMS of the TRx orientation deviation about the LOS
σ_s	Small-scale fading RMS
$\Upsilon(\theta, \phi)$	Frequency-wavenumber response
$a(t), A(f)$	Tx beamformer input signal (RF)
b_k	Tx bit-sequence
$B(\theta, \phi)$	Beam-pattern
c	Velocity of light $\approx 3 \cdot 10^8$ m/s
$d^{(i,k)}$	path length of the k-th ray of the i-th cluster

d_x, d_y	Inter-element spacings for URAs
f	Frequency
f_0	Design frequency: 60 GHz
$G_{refl}^{(i)}$	Reflection coefficient of the i-th cluster
$h(t, \theta_{rx}, \phi_{rx}, \theta_{tx}, \phi_{tx})$	Time-invariant Channel Impulse Response
K_{LOS}, K_C	Inter-cluster and intra-cluster Rician K-factors
M	Number of URA elements along y
N	Number of URA elements along x
$N_R^{(i)}$	Number of rays within the i-th cluster
N_C, N_R	Number of clusters and rays
$P(t)$	Power delay profile
R	Number of Rx antennas
r_k	Rx symbol-sequence
s_k	Tx symbol-sequence
$s(t)$	Tx base-band wave-form
T	Number of Tx antennas
t	Time
$y(t), Y(f)$	Rx beamformer output (RF)
$z(t)$	Rx base-band wave-form

Operators

$(\cdot)^T$	Transpose
$(\cdot)^H$	Conjugate transpose
$\mathbf{I}_N$	Identity matrix of dimension $N \times N$
$\mathbf{1}_N$	Column vector of N ones
$*$	Convolution
$\otimes$	Kronecker product
$\|\cdot\|$	Euclidean norm
$E[\cdot]$	Expectation
vec$(\cdot)$	Stack the columns of a matrix to form a column vector

Abbreviations

ABF	Analog BeamForming
ADC	Analog to Digital Converter
AWGN	Additive White Gaussian Noise
CDF	Cumulative Density Function
CIR	Channel Impulse Response
CMOS	Complementary Metal-Oxide Semiconductor
DAC	Digital to Analog Converter
DBF	Digital BeamForming
DoA	Direction of Arrival
DoD	Direction of Departure

ECMA	European Computer Manufacturers Association
FDE	Frequency-Domain Equalization
FFT	Fast Fourier Transform
FIR	Finite Impulse Response
GSCM	Geometry-based Stochastic Channel Model
HD	High-Definition
HDMI	High-Definition Multimedia Interface
HDTV	High-Definition TeleVision
HPBW	Half-Power Beam Width
IEEE	Institute of Electrical and Electronic Engineers
IFFT	Inverse Fast Fourier Transform
ISI	Inter-Symbol Interference
LNA	Low-Noise Amplifier
LO	Local Oscillator
LOS	Line-Of-Sight
MAC	Medium Access Control
MIMO	Multiple-Input Multiple-Output
MISO	Multiple-Input Single Output
mmWave	Millimeter-Wave
MRA	Main Response Axis
MRC	Maximum Ratio Combining
NICT	National Institute of information and Communications Technology
NLOS	Non Line-Of-Sight
NNBW	Null-to-Null Beam Width
OFDM	Orthogonal Frequency-Division Multiplexing
OLOS	Obstructed Line-of-Sight
PC	Personal Computer
PDA	Personal Digital Assistant
PDF	Probability Density Function
PDP	Power Delay Profile
PHY	Physical Layer
PSD	Power Spectral Density
RF	Radio Frequency
RMS	Root-Mean Square
RV	Random Variable
Rx	Receiver
SC	Single-Carrier
SDCM	Semi-Deterministic Channel Model
SIMO	Single-Input Multiple Output
SISO	Single-Input Single-Output
SINR	Signal-to-Interference and Noise Ratio
SNR	Signal-to-Noise Ratio
STB	Set-Top Box
SVM	Steering Vector Model
TDE	Time-Domain Equalization

TG3c	IEEE Task Group 802.15.3c
TGad	IEEE Task Group 802.11ad
TRx	Transceiver
Tx	Transmitter
ULA	Uniform Linear Array
URA	Uniform Rectangular Array
WiGig	Wireless Gigabit Alliance
WLAN	Wireless Local Area Network
WPAN	Wireless Personal Area Network
WSSUS	Wide-Sense Stationary - Uncorrelated Scattering

1 Introduction

Indoor wireless communications at 60 GHz have recently gained a lot of momentum from industry and academy because of their potential to deliver multi-gigabit rates over short distances. The main driver of this technology is the huge license-free bandwidth that has been allocated worldwide at these frequencies, reaching up to 7 GHz. Long-range communication systems are practically unfeasible in this band because of the presence of the oxygen absorption peak, thus leaving space for high data-rate indoor wireless systems (where the losses due to oxygen absorption are negligible).

The main difficulty that the 60 GHz technology must face is the poor link budget, which is a result of the increased path loss and the extended transmission bandwidth of 60 GHz systems (as large as 2 GHz). For a fixed Tx-Rx distance, these two aspects respectively translate into a more severe signal attenuation and a higher total noise power when compared to systems operating at lower frequencies.

In recent research papers on 60 GHz technology [1–5], antenna-array beamforming is indicated as the key-solution to mitigate the limited link budget problem. Adaptive antenna arrays supporting beamforming should be employed at least at one end of the transceiver system and should support reliable communication links in Line-of-Sight (LOS) and NLOS scenarios. Finally, in order to ensure the success of 60 GHz radios, beamforming techniques need to be inexpensive and readily amenable to mass production [3]. The evaluation of the performance of low-cost transmit-receive beamforming solutions over the 60 GHz indoor channel is therefore a fundamental step in the design of 60 GHz transceiver systems.

Many recent studies [6–12] focused on antenna solutions for 60 GHz radios. The research has focused on digital multi-antenna approaches, such as multiple-input multiple-output (MIMO) techniques [11] or Digital BeamForming (DBF) architectures [7, 10]. However, few investigations have concentrated on the topic of transmit-receive Analog BeamForming (ABF), which is the technique that best suits the low-cost and low-complexity requirements for 60 GHz radio transceivers. Furthermore, due to the lack of Direction of Departure (DoD) - Direction of Arrival (DoA) information in 60 GHz MIMO channel models, several studies had to assume omni-directional transmit antennas [8] or i.i.d flat-fading MIMO channels [7, 11, 12], or finally resort to ray-tracing simulations [9, 12].

The purpose of this thesis is to evaluate a joint analog transmit-receive beamforming solution applied to MIMO channel models specifically derived for the 60 GHz indoor propagation, in LOS and NLOS scenarios and for different array sizes. The scope of the evaluation is limited to analog beamforming architectures with one scalar weight per antenna, where the signal combining is performed at Radio Frequency (RF) level. As for the antenna arrays, Uniform Rectangular Arrays (URA) of various sizes are considered.

1.1 Original Contributions

The main contributions of this thesis may be stated as follows:

- Evaluate the performance of a joint analog Tx-Rx beamforming approach based on beam-switching applied to a 60 GHz MIMO channel in terms of beamforming gain, average spectral efficiency and coherence bandwidth of the beamformed channel. Investigate the impact of the URA size and of the channel nature (LOS/NLOS) on the system performance. Compare the performance results with the upper-bound given by an optimal beamforming scheme.

Instrumental to the aforementioned claim:

- Develop a semi-deterministic DoD-DoA MIMO channel model based on a combination of geometrical optics and the statistical characterization available in the literature.

1.2 Scope of the Thesis

The first step towards the Tx-Rx beamforming system design consists of the definition of the MIMO channel between two transceivers. The characteristics of indoor propagation at 60 GHz are investigated and a channel model that can be directly applied to the Tx-Rx system design is proposed. Based on the combination of geometrical-optics and the well-known Saleh-Valenzuela statistical model [13], this channel model features a DoD-DoA characterization (both elevation and azimuth angles are considered), which is essential in constructing the MIMO channel matrix. The accuracy of the proposed model is assessed through a comparison with the results of a channel measurements campaign performed by the IEEE 802.15 task-group 3c (TG3c).

Secondly, a joint analog Tx-Rx beamforming scheme is introduced. The technique is based on beam-switching, also known as "exhaustive search". With this method, the Tx-Rx beam-vector pair that maximizes the average output Signal-to-Noise Ratio (SNR) is selected using a codebook of orthogonal beam-vectors spanning the whole 3-D space. The performance of this scheme is evaluated in terms of beamforming gain, average spectral efficiency and coherence bandwidth of the end-to-end channel obtained after beamforming. The evaluation is applied to the 60 GHz MIMO channel previously introduced, in LOS and NLOS configurations and for different URA sizes. The spectral efficiency of the beam-switching technique is then compared to that of an optimal digital beamforming scheme. For the comparison, Dominant Eigenmode Transmission (DET) beamforming is considered.

Other analog beamforming solutions are investigated with the goal of overcoming the main drawbacks of beam-switching: the duration of the procedure (for large arrays) and the inflexible quantized spatial resolution. An alternative approach

that maximizes the average output SNR and calculates the optimal weights via eigendecomposition is introduced. The performance of this approach is compared to that of the beam-switching beamforming. The complexity and feasibility of these schemes are considered, too.

Finally, conclusions on the investigation are given and a few open research topics are outlined.

The aforementioned investigation mostly relies on Monte Carlo simulations performed using several Matlab tools with the following simulation procedure. Multiple channel realizations are obtained through the SDCM, initialized with the channel parameters and room size of the IEEE TG3c "residential room" [14]. NLOS scenarios are obtained simply by removing the LOS path. The position and orientation of the transceivers varies between different realizations. The convention is to assign power 1 and zero delay to the LOS path. For each realization, the MIMO channel matrix is evaluated on a bandwidth of 2 GHz. The beamforming arrays are applied to both ends of the MIMO matrix and the end-to-end beamformed channel is obtained. Using this quantity, the coherence bandwidth and the average (over the considered band) spectral efficiency and beamforming gain are extracted. The performance parameters are finally averaged over multiple channel realizations.

1.2.1 Assumptions

The following basic assumptions are considered valid throughout the entire dissertation:

- Wide-Sense Stationary symmetric channel with uncorrelated scattering (WSSUS);
- Negligible inter-room propagation;
- Narrow-band arrays;
- Omni-directional array elements with half-wavelength spacing;
- Perfect Channel State Information (CSI) available at Tx and Rx sides;
- Interference-free environment;
- Spatially-white Additive White Gaussian Noise (AWGN), uncorrelated noise and signal;

1.3 Organization of the Thesis

The rest of the thesis is organized as follows:

- **Chapter 2** contains a brief survey on 60 GHz indoor wireless communications. The technology enablers and drivers are first presented, followed by a description of some of the most impelling challenges that the 60 GHz technology must tackle. Finally, some insight on the present standardization work is provided.

- **Chapter 3** provides a characterization of the array structures considered in this report: standard uniform rectangular arrays (URA) with one scalar weight per antenna. The topic of beamforming is introduced in terms of steering vectors and frequency-wavenumber response, and the beam-pattern characteristics are presented for the considered array geometry. The technique of array steering is then illustrated. Afterwards, the choice of analog beamforming over digital beamforming is discussed. Finally, a mathematical description of the analog Tx-Rx system is provided.

- **Chapter 4** is dedicated to channel modeling. First, the spatial and temporal characteristics of indoor propagation at 60 GHz are described and the available channel models are briefly introduced. A semi-deterministic channel model that can be readily applied to the Tx-Rx system design is then presented. The validity of the proposed model is then assessed through a comparison with the measurements available in the literature. Finally, the MIMO channel matrix is shown to be straightforwardly constructed starting from the proposed channel model.

- **Chapter 5** presents the evaluation framework of joint analog Tx-Rx beamforming for 60 GHz indoor radio systems. First, a technique based on beam-switching is presented for the considered array configurations and the beam-vector codebook is described. Secondly, the performance parameters employed are briefly introduced. The simulation procedure is then outlined, followed by a presentation of the results. The observed performance is compared against the upper-bound given by DET beamforming. A beamforming solution alternative to the beam-switching technique is subsequently presented along with its performance results. Finally, the performance of the considered schemes are compared and discussed in terms of cost-performance trade-off.

- **Chapter 6** concludes the thesis and outlines future research topics.

- **Appendix A** contains a detailed description of the MIMO channel simulator.

- **Appendix B** presents a mathematical description of the beam-vector codebook used in Chapter 5.

2 Overview on 60 GHz Wireless Communications

Over the past decades we have witnessed an unprecedented growth of wireless communication services driven by the development of advanced and "bandwidth-hungry" technologies. The industry has evolved from pagers and cell-phones to cutting-edge personal digital assistants (PDAs), set-top-boxes (STB), personal computers (PCs) and other devices capable of delivering high-speed multimedia content while connected to fast and reliable broadband wireless local area networks (WLAN) and wireless personal area networks (WPAN) [2–4]. In the attempt of keeping up with the huge amount of data traffic required by the most recent and high-bit-rate multimedia services, wireless networks have increased their capacity at the pace of ten times every five years and are expected to break the 1 Gbit/s limit in the near future [4] (see Figure 2.1).

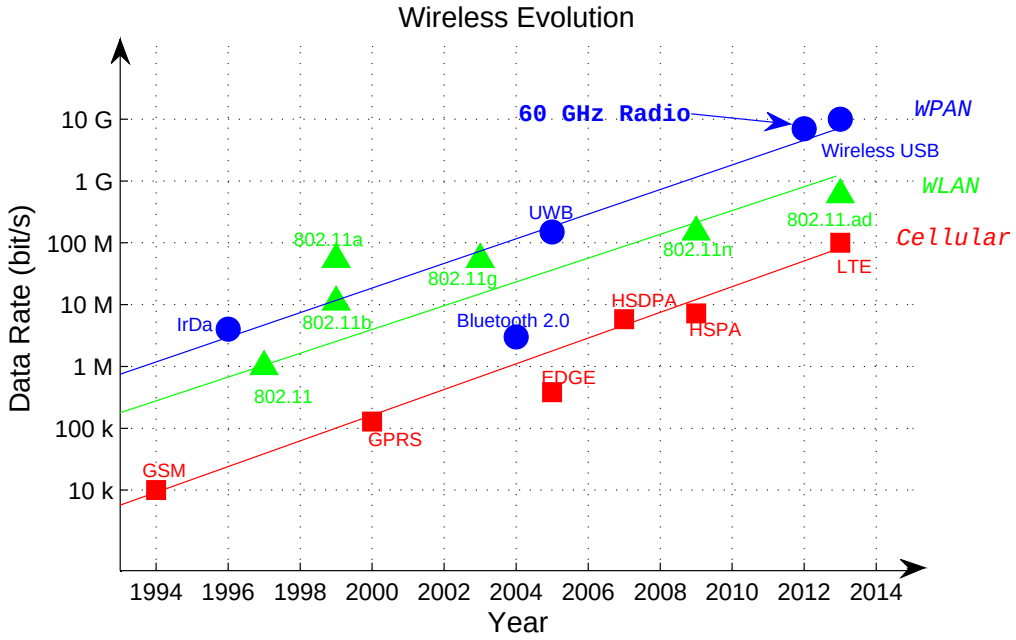

Figure 2.1: Evolution of wireless communication systems in the last decade.

There is a large number of services and applications that require very high bit rates (from hundreds of megabits to tens of gigabit), and this number will most likely increase in the future. Such applications include high definition television (HDTV) uncompressed streaming, real-time HD audio/video delivery, gaming and fast file transfers. Currently, these applications rely on wired technologies such as USB 2.0, High Definition Multimedia Interface (HDMI) and FireWire[1] cables. On the other hand, contemporary wireless standards support only moderate levels of data traffic, as seen in Bluetooth and WLANs, and are clearly unable to support such high data-rate services [3]. In this context, the millimeter-wave band[2] is believed to be the

[1]FireWire technology is often referred to as IEEE 1394.
[2]Frequency range: 30 - 300 GHz [2]

most promising candidate for next-generation wireless communications capable of delivering multi-gigabit rates through an air interface (see Figure 2.2).

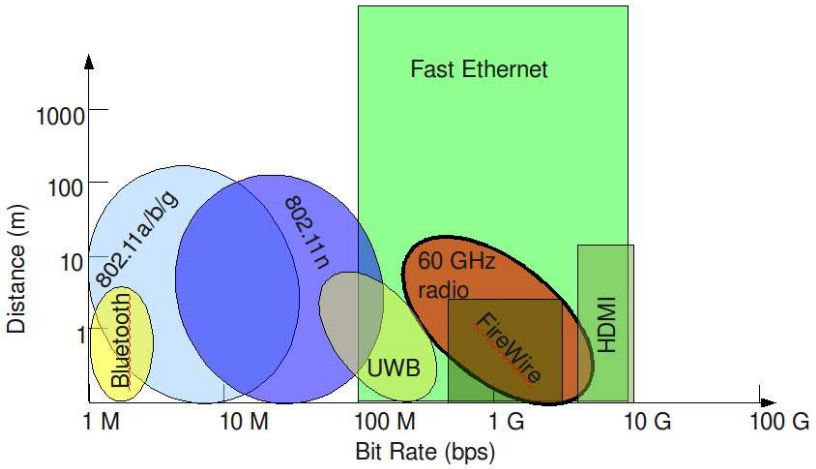

Figure 2.2: Data rates and coverage ranges for the most common wired (rectangles) and wireless (ellipses) standards. Source: [2].

2.1 Technology Enablers and Drivers

Within the mmWave landscape, the 60 GHz band in particular is considered as the most promising candidate to support multi-gigabit data rates [2]. This is motivated mainly by the following technology-enablers and drivers:

- **Availability of 7 GHz unlicensed spectrum**. The most attractive aspect of this technology lays in the fact that there is a very broad portion of the electromagnetic spectrum (up to 7 GHz) about 60 GHz which is totally license-free worldwide. Reportedly one of the largest unlicensed bandwidth being allocated in history [2], it is by far broader than the available unlicensed spectrum around 2.5 GHz and 5 GHz [11]. The exact spectral extension varies depending on location-specific regulations which may be found in details in [15], and are illustrated in Figure 2.3. In [16] it is reported that the maximum allowed transmission bandwidth equals 2.16 GHz. The reason why such a broad portion of the electromagnetic spectrum is license-free resides

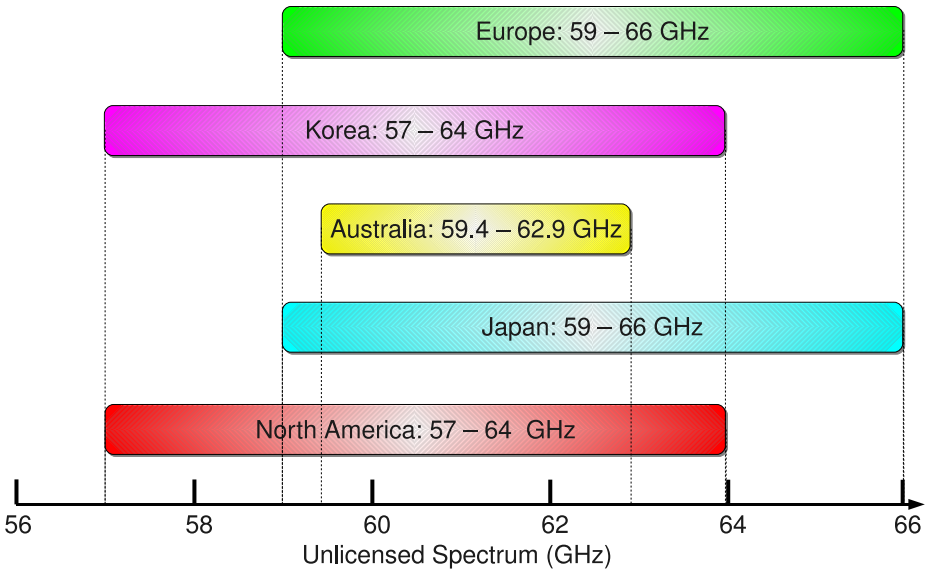

Figure 2.3: License-free spectra allocated for 60 GHz systems.

in the presence of the oxygen absorption peak occurring at 63 GHz [17], as depicted in Figure 2.4. This phenomenon causes additional signal attenuation up to 15 - 30 dB/km, making outdoor long-range communications (> 1-2 km) in the 60 GHz band practically unfeasible [18]. This feature enables higher frequency reuse and therefore allows the coexistence of closely-spaced 60 GHz radios and other systems operating at different frequencies [2].

- **Low interference levels**. At mmWave frequencies, signal deterioration due to attenuation is very severe. In order to counter the effects of attenuation, high-gain directional antennas are required in any practical system. As a result, not only the received signal power rapidly fades as the distance from the transmitter increases, but the signal is also confined to a narrow solid angle, thus reducing the amount of interference to/from another communication system operating on the same band. Furthermore, in addition to the increased attenuation due to propagation (oxygen absorption and higher path loss), the loss due to wall penetration is greater than that occurring at lower frequencies. Measurements carried out in recent years [20–22] came to the conclusion that 60 GHz signals can be practically considered as confined within a single room [2, 22]. Therefore, due to the severe propagation and penetration losses in addition to the high directionality of links operating at these frequencies, 60 GHz communications are expected to experience low levels of interference.

- **Relaxed power constraints**. Because of the intrinsic spatial confinement

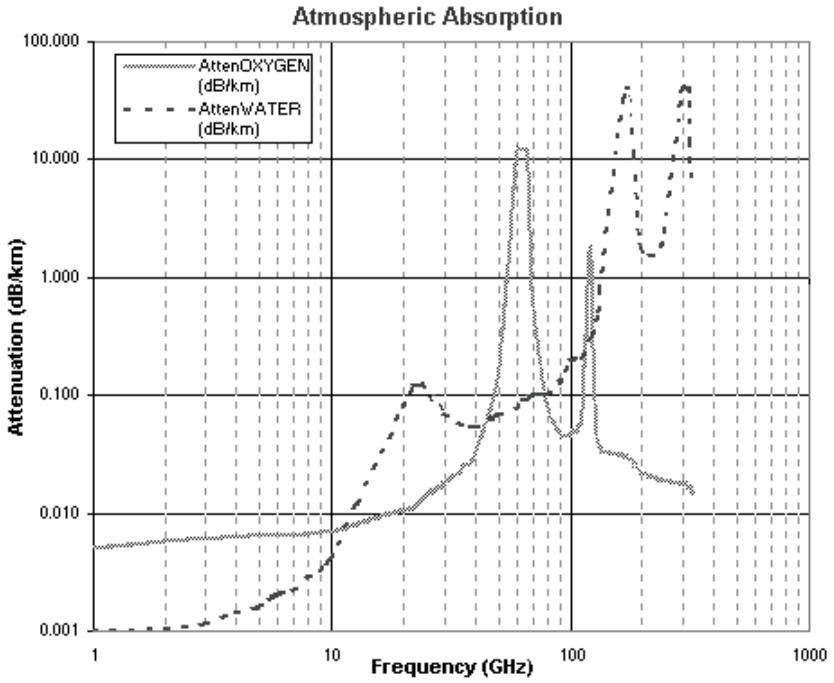

Figure 2.4: Oxygen and water absorption at sea-level as a function of frequency. (Source: [19])

that characterizes the 60 GHz band and the consequent low-interference levels, the power constraints that regulate the usage of this band are relaxed when compared to other technologies [2]. The allowed power emissions are listed in Table 2.1.

Table 2.1: Frequency band regulations for 60 GHz communications. Source: [2]

Region	Unlicensed bandwidth (GHz)	Tx Power	EIRP	Max Antenna gain
USA & Canada	7 GHz (57 - 64)	500 mW	43 dBm	NS
Japan	7 GHz (59 - 66), max 2.5 GHz	10 mW	NS	47 dBi
Australia	3.5 GHz (59.4 - 62.9)	10 mW	150 W	NS
Korea	7 GHz (57 - 64)	10 mW	TBD	TBD
Europe	7 GHz (59 - 66)	20 mW	57 dBm	37 dBi

- **Small form factor of the antenna subsystem**. Because of the reduced design wavelength (5 mm at 60 GHz), the form factor of transceiver (TRx) antennas is significantly smaller for a 60 GHz system than a lower-frequency system. Therefore, electrically large antennas may be designed in a small area. This feature enables a broad variety of antenna solutions for 60 GHz radios that would be very difficult, if not impossible, at smaller frequencies.

Furthermore, this aspect results in a higher level of integration which in turns translates into a lower device cost.

- **Low-cost front end technology**. In several surveys on 60 GHz technology [2, 3, 18, 23–25] it was reported that low-cost, highly integrated and low volume front-end technology for 60 GHz radios is now available, thanks to the constant efforts by industry and academia. In particular, RF technology based on complementary metal-oxide semiconductors (CMOS) is indicated as the leading solution, enabling the development of 60 GHz radios at the same cost structure of radios operating in the gigahertz range or less [23].

2.2 Challenges for 60 GHz

Along with the significant benefits, the 60 GHz band has several challenges to tackle in order to unleash is full potential. Some of them are discussed below:

- **Poor link budget**. The 60 GHz band suffers from severe attenuation due to propagation. Let alone the oxygen absorption, which may be neglected for short radio links [1], the free-space path loss occurring at 60 GHz is in the order of 20-30 dB higher than that of a WLAN operating at 2.5 GHz, as it can be readily determined by using the Friis equation [26] for free-space attenuation. Furthermore, due to the very large transmission bandwidth (up to 2.16 GHz), the total noise power is by far greater than that of systems operating at lower frequencies. These combined factors result in a poor link budget[3].

- **LOS signal blockage**. Another crucial problem of 60 GHz radios is the blockage of the line-of-sight (LOS) signal, which may occur due to the presence of furniture, objects or humans within the propagation environment. In [27], it was reported that the presence of a human on the trajectory of the LOS path typically causes a shadowing loss greater than 20 dB[4]. Nonetheless, 60 GHz radios must include a strategy to establish reliable communication links in NLOS scenarios.

- **Multipath propagation**. Indoor radio propagation at 60 GHz is characterized by rich scattering and reflections, which results in multipath frequency-selective radio channels [28]. This feature means that 60 GHz communications are likely to suffer from the inter-symbol interference (ISI) problem, which may severely degrade the system performance if the proper countermeasures are not taken.

The above problems must be solved in order for 60 GHz technology to unleash its full potential and deliver multi-gigabit data rates. In the literature, adaptive

[3] See the case study reported in Section 5.3.2.

[4] This scenario is often referred to as obstructed line-of-sight (OLOS). Throughout the remainder of the report, OLOS and NLOS configurations are assumed identical.

antenna array beamforming is addressed as the key-solution to overcome the poor link budget and the LOS-blockage problems [1–5]. This solution would provide the necessary array gain to counter the effect of the increased attenuation at 60 GHz, achieved through the employment of multiple antenna elements. Furthermore, with adaptive antenna array beamforming, the radiation pattern of both transceivers can be adaptively varied depending on the propagation conditions. In NLOS scenarios, beamforming can be exploited to electronically steer the Tx-Rx beam-patterns towards the strongest reflection available. Antenna array solutions for 60 GHz systems should feature the following properties [18]:

- Low fabrication cost, readily amenable to mass production
- Light weight and low volume
- Easy to integrate with RF front-end circuitry
- High performance (gain, efficiency, broad bandwidth, sufficient spatial resolution)

The ISI mitigation problem may be tackled in many ways such as equalization, orthogonal-frequency-division-multiplexing (OFDM) and FFT processing [29]. In [2] and [16], it was reported that both equalized single-carrier (SC-TDE/FDE) and OFDM techniques are suitable for 60 GHz radios, and their usage depends on application-specific or hardware-specific requirements. Some of the key aspects of these two modulation schemes are summarized in Table 2.2.

Table 2.2: Modulation scheme summary: OFDM vs. SC-TDE/FDE ([2])

Modulation scheme	**Advantages**	**Disadvantages**
OFDM	Less complex ISI mitigation for severely frequency-selective channels;	Poor power efficiency;
	High spectral efficiency	Sensitive to phase noise
	Flexible frequency allocation, allowing high levels of adaptations	Sensitive to spectrum broadening
SC-TDE/FDE	Maximum power efficiency;	Increased equalizer complexity for severely frequency-selective channels;
	More robust to phase noise;	Poor spectral efficiency;
	More robust to spectrum broadening	Lower capability of adaptation

2.3 Standardization Work

Standardization in the 60 GHz wireless networks is currently being carried out by several industrial consortia and international standard organizations. Within the

IEEE (Institute of Electrical and Electronic Engineers) two task groups are presently leading the way: 802.15.3c (TG3c) on WPAN and 802.11ad (TGad) on WLAN. The first group published the first version of their standard [16], providing medium access control (MAC) and physical layer (PHY) specifications and requirements. The latter is currently working on a very-high-throughput version of the 802.11 WLAN standard based on 60 GHz radios, ensuring backward compatibility with the 802.11a/b/g/n family [30].

Among the industry-led organizations that are currently investing on 60 GHz technology, the most significant efforts have been taken by WirelessHD [31], the European Computer Manufacturers Associations (ECMA International) [32] and the Wireless Gigabit Alliance (WiGig) [33]. These associations are respectively focused on uncompressed HDTV streaming, wireless HDMI and 60 GHz WLAN.

3 Array Signal Processing Basic Concepts

This chapter provides an introduction to the main concepts of array signal processing that lay the groundwork for the remainder of this report. The purpose, along with the presentation of the notation employed in this manuscript, is to describe antenna arrays as filters that operate in the frequency-wavenumber domain and to provide a mathematical expression for the Tx-Rx beamforming system model. The discussion is limited to uniform rectangular arrays (URA) with scalar weights and omni-directional elements. A broader and more detailed presentation on array signal processing, including optimum beamforming schemes and their adaptive implementations, may be found in textbooks such as [34], [35] and [36].

3.1 Problem Geometry

The coordinate system adopted in this manuscript is the spherical coordinate system, where a given point in the 3-D space is identified by its radius, azimuth and elevation, denoted by the symbols ρ, θ and ϕ, respectively. The definition of these angles can be inferred from Figure 3.1, and the relationships between the cartesian and the spherical coordinate systems is expressed as follows:

$$\begin{cases} x = \rho \sin\theta \cos\phi = \rho u_x \\ y = \rho \sin\theta \sin\phi = \rho u_y \\ z = \rho \cos\theta = \rho u_z \end{cases} \longleftrightarrow \begin{cases} \rho &= \sqrt{x^2+y^2+z^2} \\ \theta &= \cos^{-1}\left(\frac{z}{\sqrt{x^2+y^2+z^2}}\right) \\ \phi &= \tan^{-1}\left(\frac{y}{x}\right) \end{cases} \tag{3.1}$$

where (u_x, u_y, u_z) are the direction cosines.

3.2 Antenna Arrays

An antenna array may be defined as a collection of antenna elements arranged in a specific geometry and positioned at a specific distance. Depending on the arrangement of its elements, one could distinguish between linear, planar and three-dimensional arrays. In this thesis, only **Standard Uniform Rectangular Array (URA)** are considered: the elements lay on the xy-plane, and the inter-element spacing along both abscissae (d_x and d_y) is constant and equal to $\lambda_0/2$, where λ_0 is 5 mm at 60 GHz. Like all two-dimensional array structures, URAs are capable of resolving both azimuthal and elevation coordinates. A $N \times M$ URA is represented in Figure 3.1.

Furthermore, the dissertation is restricted to *omni-directional array elements*, which means that the sensors of the arrays are assumed to radiate (and receive) power isotropically in the space and with unitary gain. Hence, only the *array factor* is considered in this work; incorporating the *element factor* is straightforward [34], but it is not considered here.

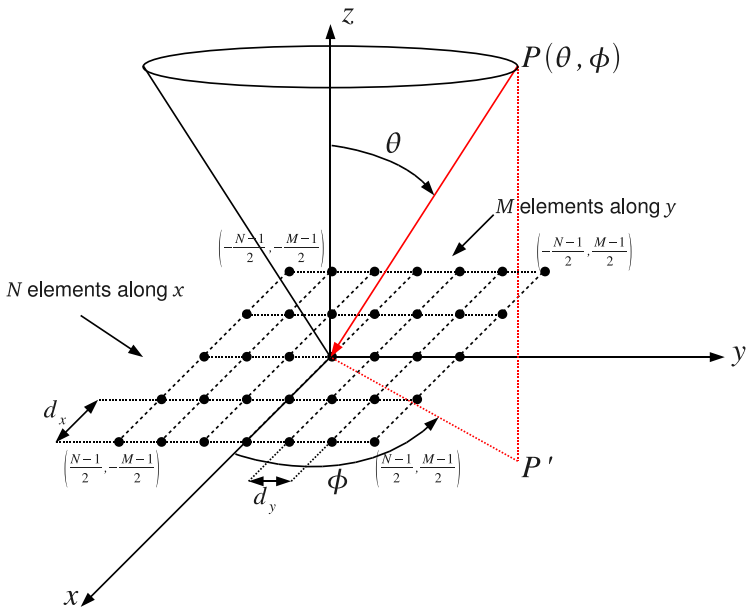

Figure 3.1: $N \times M$ planar array.

From a geometrical point of view, an array is described by the cartesian coordinates of its N elements, here denoted with the vector $\mathbf{p}_n$, $n = 0, \ldots, N-1$:

$$\mathbf{p}_n = \begin{bmatrix} p_{n,x} \\ p_{n,y} \\ p_{n,z} \end{bmatrix} \tag{3.2}$$

Naturally, the location of the origin of the coordinate system is arbitrary and does not affect the final results. The choice made here, in accordance with [34], is to adopt a centro-symmetric positioning of the array elements, that is the origin is always located at the center of mass of the array. Consequently, the position of the (n, m)-th element for an URA aligned laying on the xy plane is expressed in the following manner (see Figure 3.1):

$$\mathbf{p}_{n,m} = \begin{bmatrix} \left(n - \frac{N-1}{2}\right) d_x \\ \left(m - \frac{M-1}{2}\right) d_y \\ 0 \end{bmatrix} \qquad n = 0, 1, \ldots, N-1; \quad m = 0, 1, \ldots, M-1 \tag{3.3}$$

3.2.1 Steering Vector Model

Let us consider a single plane-wave signal of spectrum $A(f)$ impinging on an arbitrary array of N elements from direction (θ_a, ϕ_a). Assuming far-field propagation[1]

[1] As a consequence of this assumption, the iso-phase surfaces of the impinging wave-field may be considered linear and parallel (plane-wave model). Far-field propagation is assumed throughout the remainder of this report. For more insights on far-field propagation, the reader is referred to [37].

and isotropic transmission medium, the observation vector is given by delayed copies of the received signal:

$$\mathbf{X}(f) = \begin{bmatrix} X_0(f) \\ X_1(f) \\ \vdots \\ X_{N-1}(f) \end{bmatrix} = \begin{bmatrix} A(f)e^{-j2\pi f\tau_0} \\ A(f)e^{-j2\pi f\tau_1} \\ \vdots \\ A(f)e^{-j2\pi f\tau_{N-1}} \end{bmatrix} \tag{3.4}$$

where the delay at the delay at the n-th element is given by [34]:

$$\tau_n = -\frac{1}{c}[\sin\theta_a \cos\phi_a p_{n,x} + \sin\theta_a \sin\phi_a p_{n,y} + \cos\theta_a p_{n,z}] \tag{3.5}$$

The exponential terms in (3.4) can be therefore expressed as follows:

$$2\pi f\tau_n = -\frac{2\pi}{\lambda}[\sin\theta_a \cos\phi_a p_{n,x} + \sin\theta_a \sin\phi_a p_{n,y} + \cos\theta_a p_{n,z}] = -\mathbf{k}_a^T \mathbf{p}_n \tag{3.6}$$

where $\mathbf{k}_a$ is the wave-number corresponding to direction (θ_a, ϕ_a). Recalling (3.4), the observation vector is now given by

$$\mathbf{X}(f) = A(f)\mathbf{v}(\theta_a, \phi_a) \tag{3.7}$$

where $\mathbf{v}(\theta_a, \phi_a)$ is termed *steering vector*. For an arbitrary N-element array, the steering vector can be therefore expressed as follows:

$$\mathbf{v}(\theta_a, \phi_a) = \begin{bmatrix} e^{j\mathbf{k}_a^T \mathbf{p_0}} \\ e^{j\mathbf{k}_a^T \mathbf{p_1}} \\ \vdots \\ e^{j\mathbf{k}_a^T \mathbf{p_{N-1}}} \end{bmatrix} = \begin{bmatrix} e^{-j\frac{2\pi}{\lambda}(\sin\theta_a \cos\phi_a p_{0,x} + \sin\theta_a \sin\phi_a p_{0,y} + \cos\theta_a p_{0,z})} \\ e^{-j\frac{2\pi}{\lambda}(\sin\theta_a \cos\phi_a p_{1,x} + \sin\theta_a \sin\phi_a p_{1,y} + \cos\theta_a p_{1,z})} \\ \vdots \\ e^{-j\frac{2\pi}{\lambda}(\sin\theta_a \cos\phi_a p_{N-1,x} + \sin\theta_a \sin\phi_a p_{N-1,y} + \cos\theta_a p_{N-1,z})} \end{bmatrix} \tag{3.8}$$

The steering vector model can be extended to the case of an $N \times M$ URA laying on the xy-plane in the following manner. First, it is convenient to define the steering vectors corresponding to the first lines of sensors along the x and y directions:

$$\mathbf{v}_x(\theta_a, \phi_a) = [e^{-j\frac{2\pi}{\lambda}\sin\theta_a \cos\phi_a p_{0,x}}, \ldots, e^{-j\frac{2\pi}{\lambda}\sin\theta_a \cos\phi_a p_{N-1,x}}]^T \tag{3.9}$$

$$\mathbf{v}_y(\theta_a, \phi_a) = [e^{-j\frac{2\pi}{\lambda}\sin\theta_a \sin\phi_a p_{0,y}}, \ldots, e^{-j\frac{2\pi}{\lambda}\sin\theta_a \sin\phi_a p_{M-1,y}}]^T \tag{3.10}$$

where $p_{n,x} = (n - \frac{N-1}{2})d_x$, $n = 0, \ldots, N-1$ and $p_{m,y} = (m - \frac{M-1}{2})d_y$, $m = 0, \ldots, M-1$ (recall (3.3)). At this point, the steering vector corresponding to

direction (θ_a, ϕ_a) for the URA is given by [34]:

$$\begin{aligned}\mathbf{v}(\theta_a,\phi_a) &= \mathbf{v}_x(\theta_a,\phi_a)\otimes\mathbf{v}_y(\theta_a,\phi_a)\\ &= \begin{bmatrix} e^{-j\frac{2\pi}{\lambda}(\sin\theta_a\cos\phi_a p_{0,x}+\sin\theta_a\sin\phi_a p_{0,y})}\\ \vdots\\ e^{-j\frac{2\pi}{\lambda}(\sin\theta_a\cos\phi_a p_{0,x}+\sin\theta_a\sin\phi_a p_{M-1,y})}\\ \vdots\\ e^{-j\frac{2\pi}{\lambda}(\sin\theta_a\cos\phi_a p_{N-1,x}+\sin\theta_a\sin\phi_a p_{0,y})}\\ \vdots\\ e^{-j\frac{2\pi}{\lambda}(\sin\theta_a\cos\phi_a p_{N-1,x}+\sin\theta_a\sin\phi_a p_{M-1,y})}\end{bmatrix}\\ &= \mathrm{vec}(\mathbf{v}_y(\theta_a,\phi_a)\mathbf{v}_x^T(\theta_a,\phi_a))\end{aligned} \tag{3.11}$$

where $\otimes$ denotes the Kronecker product and the vec operator creates a column vector from a matrix by stacking its column vectors below one another.

The steering vector model presented in the previous section is referred to as the *broadband model*. In this case, different frequencies experience different delays and the steering vector is a frequency-dependent term[2]. Although this is the most general case, in this thesis the *narrowband model* is adopted for the steering vectors. In [34] it is reported that the narrowband model can be assumed if the following condition holds:

$$B\cdot\Delta T_{max} \ll 1 \tag{3.12}$$

where B is the bandwidth of the transmitted signal and ΔT_{max} is the maximum travel time across the array. For the narrowband model, the delay experienced by the received signal when propagating across the array is approximated by a phase shift and the steering vector corresponding to a given direction is simply a set of complex-valued coefficients with unitary magnitude [34].

Let us verify that the narrowband assumption holds for realistic 60 GHz parameters. According the IEEE 802.15.3c standard [16], the maximum allowed transmission bandwidth is about $B = 2$ GHz. For a standard squared URA of N elements, the maximum travel time across the array is given by

$$\Delta T_{max} = \frac{\lambda_0}{2}\frac{\sqrt{2}N}{c} = \frac{N}{\sqrt{2}f_0} \tag{3.13}$$

Assuming a 36-element squared URA, it can be readily verified that (3.12) would still hold. Henceforth, for practical 60 GHz systems with $B \approx 2$ GHz, the narrowband assumption for the steering vector model is reasonably legitimate. Further proof of the validity of this assumption will be given later in this chapter, where it is seen that the beam-pattern can be practically considered constant across B (see Figure 3.5). Furthermore, in Chapter 5 it is shown that the simulation results obtained with the

[2]See the λ-dependency in (3.11)

narrowband model for the steering vectors are almost identical to those obtained with the broadband model (see Figure 5.9).

As a consequence of the narrowband assumption, the steering vector model can be considered frequency-independent. For the remainder of the dissertation the steering vectors will be calculated for $f = f_0$ and assumed constant across the entire spectrum:

$$\mathbf{v}(\theta_a, \phi_a) = \begin{bmatrix} e^{-j\frac{2\pi}{\lambda_0}(\sin\theta_a \cos\phi_a p_{0,x} + \sin\theta_a \sin\phi_a p_{0,y})} \\ \vdots \\ e^{-j\frac{2\pi}{\lambda_0}(\sin\theta_a \cos\phi_a p_{0,x} + \sin\theta_a \sin\phi_a p_{M-1,y})} \\ \vdots \\ e^{-j\frac{2\pi}{\lambda_0}(\sin\theta_a \cos\phi_a p_{N-1,x} + \sin\theta_a \sin\phi_a p_{0,y})} \\ \vdots \\ e^{-j\frac{2\pi}{\lambda_0}(\sin\theta_a \cos\phi_a p_{N-1,x} + \sin\theta_a \sin\phi_a p_{M-1,y})} \end{bmatrix} \tag{3.14}$$

3.3 Beamforming as Spatial Filtering

A beamformer is an array processor that operates a filtering operation in the frequency-wavenumber domain [34]. A block-scheme representation of a general receive beamformer with N antennas is illustrated in Figure 3.2: The filtering operation is per-

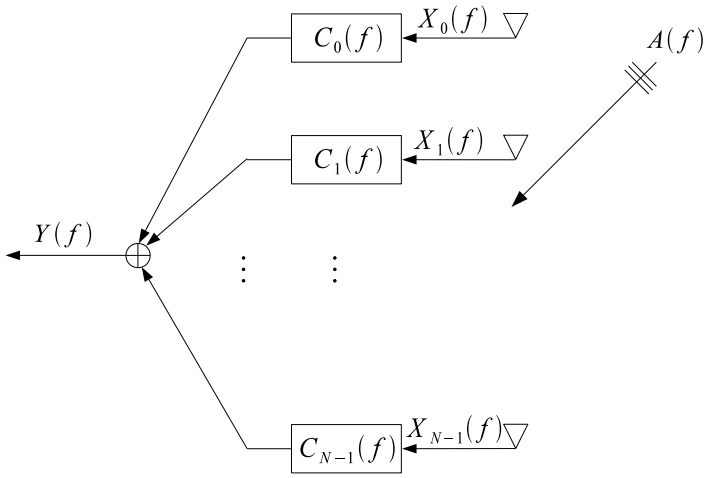

Figure 3.2: Block scheme representation of a general receive beamformer with N antennas.

formed by properly weighting the signal received by each element, and then adding up the partial contributions to form the beamformer output. The frequency-domain input-output relationship is expressed by:

$$Y(f) = \mathbf{C}^H(f)\mathbf{X}(f) = \mathbf{C}^H(f)\mathbf{v}(\theta_a, \phi_a)A(f) + \mathbf{C}^H(f)\mathbf{N}(f) \tag{3.15}$$

where $\mathbf{X}(f)$ is the observation vector, $\mathbf{C}(f)$ the processor frequency-domain weight-vector, $A(f)$ the impinging single-plane wave-form, $Y(f)$ the beamformer output and $\mathbf{N}(f)$ is a noise vector.

In this thesis, the discussion is limited to the case of beamforming with one scalar weight per antenna. Therefore, the weight-vector reduces to a set of complex-valued coefficients (constant across the entire transmission bandwidth), denoted with $\mathbf{c}$. Henceforth, the input-output relationship of the beamformer is given by

$$Y(f) = \mathbf{c}^H \mathbf{X}(f) = \mathbf{c}^H \mathbf{v}(\theta_a, \phi_a) A(f) + \mathbf{c}^H \mathbf{N}(f) \tag{3.16}$$

and the frequency-wavenumber response of the array to a single plane-wave signal impinging from a generic direction (θ, ϕ) has the following expression:

$$\Upsilon(\theta, \phi) = \mathbf{c}^H \mathbf{v}(\theta, \phi) \tag{3.17}$$

It should be noticed that each signal impinging on the array results into a steering vector. Furthermore, for the considered case of one scalar weight per antenna and the narrowband steering vector model, the frequency-wavenumber response is actually constant in the transmission bandwidth.

The weight-vector $\mathbf{c}$ can be designed to obtain a specific array response. In many cases the weights are pure-phase terms, and the beamformer re-phases any signal coming from a specific direction (see Section 3.3.2). This type of beamformer is known as a *phased-array beamformer*, and will be used extensively throughout the thesis work. In other applications it may be desirable to adjust both the gain and the phase at the output of each sensor in order to obtain a specific response. In this case, the weights are implemented as a cascade of a gain and a phase shifter.

3.3.1 Beam-Patterns

One of the most important features of a beamformer is its beam-pattern, often referred to as radiation pattern, which is a representation of the its spatial response. In [34], the mathematical expression of the beam-pattern for a given weight-vector $\mathbf{c}$ is given by:

$$B(\theta, \phi) = \mathbf{c}^H \mathbf{V}(\theta, \phi) \tag{3.18}$$

where $\mathbf{V}(\theta, \phi)$ is termed *array manifold matrix*, a collection of the steering vectors spanning the whole (θ, ϕ) space.

In [34] it is shown that the beam-pattern of a phased-array URA with uniform power-normalized weights, i.e. $\mathbf{c} = \frac{1}{\sqrt{R}} \mathbf{1}_R$ where $R = NM$, is expressed by:

$$B(\theta, \phi) = \left[\frac{1}{\sqrt{N}} \frac{\sin\left(N \frac{\pi}{2} \sin\theta \cos\phi\right)}{\sin\left(\frac{\pi}{2} \sin\theta \cos\phi\right)} \right] \left[\frac{1}{\sqrt{M}} \frac{\sin\left(M \frac{\pi}{2} \sin\theta \sin\phi\right)}{\sin\left(\frac{\pi}{2} \sin\theta \sin\phi\right)} \right] \tag{3.19}$$

Figures 3.3 and 3.4 illustrate the standard beam-pattern of an ideal 10×6 URA laying on the xy plane through 3-D polar and pattern-cut representations.

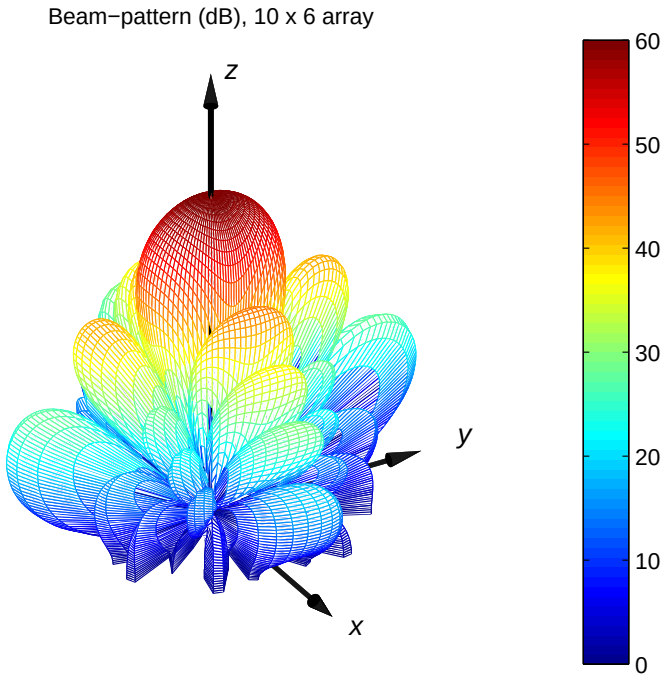

Figure 3.3: An ideal 10×6 URA standard beam-pattern.

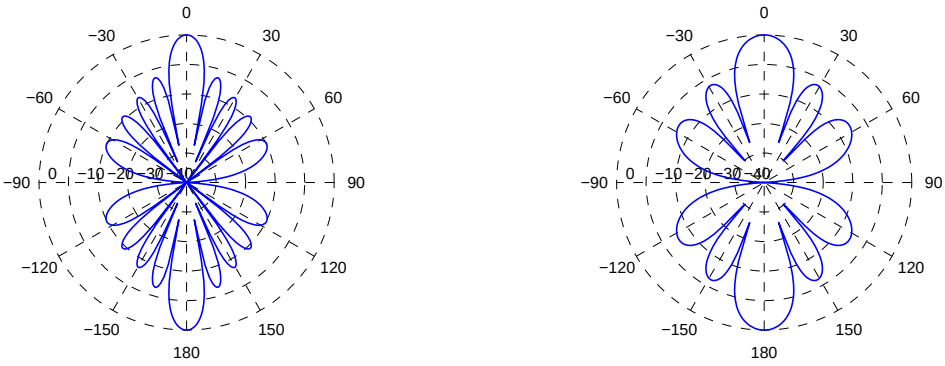

(a) Pattern-cut at $\phi = 0$.

(b) Pattern-cut at $\phi = \pi/2$

Figure 3.4: An ideal 10×6 URA standard beam-pattern (pattern cuts).

It should be noticed that the frequency-dependance does not appear in (3.19) since $d = \lambda_0/2$ was assumed and the model for the steering vectors (and thus the manifold matrix) is narrowband. However, if the broadband model is adopted, the array manifold matrix will contain frequency-dependent steering vectors. In turns, the beam-pattern will also exhibit frequency dependency[3]. Figure 3.5 illustrates the beam-pattern cut of a 6×6 -element phased array with uniform weighting, evaluated at different frequencies within a bandwitdth of 2 GHz centered about $f_0 = 60$ GHz. The inter-element spacing is $\lambda_0/2$, with $\lambda_0 = c/f_0 = 5$ mm. The manifold matrix is calculated using (3.11) with different values of λ.

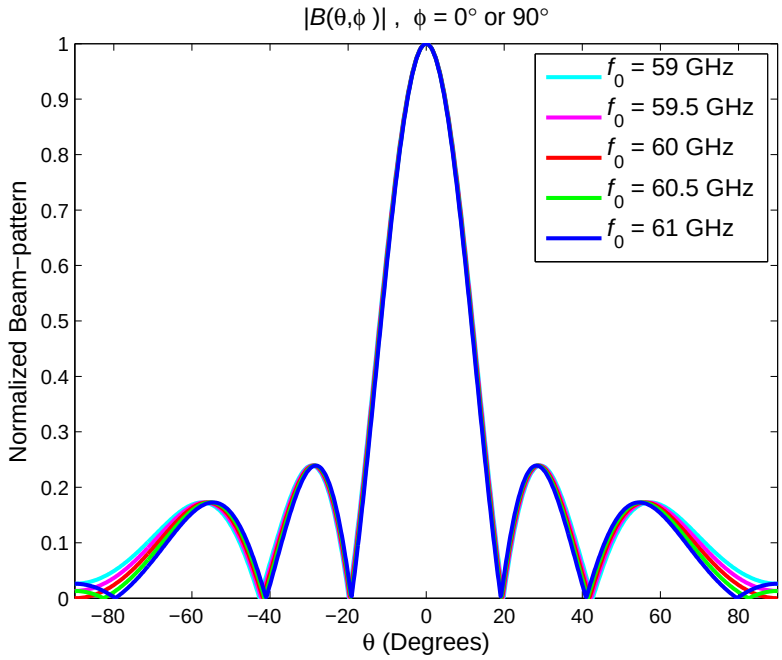

Figure 3.5: Pattern cut (horizontal/vertical plane) of a 6×6 -element URA evaluated at different frequencies within $B = 2$ GHz.

From Figure 3.5 it is seen that the beam-patterns are slightly different. This is due to the fact that the inter-element spacing equals half-wavelength only for the operating frequency $f_0 = 60$ GHz. As a consequence, the array is electrically over-dimensioned for greater operating frequencies and electrically under-dimensioned for smaller operating frequencies. However, since the ratio between the considered transmission bandwidth and the central frequency is about 3.3%, the observed variation of the beam-pattern is very small. In particular, the main lobe is seen to be practically identical at all frequencies. The beam-patterns slightly differ in the sidelobe region, but the variation can be considered negligible for practical purposes. As a result, the narrowband model for steering vectors can be regarded as valid for the considered scenario.

[3]The frequency-selectivity of the beamformer response may be given by the adoption of broadband steering vectors and/or broadband weight vectors. In this thesis, both terms are regarded as narrowband.

3.3.2 Array Steering

By properly defining the weight-vector $\mathbf{c}$, the array beam-pattern can be electronically *steered*, i.e. the Main Response Axis (MRA) changes direction. Array steering is achieved by applying a progressive phase-shift to the weights while maintaining the weight-vector Euclidean norm equal to unity, i.e. $||\mathbf{c}|| = \mathbf{c}^H\mathbf{c} = 1$. In [34], it is shown that in order to steer the array towards a given direction (θ_a, ϕ_a), the weight-vector should be a normalized version of the steering vector corresponding to (θ_a, ϕ_a). Therefore, to steer an N-element URA towards (θ_0, ϕ_0), the combiner weight-vector must be the following (recall (3.11)):

$$\begin{aligned}\mathbf{c} &= \frac{1}{\sqrt{N}}\mathbf{v}(\theta_0, \phi_0) \\ &= \begin{bmatrix} e^{-j\frac{2\pi}{\lambda_0}(\sin\theta_0\cos\phi_0 p_{0,x}+\sin\theta_0\sin\phi_0 p_{0,y})} \\ \vdots \\ e^{-j\frac{2\pi}{\lambda_0}(\sin\theta_0\cos\phi_0 p_{0,x}+\sin\theta_0\sin\phi_0 p_{M-1,y})} \\ \vdots \\ e^{-j\frac{2\pi}{\lambda_0}(\sin\theta_0\cos\phi_0 p_{N-1,x}+\sin\theta_0\sin\phi_0 p_{0,y})} \\ \vdots \\ e^{-j\frac{2\pi}{\lambda_0}(\sin\theta_0\cos\phi_0 p_{N-1,x}+\sin\theta_0\sin\phi_0 p_{M-1,y})} \end{bmatrix}\end{aligned} \tag{3.20}$$

It should be noticed that, when the beam-pattern is steered towards (θ_0, ϕ_0), the frequency-wavenumber response is simply shifted to $\mathbf{k}_0$; although the shift operation is linear in the wave-number domain, array steering is non-linear in the (θ, ϕ) domain [34]. As a result, the steered beam-pattern exhibits a distortion with respect to the ideal standard beam-pattern, and its Half Power Beam-Width (HPBW) broadens as the steering direction moves away from the array MRA.

The concept of array steering is fundamental for phased-array beamforming. Recalling (3.16), the input-output relationship of an N-element phased-array beamformer perfectly steered towards the direction of the impinging signal is given by

$$\begin{aligned}Y(f) &= \frac{1}{\sqrt{N}}\mathbf{v}^H(\theta_0, \phi_0)\mathbf{v}(\theta_0, \phi_0)A(f) + \frac{1}{N}\mathbf{v}^H(\theta_0, \phi_0)\mathbf{N}(f) \\ &= \sqrt{N}A(f) + \nu(f)\end{aligned} \tag{3.21}$$

where $\nu(f)$ is the noise at the beamformer output. It is seen that the signal is retrieved with no phase distortion: since the array is correctly steered, the phased-array perfectly re-phases the signal coming from (θ_0, ϕ_0). For the case of spatially and temporally white additive gaussian noise of power σ_n^2, it is easy to verify that the average noise power after the combiner equals σ_n^2 [4]. Henceforth, at the beamformer output the signal power is increased by N while the input noise power is not

[4] $P_N = E[\mathbf{c}^H\mathbf{N}(f)\mathbf{N}^H(f)\mathbf{c}] = \frac{1}{N}\mathbf{v}^H(\theta_0, \phi_0)E[\mathbf{N}(f)\mathbf{N}^H(f)]\mathbf{v}(\theta_0, \phi_0) = \frac{\sigma_n^2}{N}\mathbf{v}^H(\theta_0, \phi_0)\mathbf{I}_N\mathbf{v}(\theta_0, \phi_0) = \sigma_n^2$.

enhanced. Therefore, the perfectly-steered ideal phased-array introduces an *array gain* equal to N.

The beam-switching beamforming approach discussed in Chapter 5 is based on the concept of array steering: the optimal Tx/Rx beam-pattern pair is selected among a pool of pre-defined beam-patterns, which are simply steered versions of the standard array radiation pattern. In other words, the space is scanned by steering the Tx-Rx arrays in various directions and the best Tx-Rx pair in terms of average output SNR is chosen.

3.3.3 Analog and Digital Beamforming

Depending on the beamformer architecture, the weighting can be done either in the digital domain (Digital BeamForming - DBF) or in the analog domain (Analog BeamForming - ABF). In this thesis, the focus is restricted to ABF architectures with scalar weight-vectors. The reasons are the following [6]:

- ABF has lower complexity than DBF architectures, where the weighting is achieved using Finite Impulse Response (FIR) filter weights and therefore requires complex hardware.
- ABF has lower cost and power consumption than DBF, where each antenna branch needs a dedicated RF-IF chain, including Analog-to-Digital Converters (ADC)[5].
- Analog broadband weights (FIR ABF) are theoretically achievable and the resulting architecture shares a single Tx/Rx chain, but the analog implementation of FIR filter weights is very complex.

The choice of scalar ABF over DBF and broadband ABF, shared by [6] and [7], follows directly from the considerations of Chapter 2, where the importance of low-cost end-user equipment was outlined as a key-feature of 60 GHz radios. A block-scheme comparison between the ABF and DBF Rx architectures is represented in Figures 3.7 and 3.6.

[5]Or a Digital-to-Analog Converters (DAC), if the beamformer is used for transmission.

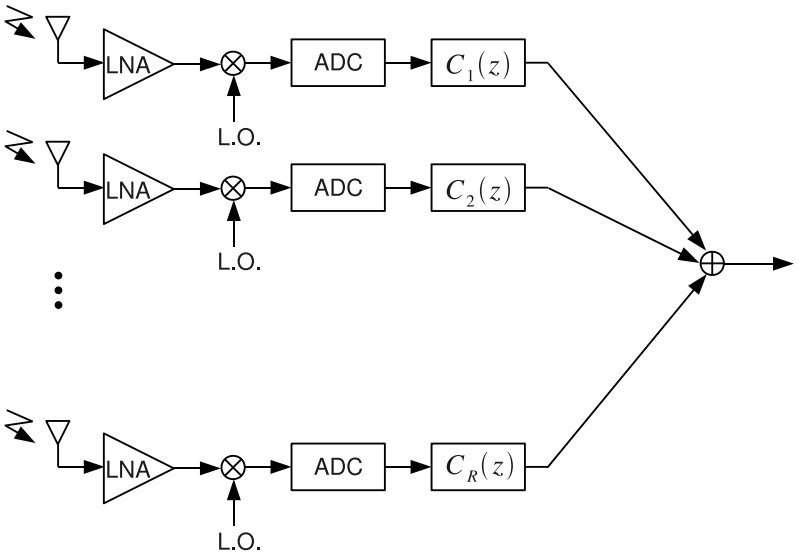

Figure 3.6: Block scheme representation of a DBF architecture. LNA = low noise amplifier, L.O. = local oscillator.

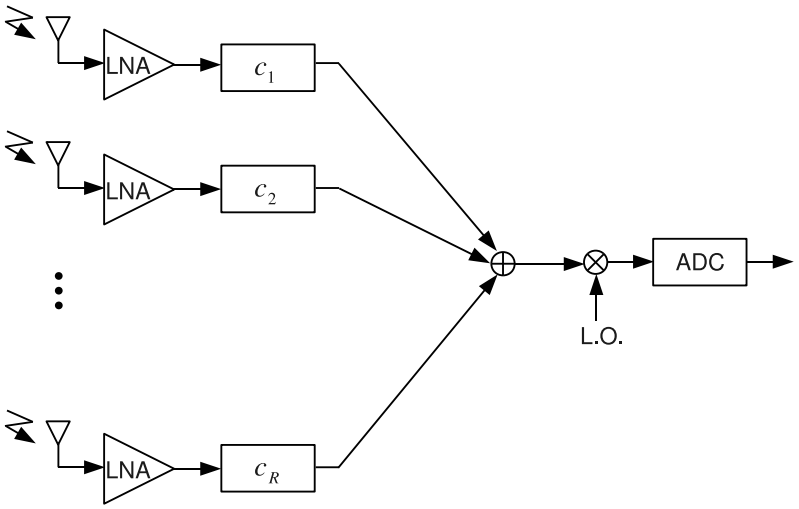

Figure 3.7: Block scheme representation of a scalar ABF architecture. LNA = low noise amplifier, L.O. = local oscillator.

3.4 Tx-Rx Analog Beamforming System Model

A block scheme representation of the considered analog Tx-Rx beamforming system model is provided in Figure 3.8, assuming T transmit and R receive antennas.

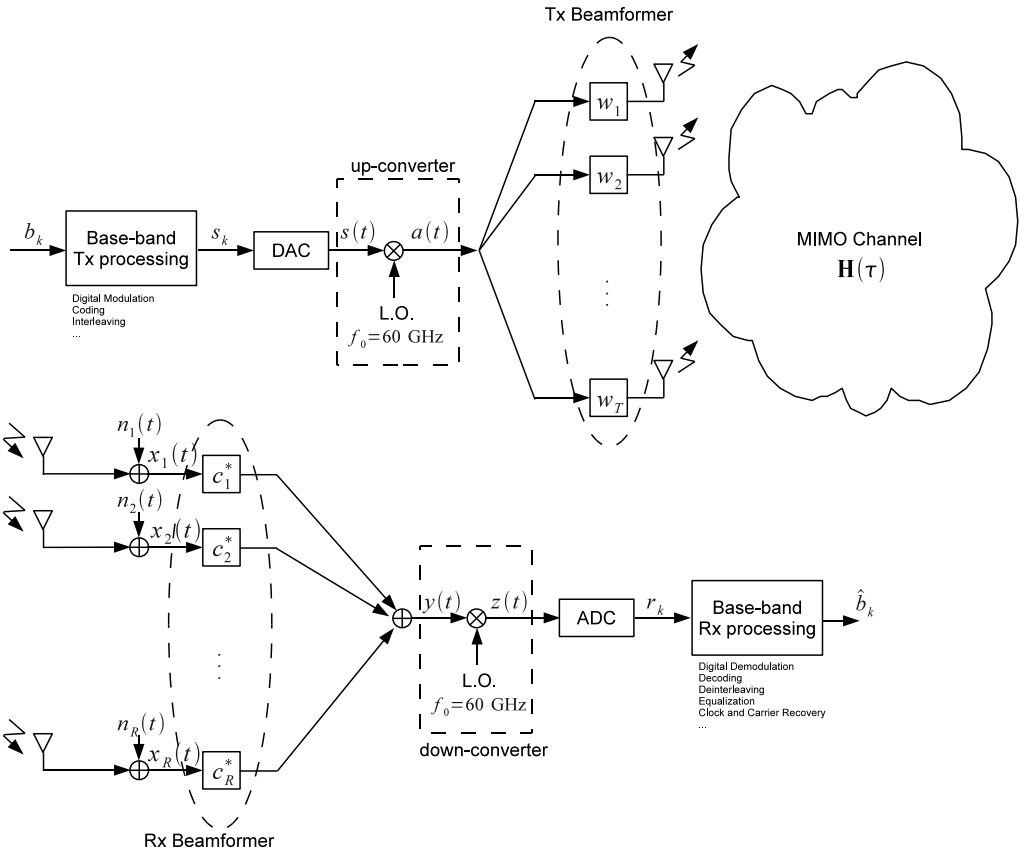

Figure 3.8: Tx-Rx analog beamforming communication chain.

The following notation is adopted:

- Discrete-time variables:
  - b_k: information bit-sequence (Tx message);
  - s_k: transmitted symbol-sequence;
  - r_k: received symbol-sequence;
  - $\hat{b}_k$: estimated bit-sequence (Rx message).

- Continuous-time variables:
  - $s(t)$: transmitted time-variant base-band wave-form;
  - $a(t)$: transmitted time-variant RF wave-form;
  - $y(t)$: time-variant received RF wave-form (after combining);
  - $z(t)$: time-variant low-pass equivalent of the received wave-form;
  - $\mathbf{w}$: $T \times 1$ ABF Tx weight-vector;

- $\mathbf{H}(\tau)$: $R \times T$ time-invariant frequency-selective multiple-input multiple-output (MIMO) channel matrix;
- $\mathbf{x}(t)$: $R \times 1$ time-variant observation vector;
- $\mathbf{n}(t)$: $R \times 1$ time-variant noise vector;
- $\mathbf{c}$: $R \times 1$ ABF Rx weight-vector.

Both Tx and Rx front-ends are based on an ABF architecture as shown in Figure 3.7. In this system configuration, only one digital stream s_k can be transmitted. Therefore, the MIMO channel matrix cannot be exploited for MIMO processing schemes: no spatial multiplexing gain can be achieved using ABF techniques [7]. For the remainder of this thesis, $\mathbf{H}(\tau)$ will be referred to as the MIMO channel matrix, but it should be clear that Tx-Rx ABF system features a single transmission stream and no MIMO beamforming solutions are addressed. Furthermore, broadband beamforming techniques cannot be implemented with the ABF architecture because of the constraint of scalar (constant across the Tx bandwidth) Tx/Rx weights. With the ABF architecture considered in this thesis, only narrowband beamforming solutions are designable, such as phased-array beamforming.

The focus of this thesis is concentrated uniquely on the central part of the block chain of Figure 3.8, that is the RF section from $a(t)$ to $y(t)$. The goal is to design a low-cost and low-complexity Tx-Rx beamforming solution to determine scalar ABF weight-vectors $\mathbf{c}$ and $\mathbf{w}$. The assumptions on the involved blocks are the following:

- Transmitted signal of power spectral density (PSD) $|A(f)|^2 = \sigma_a^2$ in the Tx bandwidth B. This corresponds to zero-mean transmitted symbols with variance σ_a^2 and ideal Tx shaping filter (zero roll-off).
- Normalized Tx and Rx beamformer weight-vectors: $||\mathbf{w}|| = 1$ and $||\mathbf{c}|| = 1$. This way, the total transmitted power is kept constant and the average SNR calculations are retained to the input SNR [6].
- Time-invariant channel: because the symbol rate is very high for realistic 60 GHz applications, the MIMO channel matrix is assumed to stay invariant during the transmission of several bursts [6].
- Spatially and temporally White Additive Gaussian Noise (AWGN) of power σ_n^2.

The time-domain input-output relationship of the RF section is given by the following expression:

$$y(t) = \mathbf{c}^H \left(\int \mathbf{H}(\tau) a(t-\tau) d\tau \right) \mathbf{w} + \mathbf{c}^H \mathbf{n}(t) \tag{3.22}$$

Equivalently, the frequency-domain relationship is given by

$$Y(f) = \mathbf{c}^H \mathbf{H}(f) \mathbf{w} A(f) + \mathbf{c}^H \mathbf{N}(f) \tag{3.23}$$

The MIMO channel matrix plays a central role in the Tx-Rx beamforming system design. This matrix embeds the steering vectors corresponding to the directions of all the transmitted and received multipath components, other than the Tx-Rx channel-response pairs. Chapter 4 is entirely dedicated to channel modeling for 60 GHz indoor environments.

4 60 GHz Channel Modeling

This chapter is entirely dedicated to 60 GHz channel modeling. The ultimate goal is to derive a model to obtain the MIMO channel matrix of Equation (3.23), in order to support system simulations for the subsequent chapter.

In the literature, there are several recent research papers on the 60 GHz frequency based on channel measurements and/or ray-tracing experiments, such as [38–46]. These papers provide insight on 60 GHz indoor propagation, but they cannot be directly applied to the transmit-receive system design. Indeed, to the best of the author's knowledge, in the literature there is no statistical channel model specific for the 60 GHz that includes the relationship between the directions of departure (DoD) and the directions of arrival (DoA) of each single multipath component. This relationship is of fundamental importance when the entire Tx-Rx system is considered: each ray is spatially filtered both at Tx and Rx sides, and therefore needs to be characterized both by its DoD and DoA[1]. For this reason, a DoD-DoA channel model for 60 GHz indoor environments is proposed. This model is semi-deterministic: it has a deterministic part based on geometrical-optics and a statistical part which is a reprise of the statistical models available in the literature. With the aid of this model, time-invariant frequency-selective MIMO channel matrix realizations can be readily obtained.

The rest of this chapter is structured as follows: Section 4.1 discusses indoor propagation at 60 GHz and describes the state-of-the-art statistical channel model (DoA-only); Section 4.2 presents a semi-deterministc DoD-DoA channel model (SDCM) and assesses its accuracy by comparing the simulation results with channel measurements available in the literature [39]. Finally, the construction of the MIMO matrix is discussed in Section 4.3.

Several Matlab tools were designed in order to implement the SDCM. For further details, the reader is referred to Appendix A.

4.1 The 60 GHz Channel

The properties of indoor propagation at 60 GHz are significantly different to those of other "traditional" bands. In [41] it has been reported that the main differences are the following:

- **Increased path loss**. Due to the shift towards higher frequencies, the free-space attenuation is higher than that of current 2.4 - 5 GHz WLAN (this can be readily verified with the Friis equation [26]);
- **Enhanced reflection and scattering**. Due to the smaller wavelength (5 mm), propagation at 60 GHz has been defined as "quasi-optical" [39, 40],

[1]It is easy to understand that the DoD and DoA of a given multipath component cannot be uncorrelated, given a specific propagation environment [47].

featuring mirror-like reflections and scattering from main objects such as walls, furniture, the floor, the ceiling.

- **Increased penetration loss**. In [22] it is reported that the penetration loss caused by typical construction materials at 60 GHz is greater than that of smaller frequencies; for this reason, it is highly likely that the receiver can only be used within the same room where the transmitter is located, and inter-room propagation can be neglected.

4.1.1 Statistical Characterization

Indoor propagation at 60 GHz may be described by the statistical model for indoor multipath propagation developed by Saleh and Valenzuela (SV) in 1987 [13] and extended to the angular domain by Spencer in 2000 [48]. This model is based on the concept of *clusters*, i.e. groups of rays closely spaced in the time and in the angular domains, and its suitability for 60 GHz channels is supported by channel measurements conducted by the IEEE TG3c [14]. The "clusterization" phenomenon is due to scattering from objects in the vicinity of the transceivers or on the reflecting surfaces [41]. A schematic representation of a clustered channel model is represented in Figure 4.1. The complex-valued low-pass channel impulse response (CIR) for this

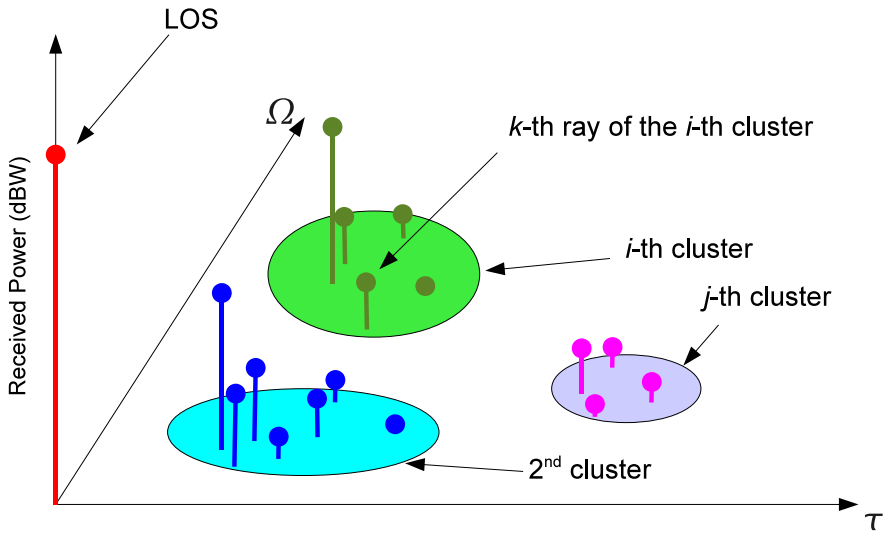

Figure 4.1: Schematic representation of a clustered channel model. Ω represents a generic angular coordinate.

model is expressed as follows:

$$h(t,\theta_{rx},\phi_{rx}) = \sum_{i=1}^{N_C}\sum_{k=1}^{N_R^{(i)}} \alpha^{(i,k)}\delta(t - T^{(i)} - \tau^{(i,k)})\delta(\theta_{rx} - \Theta_{rx}^{(i)} - \theta_{rx}^{(i,k)})\delta(\phi_{rx} - \Phi_{rx}^{(i)} - \phi_{rx}^{(i,k)}) \tag{4.1}$$

where:
- t represents the excess delay abscissa[2];
- i is the cluster index;
- k is the ray index (within a specific cluster);
- (θ_{rx}, ϕ_{rx}) correspond to the elevation and azimuth of arrival coordinates (DoA);
- $h(t, \theta_{rx}, \phi_{rx})$ is the time-invariant CIR;
- N_C is the number of clusters;
- $N_R^{(i)}$ represents the number of rays within the i-th cluster;
- $\alpha^{(i,k)}$ is the complex-valued amplitude of the k-th ray of the i-th cluster;
- $(T^{(i)}, \Theta_{rx}^{(i)}, \Phi_{rx}^{(i)})$ are the time-angular coordinates of the i-th cluster;
- $(\tau^{(i,k)}, \theta_{rx}^{(i,k)}, \phi_{rx}^{(i,k)})$ are the time-angular coordinates of the k-th ray of the i-th cluster;

The terms with superscript i are referred to as *inter-cluster* values, while those with superscript (i,k) are called *intra-cluster* terms. According to the Saleh-Valenzuela statistical model, all these values are time-varying random variables (RV). However, as pointed out in Section 1.2.1, the channel is considered as time-invariant throughout the whole thesis[3]. Nevertheless, the terms of Equation 4.1 are allowed to vary between different channel realizations, thus their statistical characterization is needed.

The cluster and ray arrival processes are both modeled as Poisson arrival processes with different rates (Λ and λ, respectively), therefore with exponentially distributed inter-arrival times. The number of clusters and rays within a specific cluster are theoretically infinite, but the contributions due to extremely delayed rays may be neglected because of their severe attenuation [13]. According to the SV model, the DoA of the received clusters is uniformly distributed (both elevation and azimuth), while the rays are locally spread around the principal ray of their cluster following a zero-mean Gaussian PDF with angular spread equal to σ_{ang}[4]. As for the probability density function (PDF) of the complex-valued amplitudes, first it is necessary to introduce the channel power delay profile (PDP).

The power delay profile (PDP) is defined as the average output power of the channel multipath components as a function of the excess delay t with respect to the arrival

[2]This was indicated with τ in Section 3.4; for notational conveniency it will be denoted by t in the sequel, since τ denotes the time of arrival of the multipath components.

[3]The less-stringent assumption of wide-sense stationary channel with uncorrelated scattering (WSSUS) for physical 60 GHz channels has been experimentally confirmed and accepted in literature [41].

[4]Actually, since the Gaussian PDF has infinite support, the angular statistics generated with this distribution must be phase-wrapped [14].

of the first path [29]. Under the WSSUS assumption (and thus for time-invariant channels), the PDP can be calculated using the following equation:

$$P(t) = E[|h(t, \theta_{rx}, \phi_{rx})|^2] \tag{4.2}$$

where the expectation is taken with respect to different channel realizations, and the angular dependence is averaged out. Recalling (4.1), the expression of the PDP becomes:

$$\begin{aligned} P(t) &= \sum_{i}^{N_C} \sum_{k}^{N_R^{(i)}} E[|\alpha^{(i,k)}|^2] \delta(t - T^{(i)} - \tau^{(i,k)}) \\ &= \sum_{i}^{N_C} \sum_{k}^{N_R^{(i)}} \overline{\beta^{(i,k)}} \delta(t - T^{(i)} - \tau^{(i,k)}) \end{aligned} \tag{4.3}$$

According to the Saleh-Valenzuela model, the PDP is a result of the superimposition of two exponentially-decaying power profiles occurring simultaneously at inter-cluster and intra-cluster levels. The equations of these profiles are the following:

$$\begin{cases} \overline{\beta^{(i,1)}} = K_{LOS} \exp\{-T^{(i)}/\Gamma\} & \text{Inter-cluster} \\ \overline{\beta^{(i,k)}} = \overline{\beta^{(i,1)}} K_C \exp\{-(\tau^{(i,k)}/\gamma\} & \text{Intra-cluster} \end{cases} \tag{4.4}$$

where K_{LOS}, K_C, Γ and γ are the inter-cluster and intra-cluster Rician factors and decay factors, respectively. The Rician factors account for the small-scale fading that occurs because of the presence of a stronger path and several secondary independent scattered rays[5] [41]. A representation of the PDP of Equation (4.4) is illustrated in Figure 4.2.

The PDP represents the average power profile, but each channel realization is allowed to vary about the average; according to the Saleh-Valenzuela model, the instantaneous power follows a log-normal distribution[6] (normal in dB) centered on the PDP with root-mean-square (RMS) equal to σ_s. The phase of the complex-valued amplitudes are instead modeled as uniform RV.

4.1.2 Channel Parameters

The statistical characterization of the RVs of the Saleh-Valenzuela model is summarized in Table 4.1, and the parameters are listed in Table 4.2.

[5]This situation occurs at both levels: the LOS and the reflected clusters at inter-cluster level, the principal cluster ray and the scattered components at intra-cluster level.

[6]Actually, it is well established in the literature that both the log-normal PDF and the Rayleigh distribution fit very well the measurements that have been collected in indoor environments [28]. Saleh-Valenzulela [13] stated that the log-normal distribution fitted their measurements better than the Rayleigh density, but eventually the latter was chosen for its analytical simplicity (being a one-parameter PDF). The TG3c preferred the log-normal distribution, which has a compelling empirical justification: the multipath phenomenon can be described as a multiplicative process (multiple reflections), and the multiplication of signal amplitudes gives rise to a log-normal distribution exactly as an additive process results in a normal distribution.

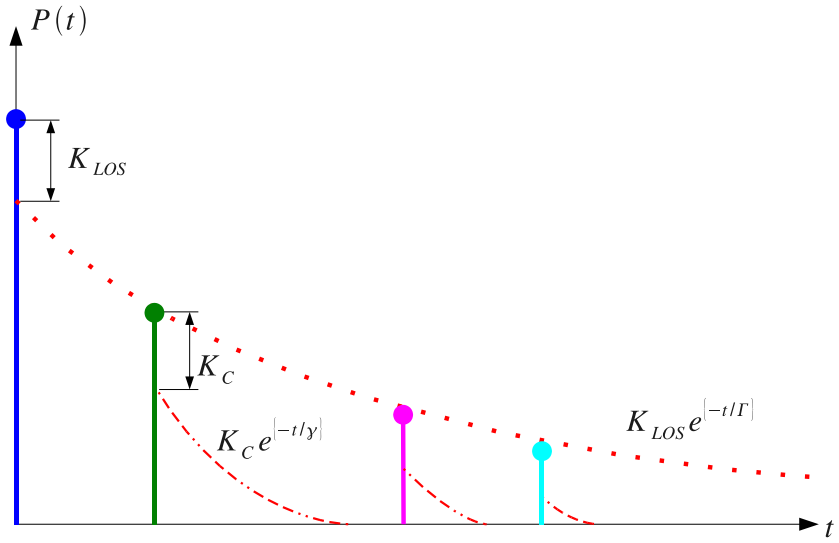

Figure 4.2: Power delay profile of the 60 GHz channel.

Table 4.1: Random variables of the Saleh-Valenzuela statistical model.

RV	*Unit*	*PDF*
$T^{(i)} - T^{(i-1)}$	[s]	$\sim \text{Exp}(\Lambda)$
$\tau^{(i,k)}\tau^{(i,k-1)}$	[s]	$\sim \text{Exp}(\lambda)$
$\Theta_{rx}^{(i)}$	[rad]	$\sim \mathcal{U}(0, 2\pi)$
$\Phi_{rx}^{(i)}$	[rad]	$\sim \mathcal{U}(0, 2\pi)$
$\theta_{rx}^{(i,k)}$	[rad]	$\sim \mathcal{N}(\Theta_{rx}^{(i)}, \sigma_{ang})$
$\phi_{rx}^{(i,k)}$	[rad]	$\sim \mathcal{N}(\Phi_{rx}^{(i)}, \sigma_{ang})$
$\lvert\alpha^{(i,k)}\rvert^2$	[W]	$\sim \text{Log-}\mathcal{N}(P(T^{(i)} - \tau^{(i,k)}), \sigma_s)$
$\angle\, \alpha^{(i,k)}$	[rad]	$\sim \mathcal{U}(0, 2\pi)$

To the best of the author's knowledge, the state-of-the-art statistical channel model for 60 GHz indoor propagation is the Saleh-Valenzuela model as presented in the previous section, whose suitability to the 60 GHz case was confirmed both by experimental investigations [14] and ray-tracing experiments [39, 49].

The IEEE TG3c adopted this model and extracted the channel parameters through an extensive measurement campaign in different environments and in LOS/NLOS configurations. The considered environments were the following: residential, office, library, desktop and kiosk. The parameters extracted for the residential environment

Table 4.2: Parameters of the Saleh-Valenzuela channel model. The measurement results for the "Residential Room" environment extracted by the TG3c are listed in the last column.

Parameter	*Unit*	*Description*	*TG3c value*
Λ	[1/ns]	Inter-cluster interarrival rate	0.21
λ	[1/ns]	Intra-cluster interarrival rate	0.77
Γ	[ns]	Inter-cluster decay factor	4.19
γ	[ns]	Intra-cluster decay factor	1.07
σ_{ang}	[deg]	Intra-cluster angular RMS	8.32
σ_s	[dB]	Small-scale fading RMS	1.26
K_{LOS}	[dB]	Inter-cluster Rician K-factor	-10
K_C	[dB]	Intra-cluster Rician K-factor	-10

are reported in Table 4.2. For more insight on the measurement setup, parameter extraction procedure and a more detailed description of the environments, the reader is referred to [14].

The only modification to the Saleh-Valenzuela model introduced by the TG3c concerns the number of cluster and rays within a cluster. According to the statistical model both quantities are theoretically infinite, being described by two independent Poisson arrival processes. Naturally, this feature is quite impractical in the perspective of channel simulations. Therefore, the TG3c tackled this issue by measuring the average number of observed clusters and deriving the average number of rays per cluster[7], respectively denoted with $\overline{N_C}$ and $N_R^{(i)}$. The actual number of clusters and rays of a specific realization is then distributed according to a Poisson distribution of parameters $\overline{N_C}$ and $N_R^{(i)}$.

Finally, the TG3c channel model assigns power equal to 1 W and delay equal to 0 ns to the LOS path, and NLOS realizations can be obtained by simply removing the direct component [14]. The reader is addressed to [14] for a detailed mathematical description of the TG3c channel models.

4.2 Semi-Deterministic DoD-DoA Channel Model (SDCM)

The modeling work of Saleh-Valenzuela and the measurements collected by the IEEE TG3c provide significant insight on the 60 GHz propagation mechanisms, but their results are not directly applicable to the Tx-Rx system design. The reasons are the

[7] $\overline{N_R^{(i)}} = \lambda T_{obs}$, where T_{obs} is the observation time. Considering the exponentially-decaying power profile, the intra-cluster PDP reduces to 1/10th of its initial power for $T_{obs} = \gamma \ln(10)$. Therefore, $\overline{N_R^{(i)}} = \lambda\gamma \ln(10)$.

following:

- *Lack of information on the DoD.* Recalling (4.1), the transmitted wavenumber is not considered.
- *Lack of DoD-DoA model.* This follows directly from the statement above: not only it is necessary to introduce the transmit wavenumber, but the relationship between the transmit and receive angles must be properly characterized[8].

If these shortcomings are not overcome, it will be not possible to generate proper realizations of the MIMO channel matrix of Equation (3.23), which is a function both of the Tx and the Rx wavenumbers. The need for a DoD-DoA model has been already claimed in [8, 40, 50], but no statistical characterization is currently available for the 60 GHz.

In the literature, there are several modeling strategies for the MIMO wireless channel. A survey of the most important approaches may be found in [47]. The available MIMO models are classified into physical models and analytical models. In the first category, the double-directional channel impulse response (i.e. including information on the DoDs and DoAs) is found on the basis of electromagnetic wave propagation between the Tx and Rx in a given propagation environment. Each multipath component is modeled in terms of DoD, DoA, delay and complex-valued amplitude, and these parameters are independent on antenna configurations and system bandwidth. Examples of physical models are Ray-Tracing (RT), Geometry-based Stochastic Channel Models (GSCM) and fully-stochastic models, such as the Saleh-Valenzuela (DoA only). Being independent on the Tx-Rx antenna configurations, physical models offer the advantage that different antenna types can be evaluated for the same propagation environment.

Analytical models directly characterize the MIMO channel matrix (i.e. all the CIR pairs between the individual Tx-Rx antennas) without explicitly accounting for wave propagation [47]. The double-directional channel response and the Tx-Rx antenna configurations is therefore subsumed in the MIMO matrix. This category can be subdivided into two classes: propagation-based models and correlation-based models. An example of the first category is the finite scatterer model, where the MIMO matrix can be straightforwardly constructed given a double-directional channel model and the Tx-Rx antenna configurations. With correlation-based models, realizations of the MIMO matrix are obtained stochastically after specifying a correlation matrix that describes the MIMO channel spatial statistics. Examples of correlation-based models are the Kronecker MIMO model and its extension, known as the Weichselberger model [51]. However, examples of correlation-based analytical models specifically parameterized for 60 GHz case have not been found in the literature.

The solution proposed here consists in a *semi-deterministic DoD-DoA model* (SDCM) based on geometrical optics (RT) and on the available statistical model. The double-

[8]Extending the uniformly-distributed model to the DoD of the clusters is not likely to be correct: once the position of the transceivers in a specific single-room environment is given, the transmitted directions and the received ones cannot be uncorrelated [47].

directional channel impulse response is found following a GSCM approach, then the MIMO matrix is constructed by incorporating the Tx-Rx antenna array configuration (number of elements and sensor displacement) adopting a finite scatterer model. In this manner, a given double-directional CIR may be evaluated for different antenna sizes. The RT approach for mmWave channels was verified to show good agreement with channel measurements in several research papers (e.g. [4, 39]), especially in environments with limited scattering. This is motivated by the quasi-optical nature of propagation at mmWave frequencies, with mirror-like reflections and increased penetration loss, enhanced scattering and reduced diffraction.

Recalling (4.1) and including the information on the DoD, the double-directional CIR becomes:

$$\begin{aligned} h(t,\theta_{tx},\phi_{tx},\theta_{rx},\phi_{rx}) = \sum_{i=1}^{N_C}\sum_{k=1}^{N_R^{(i)}} \alpha^{(i,k)}\delta(t-T^{(i)}-\tau^{(i,k)}) \\ \cdot\,\delta(\theta_{tx}-\Theta_{tx}^{(i)})\delta(\phi_{tx}-\Phi_{tx}^{(i)}) \\ \cdot\,\delta(\theta_{rx}-\Theta_{rx}^{(i)}-\theta_{rx}^{(i,k)})\delta(\phi_{rx}-\Phi_{rx}^{(i)}-\phi_{rx}^{(i,k)}) \end{aligned} \tag{4.5}$$

From (4.5) it can be observed that the $N_R^{(i)}$ rays of the i-th cluster share one common DoD $(\Theta_{rx}^{(i)}, \Phi_{tx}^{(i)})$. Therefore, each channel realization features N_C clusters and $N_R = \sum_i N_R^{(i)}$ rays, $N_R \geq N_C$ (see Figure 4.3).

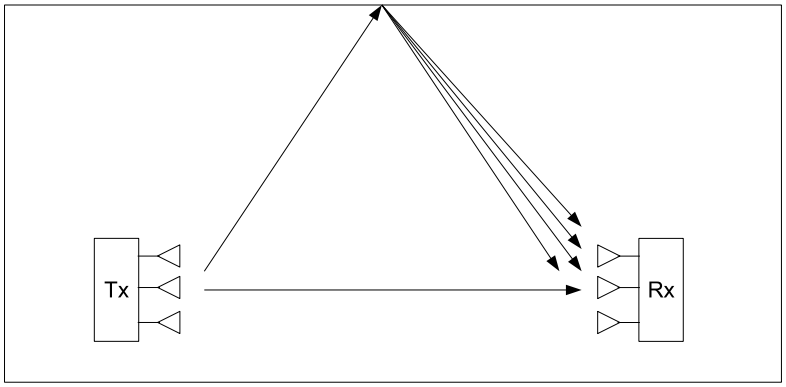

Figure 4.3: Ray clustering: N_C transmitted signal paths result in N_R received rays, with $N_R \geq N_C$.

The SDCM is composed of the following two parts:

- **Deterministic part**. Once the building superstructure and the Tx/Rx positions and orientations are defined, the following terms are readily calculated via geometrical optics: number of clusters N_C, cluster DoD $(\theta_{tx}^{(i,1)}, \phi_{tx}^{(i,1)})$, cluster DoA $(\theta_{rx}^{(i,1)}, \phi_{rx}^{(i,1)})$, cluster path length $d^{(i,1)}$, cluster time-of-arrival (ToA)

$T^{(i,1)}$. This way, almost all of the inter-cluster characterization is deterministically calculated.

- **Statistical part**. Clusters are statistically generated. The intra-cluster model coincides exactly with the Saleh-Valenzuela statistical description of Section 4.1.1. At inter-cluster level, the instantaneous power of the principal ray of each cluster is modeled in the following manner:

$$|\alpha^{(i,1)}|^2|_{dB} = PL(d^{(i,1)})|_{dB} + G^{(i)}_{refl}|_{dB} \tag{4.6}$$

where $PL(d)$ is the path loss (calculated with the Friis equation[9] [26]) and $G^{(i)}_{refl}$ is a Gaussian (in dB) RV whose parameters $\mu^{(i)}_S$ and $\sigma^{(i)}_S$ depend on the number of reflections that the i-th cluster undergoes. In [40], the values of these parameters were measured at 60 GHz for typical construction materials[10]. These values are listed in Table 4.3. The phase of the principal rays of the clusters is uniformly-distributed.

The positions and orientations of the transceivers are allowed to vary randomly between channel realizations. The following models are assumed:

  - *TRx positions*. The (x, y, z) coordinates of the transceivers are modeled as uniform RV variables in the ranges (L, W, H) (room length, width and height).
  - *TRx orientations*. Since it is not likely that the user of a 60 GHz radio will always a obtain perfect alignment between the transceivers (i.e. the look-directions of both the Tx and Rx coincide with the LOS), the main response abscissae (MRA) of the Tx and Rx arrays are allowed to vary between channel realizations. This is accounted for by introducing a rotation RV (horizontal plane) and a tilting RV (vertical plane) with respect to the LOS direction, both described by zero-mean Gaussian PDFs with (horizontal and vertical) and RMS equal to σ_{look} (see Figure 4.4).

In order to obtain SDCM channel realizations, a geometrical-optics tool was designed in Matlab (see Appendix A). The following simplifications are introduced:

- Reflections of order higher than 2nd are neglected. According to [40], reflections of higher order bring negligible contribution to the total received power. Referring to the channel model classification of [47], this feature classifies the SDCM as a double-bounce GSCM.
- The propagation environment is assumed to be an empty room with no furniture, windows nor doors.

[9] $PL(d) = 20\log_{10}\left(\frac{\lambda}{4\pi d}\right)$.

[10] Interior walls are made of two plasterboard sheets with an air gap between them, and outer walls are made of concrete covered by plasterboard. For more details, the reader is addressed to [40].

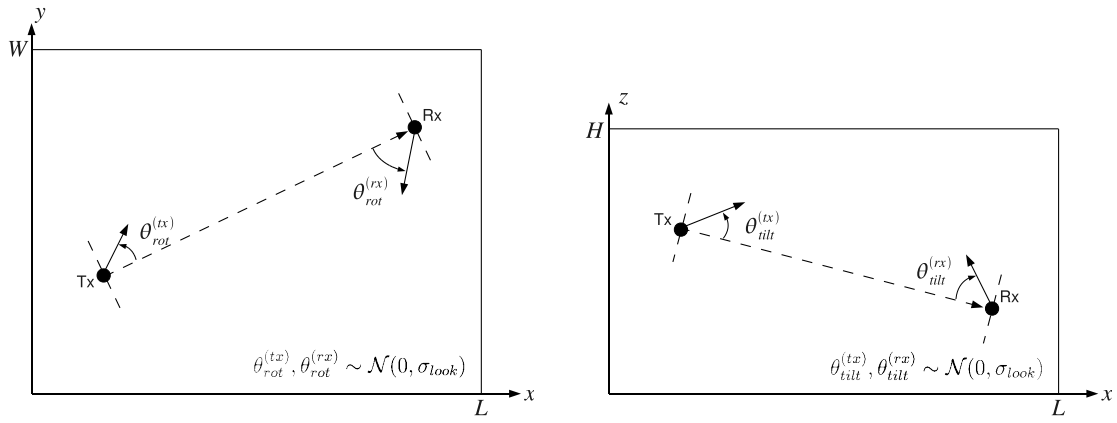

(a) Horizontal plane (xy) (b) Vertical plane (xz)

Figure 4.4: Tx and Rx are allowed to rotate on the horizontal and vertical planes, thus deviating away from the perfect alignment condition.

- No intra-room propagation is considered.

It should be noticed that the SDCM is not meant to substitute a ray-tracer, where the characterization of all rays and clusters is obtained entirely deterministically, given a thorough description of the propagation environment (including the position, volume and material of objects and furniture). On the contrary, the SDCM applies the basic rules of geometrical optics in a very simple environment (a six-walled empty space) to determine the DoD-DoA correspondence, but then leaves space for a statistical description of the other channel parameters. Henceforth, obtaining channel realizations with the SDCM is reasonably expected to be faster, more scalable and low-complexity than with a proper ray-tracer. In order for the channel realizations to be accurate, however, accurate channel parameters are required. The accuracy of the SDCM is evaluated in Section 4.2.2.

4.2.1 SDCM Parameters

The SDCM and the TG3c/Saleh-Valenzuela models are identical at intra-cluster level; therefore, the intra-cluster channel parameters for the SDCM are directly taken from the TG3c measurements [14]. The "residential room" environment is chosen because of its simple geometry (no furniture, no objects), and thus similarity to the geometry setup of the SDCM. The parameters of the log-normal reflection coefficients, used to model the instantaneous intensity of the clusters, are taken from [40]. The parameters adopted in the thesis are summarized in Table 4.3, and will not be changed throughout the rest of the report.

In the following pages, a LOS and a NLOS channel realizations generated with the SDCM are given as examples in Figures 4.5 through 4.10. The clustering phenomenon is evident from both realizations, both in the time and in the angular

Table 4.3: Parameters of the SDCM channel model.

Parameter	*Description*	*Value*	*Source*
$\mu_S^{(i)}$ - 1st	1st-order reflection mean	- 10 dB	[40]
$\sigma_S^{(i)}$ - 1st	1st-order reflection RMS	4 dB	[40]
$\mu_S^{(i)}$ - 2nd	2nd-order reflection mean	- 16 dB	[40]
$\sigma_S^{(i)}$ - 2nd	2nd-order reflection RMS	5 dB	[40]
σ_{look}	Orientation deviation RMS	30°	-
λ	Intra-cluster interarrival rate	0.77 ns $^{-1}$	[14]
γ	Intra-cluster decay factor	1.07 ns	[14]
σ_{ang}	Intra-cluster angular RMS	8.32°	[14]
σ_s	Small-scale fading RMS	1.26 dB	[14]
K_C	Intra-cluster Rician K-factor	-10 dB	[14]
(W, L, H)	Room width, length, height	(6.85, 3.57, 2.47) m	[14]

domains. In LOS scenarios, the direct path is clearly predominant with respect to the reflected rays. The first-order reflections are about 10 - 15 dB below the LOS component and the second-order reflections are approximately 20 - 30 dB weaker. In [40] it was reported that, despite the difference in power levels, these paths provide enough power to establish a communication link using robust modulation and coding schemes.

From the angular profiles it is seen that the received paths are separated in the angular domain[11], therefore a beamformer could improve the system performance by providing gain along the direction of the predominant components (the direct path or the strongest reflection). The channel realizations also exhibit a time-dispersive nature; therefore, considering the large bandwidth of 60 GHz applications, it is natural to expect frequency-selectivity from the channel[12]. In Section 5.3.3, the average coherence bandwidth of the 60 GHz channel is extracted using Monte Carlo simulations and is shown to be about 250 MHz, by far smaller than the transmission bandwidth (which can reach up to 2.16 GHz [16]). Hence, the MIMO channel matrix needs to be modeled in a broadband manner. A beamforming system could effectively mitigate the multipath fading by spatially filtering out secondary components.

[11]Notice that only the elevation angle was plotted; however, rays are also separated in the azimuth domain.

[12]The narrowband assumption regards only the steering vector model.

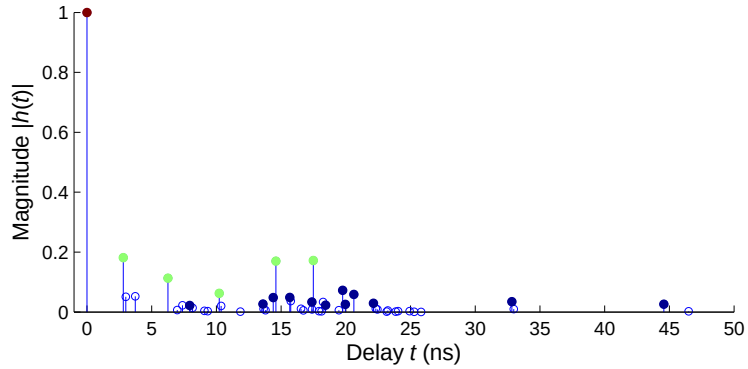

Figure 4.5: LOS channel realization obtained with the SDCM: amplitude profile.

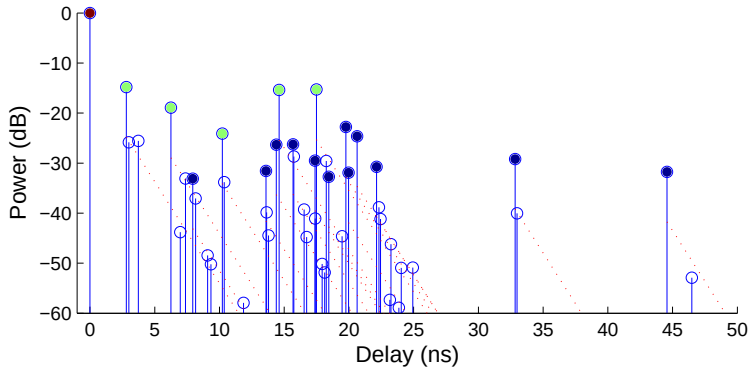

Figure 4.6: LOS channel realization obtained with the SDCM: power profile.

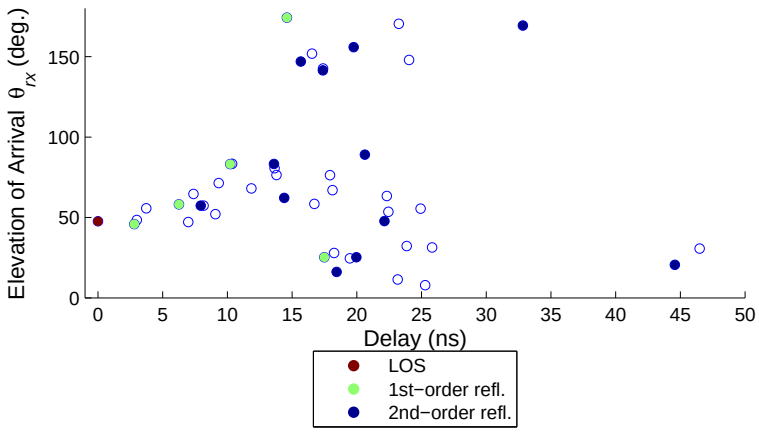

Figure 4.7: LOS channel realization obtained with the SDCM: angular profile (elevation).

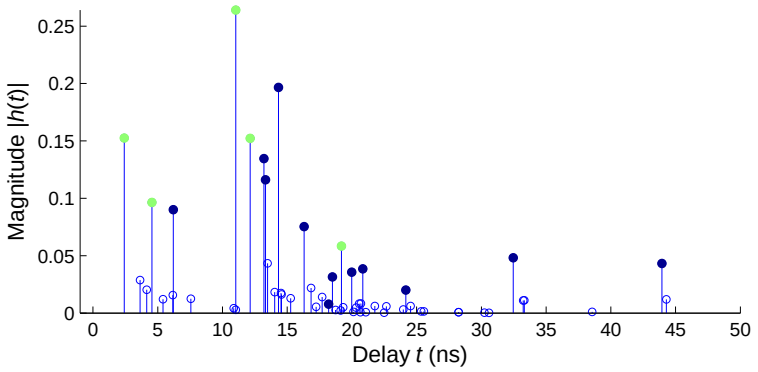

Figure 4.8: NLOS channel realization obtained with the SDCM: amplitude profile.

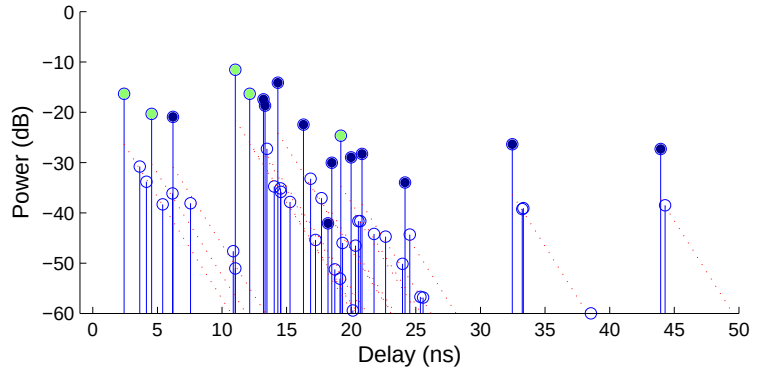

Figure 4.9: NLOS channel realization obtained with the SDCM: power profile.

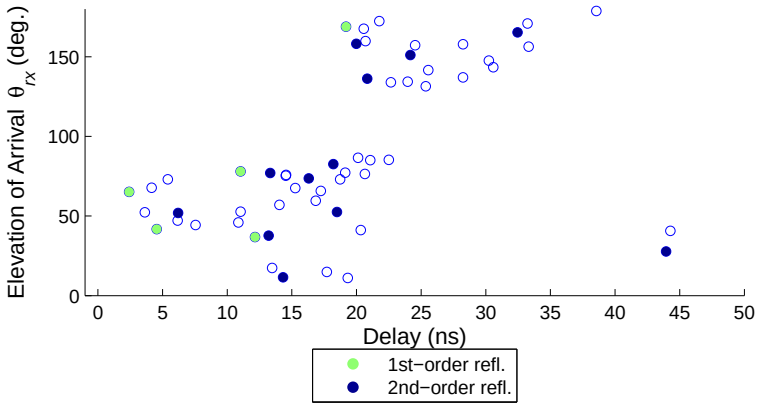

Figure 4.10: NLOS channel realization obtained with the SDCM: angular profile (elevation).

4.2.2 SDCM Accuracy Assessment

The SDCM applies the basic rules of geometrical optics in a very simple propagation environment in order to obtain the DoD-DoA correspondence of each ray and cluster, then it generates the cluster amplitudes and characterizes intra-cluster rays in a statistical manner. The semi-deterministic approach is inherently different from a ray-tracer, which is entirely deterministic and requires a detailed model of the propagation environment. At the same time, the SDCM differs from fully-statistical models such as the TG3c/Saleh-Valenzuela, where rays are generated regardless of the building superstructure and a DoD characterization is missing.

In [52], the National Institute of information and Communications Technology (NICT, affiliated to the TG3c) compared their channel measurements with a ray-tracing experiment in the residential environment, showing good agreement between the results. The measurement results are illustrated in Figure 4.11a. In order to assess the validity of the proposed SDCM, channel realizations were generated in the same environment with the same measurement setup of [52] and compared with the channel measurements collected by the NICT. The statistical parameters employed are reported in Table 4.3, and the simulation results are presented in Figure 4.11b. A detailed description of the simulation setup can be found in Appendix A.

Unfortunately, in [52] no quantitative results were provided, therefore it is hard to perform a comparison using quantitative criteria. Nonetheless, in general, strong resemblance in cluster shape and location is observed between the results derived from measurement and simulation. The clustering phenomenon is captured in both experiments. The SDCM simulation retrieves one LOS component, 4 first-order reflections and 7 second-order reflections. Each cluster formation is the result of a unique path between the transmitter and the receiver. However, due to the specific simulation geometry (the transceivers are located exactly along the horizontal axis of symmetry of the room, with equal spacing from the walls, as illustrated in Figure A4), some of these clusters are merged into larger clusters. The spatio-temporal coordinates of the main clusters are listed in Table 4.4.

From Table 4.4 and Figure 4.11 it is seen that almost all measured clusters are retrieved by the SDCM simulation, and the time-angular location of the centers of the clusters is exactly equal in both experiments. The most delayed cluster of Figure 4.11b is not present in the measurement data. This cluster corresponds to a 2nd-order path lying along the LOS direction and bouncing on the back-walls. Because of the specific experiment geometry, this path is blocked by the volume of the measurement equipment (covered by electromagnetic absorbers [52]); however, such equipment does not physically exist in the simulation.

The same color convention was employed (the color-bar of Figure 4.11b is in dB), showing in general a good resemblance also as far as the cluster amplitudes are concerned. No information on the measured power delay profile is provided in [52], therefore an accurate quantitative comparison between the amplitudes is not possible.

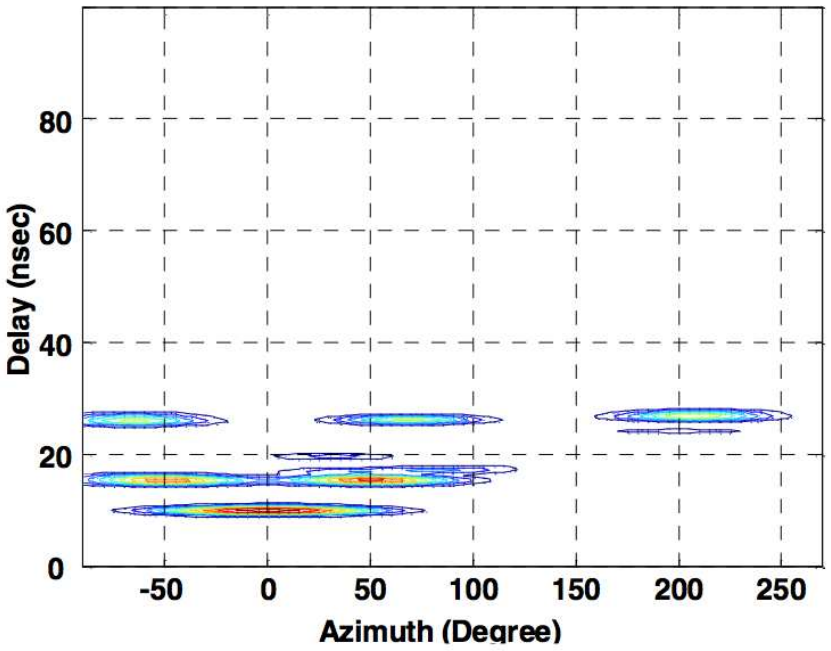

(a) NICT measurements (©IEEE 2007).

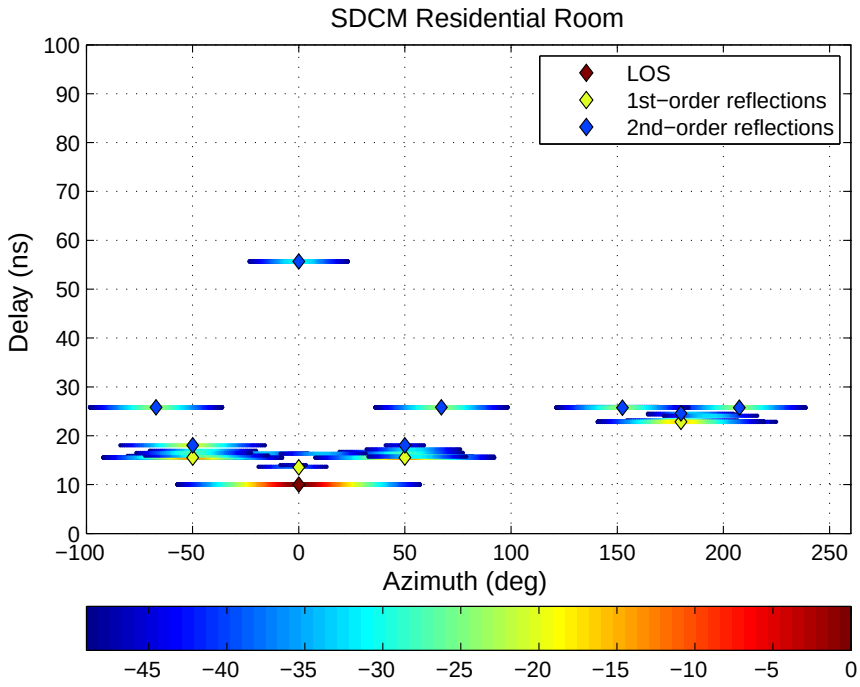

(b) SDCM simulation results.

Figure 4.11: Comparison between the NICT measurements (source: [52]) and the SDCM simulation results in the residential LOS environment.

Table 4.4: Cluster center's coordinates in the measurement and in the SDCM.

Cluster Arrival Angle	Cluster Arrival Time (ns)	Exist in NICT Measurement	Exist in SDCM Simulation
0°	10	Yes	Yes
−50°	15.5	Yes	Yes
50°	15.5	Yes	Yes
−74°	25.75	Yes	Yes
74°	25.75	Yes	Yes
152.5°, 207.5°	25.75	Yes (merged)	Yes
180°	22.85	Yes	Yes
0°	55	No	Yes

It should be noticed that Figures 4.11a and 4.11b actually do not represent the channel time-azimuth response alone. Since a Rx antenna had to be used to collect the measurements, the observed values correspond to the channel time-azimuth response filtered by the Rx antenna beam-pattern. This is the reason why the LOS and all other rays are not represented as a Dirac delta in the time and azimuth domains, and appear "stretched" in the azimuth domain. In order to represent comparable results, a virtual antenna with a radiation pattern resembling the one employed by the NICT was introduced in the simulations[13]. More insight on this point is provided in Appendix A.

In conclusion, the simulation results obtained with the SDCM strongly resemble the channel measurements collected by the NICT in terms of cluster location and shape. As reported in [52], the differences between the two figures may be explained by the presence of additional scatterers in the real scenario, by non-perfect statistical parameters in the SDCM and by the effects of the measurement equipment. For instance, the measured residential room features two large windows and one door, which are not modeled in the SDCM. Nevertheless, despite the discrepancies with the measurement data, the SDCM is seen to capture the essence of the spatial-temporal characteristics of the 60 GHz channel, and can be therefore considered a valid approach to obtain the DoD-DoA relationship that is fundamental to construct the 60 GHz MIMO channel matrix.

[13]The SDCM generates each ray as perfect impulse (with infinite resolution) along the following abscissae: $(t, \theta_{rx}, \phi_{rx}, \theta_{tx}, \phi_{tx})$. Measuring these Dirac deltas would require equipment with infinite bandwidth and infinitesimal HPBW.

4.3 Building the MIMO Matrix

The SDCM generates the cluster structures and characterizes each ray in terms of ToA, DoD, DoA and complex-valued amplitude. This information can be used to construct the MIMO channel matrix of Equations (3.22) and (3.23), which is the central part of the Tx-Rx beamforming system. Adopting an approach similar to the one outlined in [53] and assuming a $T \times R$ MIMO system, the following quantities can be defined:

- *Tx steering matrix* $\mathbf{V}(\theta_{tx}, \phi_{tx})$, a $T \times N_C$ is a collection of the steering vectors corresponding to all the DoD:

$$\mathbf{V}(\theta_{tx}, \phi_{tx}) = [\mathbf{v}(\Theta_{tx}^{(1)}, \Phi_{tx}^{(1)}), \ldots, \mathbf{v}(\Theta_{tx}^{(N_C)}, \Phi_{tx}^{(N_C)})] \tag{4.7}$$

- *Rx steering matrix* $\mathbf{V}(\theta_{rx}, \phi_{rx})$, a $R \times N_R$ is a collection of the steering vectors corresponding to all the DoA:

$$\mathbf{V}(\theta_{rx}, \phi_{rx}) = [\mathbf{v}(\theta_{rx}^{(1,1)}, \phi_{rx}^{(1,1)}), \ldots, \mathbf{v}(\theta_{rx}^{(N_C, N_R^{(N_C)})}, \phi_{rx}^{(N_C, N_R^{(N_C)})})] \tag{4.8}$$

- *Fading matrix* $\mathbf{B}(f)$, a $N_R \times N_C$ matrix defined as follows:

$$\begin{aligned} \mathbf{B}(f) &= \begin{bmatrix} \mathcal{B}^{(1)}(f) & 0 & \cdots & 0 \\ 0 & \mathcal{B}^{(2)}(f) & \cdots & 0 \\ \vdots & \vdots & \ddots & \vdots \\ 0 & 0 & \cdots & \mathcal{B}^{(N_C)}(f) \end{bmatrix} \\ &= \operatorname{diag}\{\mathcal{B}^{(1)}(f), \ldots, \mathcal{B}^{(N_C)}(f)\} \end{aligned} \tag{4.9}$$

  where

$$\mathcal{B}^{(i)}(f) = \begin{bmatrix} \alpha^{(i,1)} \exp\{-j2\pi f(T^{(i)} - \tau^{(i,1)})\} \\ \vdots \\ \alpha^{(i,N_R^{(i)})} \exp\{-j2\pi f(T^{(i)} - \tau^{(i,N_R^{(i)})})\} \end{bmatrix}, \; i = 1, \ldots, N_C \tag{4.10}$$

In this manner, the contribution of the k-th ray of the i-th cluster to the MIMO matrix is given by:

$$\mathbf{H}^{(i,k)}(f) = \mathbf{v}(\theta_{rx}^{(i,k)}, \phi_{rx}^{(i,k)}) \exp\{-j2\pi f(T^{(i)} - \tau^{(i,k)})\} \mathbf{v}^H(\Theta_{tx}^{(i)}, \Phi_{tx}^{(i)}) \tag{4.11}$$

The MIMO channel matrix can be therefore be expressed as follows:

$$\mathbf{H}(f) = \mathbf{V}(\theta_{rx}, \phi_{rx}) \mathbf{B}(f) \mathbf{V}^H(\Theta_{tx}, \Phi_{tx}) \tag{4.12}$$

where the angular dependency has been suppressed for notational conveniency. Due to the narrowband assumption, the steering matrices are constant across the transmission bandwidth; the time-domain version of (4.12) is therefore given by:

$$\mathbf{H}(t) = \mathbf{V}(\theta_{rx}, \phi_{rx}) \mathcal{F}^{-1}\{\mathbf{B}(f)\} \mathbf{V}^H(\Theta_{tx}, \Phi_{tx}) \tag{4.13}$$

Recalling Equations (3.23) and (3.17), the input-output relationship of the Tx-Rx system becomes:

$$\begin{aligned} Y(f) &= \mathbf{c}^H \mathbf{H}(f)\mathbf{w}A(f) + \mathbf{c}^H \mathbf{N}(f) \\ &= \mathbf{c}^H \mathbf{V}(\theta_{rx}, \phi_{rx})\mathbf{B}(f)\mathbf{V}^H(\theta_{tx}, \phi_{tx})\mathbf{w}A(f) + \mathbf{c}^H \mathbf{N}(f) \\ &= \sum_{i}^{N_C} \sum_{k}^{N_R^{(i)}} \Upsilon(\theta_{rx}^{(i,k)}, \phi_{rx}^{(i,k)})\alpha^{(i,k)} \exp\{-j2\pi f(T^{(i)} - \tau^{(i,k)})\}\Upsilon^H(\Theta_{tx}^{(i)}, \Phi_{tx}^{(i)})A(f) \\ &+ \mathbf{c}^H \mathbf{N}(f) \end{aligned} \tag{4.14}$$

which shows that the Tx and Rx beamformers weight each ray depending on its DoD and DoA, respectively. The weights applied by a R-element beamformer range from 0 to $\sqrt{R}$, which respectively correspond to a null in the beam-pattern and perfect alignment. For the considered case of spatially and temporally white additive Gaussian noise of power σ_n^2 and normalized weight-vector $\mathbf{c}$ (see Section 3.3.2), the Rx combiner averages out the R noise contributions, and the noise output power equals the input noise power at each antenna.

4.4 Conclusion

In this chapter, the topic of channel modeling was discussed. The goal was to derive a channel model to generate time-invariant frequency-selective 60 GHz MIMO channel realizations that could be directly plugged into the Tx-Rx system of Equation (3.23).

The propagation characteristics of the 60 GHz indoor radio channel were presented in Section 4.1. It was argued that the fully-statistical characterization of the Saleh-Valenzuela model [13], adopted by the IEEE TG3c, provides insight into the 60 GHz channel but fails to provide a DoD-DoA model.

Since this information is fundamental in order to construct the MIMO matrix, another modeling strategy must be developed. In Section 4.2, a semi-deterministic channel model (SDCM) was presented. The SDCM is based on geometrical optics, thus the DoD-DoA correspondence is deterministically calculated given a specific problem geometry. The remaining channel information (e.g. rays complex-valued amplitudes, cluster characteristics) is generated statistically as in the Saleh-Valenzuela/TG3c channel model. The inputs of the SDCM are the room size (assuming no objects/furniture) and the position/orientation of the transceivers, which varies randomly between channel realizations. In the landscape of the available MIMO channel models [47], the SDCM can be considered a finite scatterer model where the double-directional CIR is determined using a double-bounce GSCM approach.

The statistical channel parameters and the room geometry used throughout this thesis are reported in Table 4.3, and correspond to the "Residential Room" environment studied by the IEEE TG3c. In Section 4.2.2, the SDCM simulation results are compared with the channel measurements collected by the IEEE TG3c in the residential environment, showing consistency between the two experiments.

Finally, in Section 4.3 it is shown how the MIMO matrix can be constructed mathematically starting from the results of the SDCM; once this frequency-selective matrix is available, joint Tx-Rx beamforming schemes can be applied and evaluated.

5 Transmit-Receive Beamforming at 60 GHz

This chapter is dedicated to the evaluation of Analog BeamForming (ABF) solutions applied to the previously described 60 GHz channel model. The considered beamforming approach is based on analog beam-switching, where the best Tx-Rx beam-pattern pair is exhaustively searched for by maximizing the average output Signal-to-Noise Ratio (SNR). The performance parameters are the beamforming gain, the coherence bandwidth of the beamformed channel and the average spectral efficiency after beamforming. The impact of the URA size is evaluated both in LOS and NLOS scenarios through Monte Carlo simulations. An ABF technique alternative to beam-switching is then introduced in order to optimize the system performance. Finally, general considerations on analog beamforming for 60 GHz are drawn.

Section 5.1 provides an introduction to the topic of beamforming for 60 GHz radios, while the beam-switching beamforming approach is defined in Section 5.2. The performance evaluation is presented in Section 5.3, and the simulation strategy is reported in Section 5.3.1. The simulation results are then discussed in Sections 5.3.2, 5.3.3 and 5.3.4. Afterwards, Section 5.4 introduces an alternative analog beamforming approach and discusses its cost-performance characteristics. Finally, the conclusions on this investigation are reported in Section 5.5.

5.1 Introduction

Before introducing the ABF scheme, it should be pointed out that the well-known optimum beamforming solutions such as Minimum Mean-Square Error (MMSE), Minimum Variance Distortionless Response (MDVR) [54] and Dominant Eigenmode Transmission (DET) cannot be applied to the Tx-Rx ABF system design. Indeed, the 60 GHz systems exhibit a frequency-selective behavior due to the multipath channel and the broad transmission bandwidth[1]. As a result, optimum processing techniques require a frequency-selective design that can be implemented, for instance, by means of transversal filters on each antenna branch or FFT processing [34]. However, because of the constraint on analog and scalar (i.e. narrowband) beamformer weight-vectors, these schemes are not suitable to the analog architecture of Figure 3.7 [6].

As a consequence, ABF solutions for 60 GHz transceiver systems are bound to be sub-optimal, featuring a narrowband response and being applied to a broadband channel. Therefore, cost functions incorporating frequency-selectivity cannot be optimized, and only aggregate quantities can be considered. Nonetheless, due to the lower cost and complexity of ABF design over DBF (see Section 3.3.3), analog beamforming solutions are likely to be adopted for the 60 GHz [6], and therefore the evaluation of their performance is a necessary step in the system design.

[1]This statement will be confirmed subsequently by simulation results.

5.2 Beam-Switching

The analog beamforming scheme considered in this manuscript is based on the concept of beam-switching, also referred to as "exhaustive search". Reportedly utilized in other wireless communication systems such as WiMAX [55] and opportunistic beamforming, this technique is based on the concept of sectorial antennas. The Tx and Rx arrays feature a set of fixed beam-patterns, and the best joint Tx-Rx beam-pattern pair is selected so as to optimize a given cost function.

Figure 5.1 schematically illustrates the functioning of the scheme: the two transceivers are misaligned, thus the LOS does not coincide with the Main Response Axis (MRA) of the antenna arrays. Through the beam-switching technique, the blue antenna beam-patterns are selected so as to increase the system gain along the direction of the LOS. Similarly, when the direct path is obstructed, the phased array is steered towards the yellow sectors, exploiting the strongest reflection.

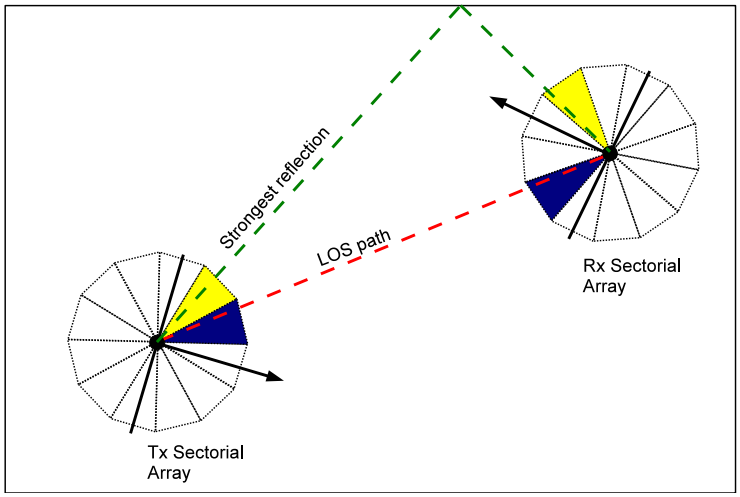

Figure 5.1: Schematic representation of transmit-receive beam-switching.

The cost function considered for the beam-switching is the SNR at the beamformer output, averaged over the whole transmission bandwidth. Therefore, the Tx-Rx beam-pattern pair that yields the maximum average SNR is selected among a pool of pre-defined beam-patterns. Recalling Equation (3.23), the SNR is expressed as follows:

$$\begin{aligned} SNR(f) &= \frac{\mathbf{c}^H\mathbf{H}(f)\mathbf{w}A(f)A^*(f)\mathbf{w}^H\mathbf{H}^H(f)\mathbf{c}}{\mathbf{c}^H\mathbf{N}(f)\mathbf{N}^H(f)\mathbf{c}} \\ &= \frac{\sigma_a^2}{\sigma_n^2}|\mathbf{c}^H\mathbf{H}(f)\mathbf{w}|^2 \end{aligned} \tag{5.1}$$

where spatially-white AWGN of variance σ_n^2, zero-mean i.i.d. data of variance σ_a^2 and power-normalized beam-vectors are assumed. The cost function to be maximized is

therefore given by the SNR averaged over the transmission bandwidth:

$$\Omega(\mathbf{c},\mathbf{w}) = \frac{\sigma_a^2}{\sigma_n^2 B}\int_B |\mathbf{c}^H\mathbf{H}(f)\mathbf{w}|^2 df = \frac{\sigma_a^2}{\sigma_n^2 B}\int_B |\tilde{H}_{(\mathbf{c},\mathbf{w})}(f)|^2 df \tag{5.2}$$

where $\tilde{H}_{(\mathbf{c},\mathbf{w})}(f)$ is termed *beamformed channel*. Hence, the beam-vectors are selected in the following manner:

$$\begin{aligned}(\hat{\mathbf{c}},\hat{\mathbf{w}}) &= \arg\max_{\mathbf{c},\mathbf{w}}\{\Omega(\mathbf{c},\mathbf{w})\} \\ &\equiv \arg\max_{\mathbf{c},\mathbf{w}}\left\{\int_B |\tilde{H}_{(\mathbf{c},\mathbf{w})}(f)|^2 df\right\}, \quad \mathbf{c}\in\mathcal{C},\mathbf{w}\in\mathcal{W}\end{aligned} \tag{5.3}$$

where $\mathcal{C}$ and $\mathcal{W}$ are termed *beam-vector codebooks*. From Equation (5.3) it is seen that maximizing the average SNR equals to maximizing the total multipath energy at the output of the receive array.

The beam-switching technique is implemented using a phased array with analog scalar (i.e. narrowband) weights, therefore phase-shifted versions of the same signal are launched/received by the antennas. Hence, no spatial multiplexing gain nor diversity gain can be achieved with this approach. It should also be noticed that by maximizing (5.2), the energy of the delayed paths is treated as useful energy to maximize the average signal energy at the output of the ABF system, as in [6]. Thus, since the multipath components are not regarded as additional noise, the Signal to Interference and Noise Ratio (SINR) is not considered here.

Considering a transmit array with T sectors and a receive antenna with R beam-patterns, the exhaustive search process is structured in T steps. In each step, the following operations take place (see Figure 5.2):

- **Forward transmission**: the Tx transmits using $\mathbf{w}_t$, the t-th weight vector of its codebook;
- **Receiver sweep**: the Rx receives using all of its beam-patterns $\mathbf{c}_r$, $r = 1,\ldots,R$. For each beam-pattern, the average SNR is estimated and the Rx weight vector corresponding to the greatest average SNR, denoted with $\mathbf{c}^{(t)}$, is selected:

$$\mathbf{c}^{(t)} = \arg\max_{\mathbf{c}_r}\{\Omega(\mathbf{c}_r,\mathbf{w}_t)\} \quad r = 1,\ldots,R \tag{5.4}$$

- **Feedback transmission**: the Rx transmits using $\mathbf{c}^{(t)}$ and communicates to the Tx the selected Rx beam-vector index $\mathbf{c}^{(t)}$ and the corresponding average SNR $\Omega(\mathbf{c}^{(t)},\mathbf{w}_t)$.
- **Weight selection**: after all the T steps are completed, the Tx-Rx beam-vector pair that corresponds to the greatest average SNR is selected.

$$(\hat{\mathbf{c}},\hat{\mathbf{w}}) = \arg\max_{\mathbf{c}^{(t)},\mathbf{w}_t}\left\{\Omega(\mathbf{c}^{(t)},\mathbf{w}_t)\right\}, \quad t = 1,\ldots,T \tag{5.5}$$

  The procedure exhaustively tries $T\cdot R$ beam-pattern pairs, as expressed in Equation (5.3)

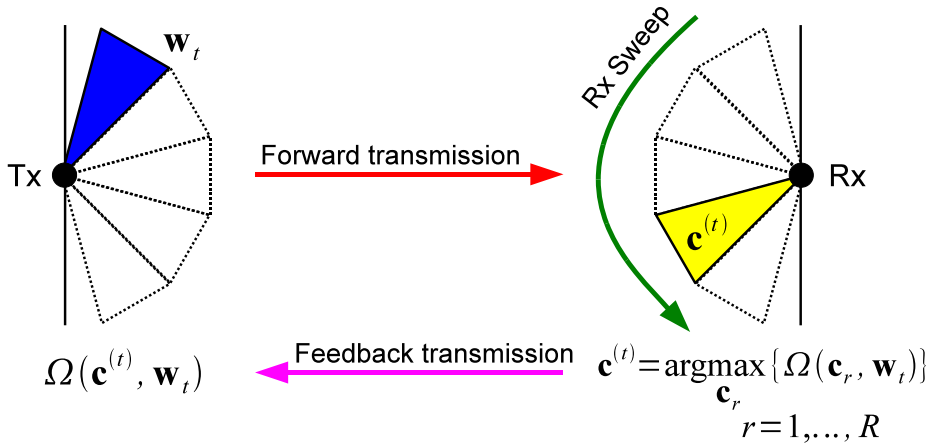

Figure 5.2: Representation of the t-th step of the exhaustive search process.

A block-scheme representation of the beam-switching beamforming is illustrated in Figure 5.3. It is important to notice that the channel estimation block is assumed ideal; therefore, perfect Channel State Information (CSI) is assumed available at each stage of the $T \cdot R$ beam-pattern trials. Besides, a feedback channel is assumed available so that the exhaustive search process can be properly synchronized between the two transceivers.

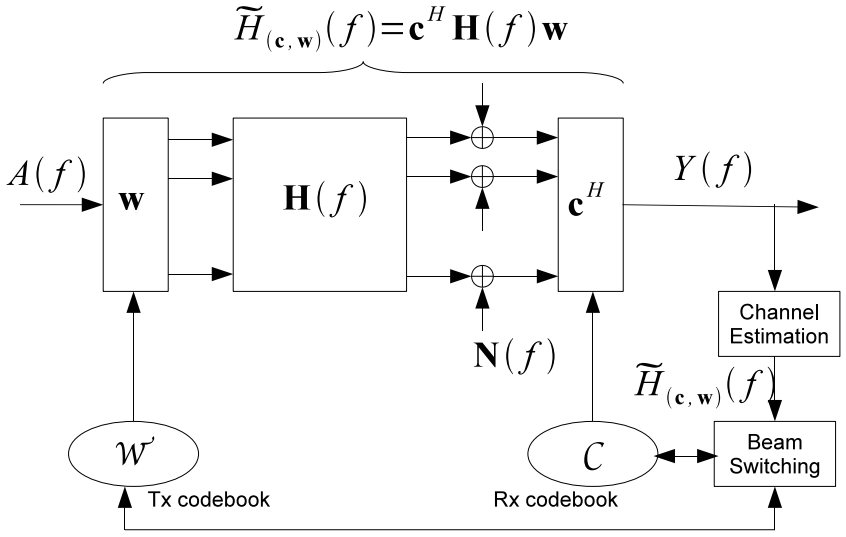

Figure 5.3: Beam-Switching beamforming block-scheme.

5.2.1 Beam-vector Codebook

The beam-vector codebook adopted in this thesis is based on the concept of orthogonal beam-patterns. In [34] it is reported that a NM-element standard array can produce NM orthogonal beams equally spaced in the direction cosine domain. The mathematical description on how to construct an orthogonal beam-pattern codebook is provided in Appendix B.

The central beam-vector of the codebook corresponds to the standard beam-pattern (see Equation (3.19)) pointing towards the array MRA. The remaining $NM - 1$ beams are simply shifted versions of the central beam-pattern in the direction cosine domain. Their corresponding beam-vectors are therefore obtained by applying a progressive phase shift to the antenna elements. The pointing direction of the nm-th beam-pattern occurs at $(u_x, u_y) = (2n/N, 2m/M)$ (see appendix B), where

$$n = \begin{cases} -\frac{N}{2} + 1, \ldots, \frac{N}{2} & N \text{ even} \\ -\frac{N-1}{2}, \ldots, \frac{N-1}{2} & N \text{ odd} \end{cases} \tag{5.6}$$

All other beams have nulls at that point, due to the orthogonality of the beam-vectors.

Figures 5.4 and 5.5 illustrate the beam-pattern codebook for a 3×3 URA in the direction cosine domain and in spherical coordinates. It can be noticed that while the pointing directions are equally-spaced in the direction cosine domain (Figure 5.4), their spacing increases as the look-direction in the (θ, ϕ)-space moves away from the MRA (Figure 5.5). Furthermore, from Figure 5.5 it can be inferred that the HPBW of the main lobe broadens for pointing directions far from the array MRA, meaning that the array performs a coarser spatial filtering.

It should be noticed that the beam-switching beamforming based on orthogonal codebooks is different from the approaches based on scanning the (θ, ϕ)-space with a fixed angular step size, as shown in Figure 5.5. In the latter approach the number of beams is given *a priori*, regardless of the number of array elements; on the contrary, when using orthogonal beam-patterns, the number of beams (and thus the size of the codebook) always equals the number of antennas.

One final consideration is that the codebook matrix of size $NM \times NM$ can be proved to have a Fourier structure. This results in an Hermitian matrix, hence reducing the memory space needed to store the beam-vectors into the transceiver apparatus.

The characteristics of the beam-patterns in the codebook play a role on the ABF beam-switching performance. In particular, the following parameters are relevant: the Half-Power Beam Width (HPBW), the Null-to-Null Beam Width (NNBW) and the sidelobe level. These values indicate the spatial resolution of the array as well as its capability to attenuate signal arriving to/departing from the region outside the main lobe.

The URAs considered in this thesis work are squared arrays of the following sizes: 4,

9, 16, 25 and 36 elements. The beam-pattern cuts on the horizontal/vertical[2] plane are illustrated in Figure 5.6 for the central beam-pattern, and the corresponding parameters are listed in Table 5.1.

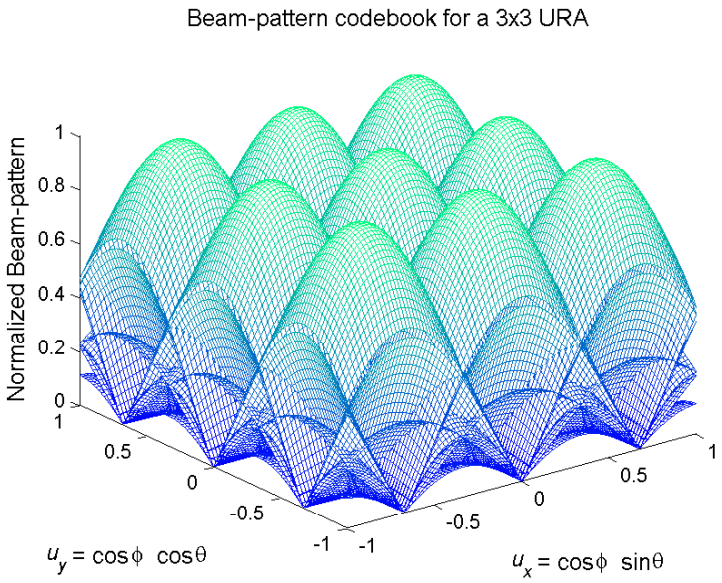

Figure 5.4: Beam-vector codebook of a 3x3 URA in the direction cosine domain.

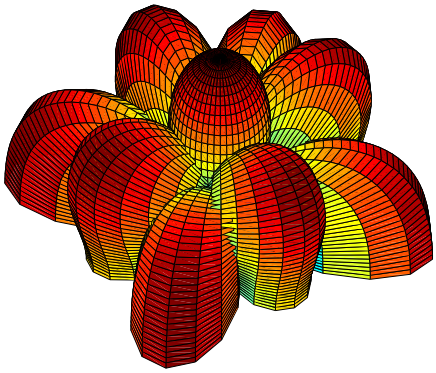

Figure 5.5: Beam-vector codebook of a 3x3 URA in spherical coordinates.

[2]The pattern cuts on the horizontal (i.e. $\phi = 0°$) and vertical (i.e. $\phi = 90°$ planes are identical for a squared array.

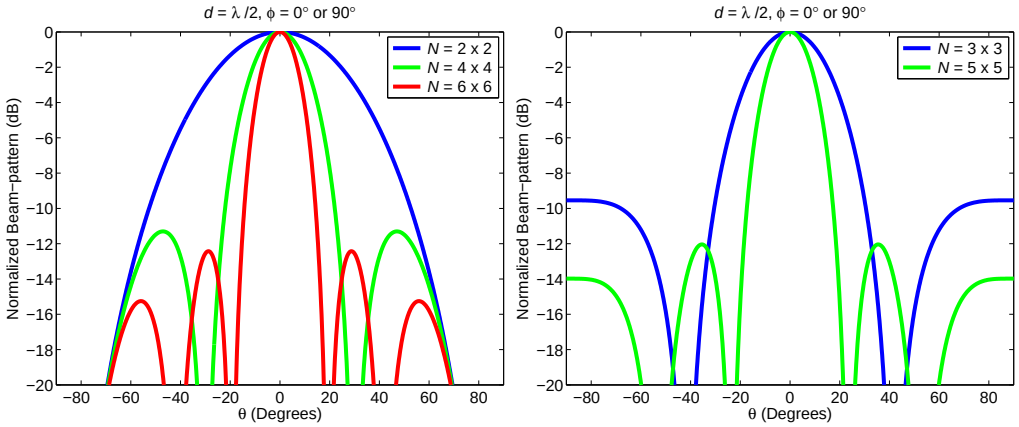

(a) Even number of elements. (b) Odd number of elements.

Figure 5.6: Beam-pattern cuts (horizontal/vertical planes) of the central beam-pattern for the considered URA structures.

Table 5.1: Beam-pattern characteristics for the considered URA structures.

URA size	HPBW (min/max)	NNBW	Sidelobe level
2×2	$60°/120°$	$180°$	No sidelobes
3×3	$36°/57°$	$83°$	-9.5 dB
4×4	$26°/80°$	$60°$	-11 dB
5×5	$20°/41°$	$47°$	-12 dB
6×6	$17°/62°$	$40°$	-12.5 dB

It should be noticed that the steered beam-patterns feature a broader main lobe, since the HPBW broadens for pointing directions far from the array MRA. The maximum values of HPBW are listed in Table 5.1 for the considered array structures. The odd-numbered arrays feature a smaller maximum HPBW in that their codebook does not include end-fire beam-patterns (i.e. the pointing direction lays on the plane of the array). The beam-pattern codebooks employed in this thesis are illustrated in details in Appendix B.

In [34] it is reported that the beam-patterns obtained with uniform weighting, such as in the codebooks considered here, feature the maximum achievable directivity (equal to N) and the narrowest HPBW. However, their sidelobe rate of decrease is reported to be slow compared to other non-uniform weighting schemes, which feature improved sidelobe behavior at the cost of a reduced directivity and a broader HPBW[3]. The beam-pattern design is therefore a trade-off between directivity, spatial resolution and sidelobe behavior; the choice made here is to maximize the directivity and minimize the HPBW, allowing for a sub-optimal sidelobe behavior.

[3]A description of the most common beam-pattern design techniques may be found in [34].

5.3 Performance Evaluation

The evaluation of the performance of the Tx-Rx phased-array ABF based on beam-switching with orthogonal codebooks is performed for LOS/NLOS scenarios using square URAs of different size and applied to the 60 GHz MIMO channel described in Section 4.2. The analysis is carried out through Monte Carlo simulations, investigating the impact on the system performance of the array size and of the nature of the channel (LOS/NLOS). The performance parameters considered in this thesis are the following:

- **Beamforming gain**, which is the increase in terms of average SNR introduced by the Tx-Rx ABF with respect to the average SNR of a system featuring transceivers with a single omnidirectional antenna (i.e. without beamforming);
- **Coherence bandwidth**, which qualitatively illustrates the impact of the Tx-Rx ABF on the frequency-selectivity of the beamformed channel;
- **Average Spectral Efficiency**, proportional to the capacity of the phased-array ABF system based on beam-switching and therefore to the achievable transmission rates. An upper-bound comparison with Dominant Eigenmode Transmission (DET) beamforming is performed. Differently from the beam-switching ABF, DET beamforming features broadband array processors and variable antenna gains (not a phased-array beamforming).

As it will be shown in the subsequent sections, the aforementioned parameters are straightforwardly extracted from the beamformed channel, i.e. the end-to-end channel between the input of the transmit array and the output of the receive beamformer, denoted with $\tilde{H}_{(\mathbf{c},\mathbf{w})}(f)$.

5.3.1 Simulation Procedure

The simulation procedure is schematically illustrated in Figure 5.7. The considered propagation environment is an empty room with size equal to the "Residential Room"[4] described by the IEEE 802.15.3c [14]. This scenario was selected since the SDCM described in Chapter 4 was shown to generate accurate results (see Section 4.2.2), and because the IEEE TG3c provides its specific channel parameters in [14].

Each realization of the beamformed channel is obtained in the following manner:

- **Tx-Rx position and orientation**. The position of the transceiver is determined randomly within the propagation environment: their cartesian coordinates are modeled as uniform RV windowed by the room size. In order to obtain realistic scenarios, the MRA of the transceivers is allowed to vary randomly on the horizontal and vertical planes, following a zero-mean Gaussian PDF centered on the perfect pointing direction and with RMS equal to 30°.

[4]The room size is $(6.85 \times 3.57 \times 2.47)$ m (see Figure A1).

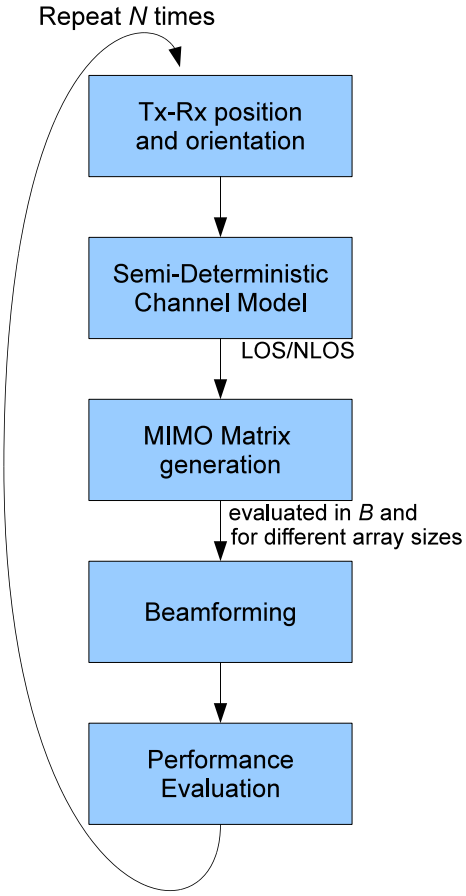

Figure 5.7: Simulation strategy to evaluate the ABF system performance.

- **Semi-deterministic channel model**. By performing ray-tracing in the given propagation environment and adding the proper statistical features[5], the SDCM generates all the clusters/rays and characterizes them in terms of complex-valued amplitude, ToA, DoD and DoA. NLOS channel realizations are simply obtained by removing the direct path.

- **Broadband MIMO matrix generation**. From the output of the SDCM, the broadband MIMO matrix is constructed as described in Section 4.3:

$$\mathbf{H}(f) = \mathbf{V}(\theta_{rx}, \phi_{rx})\mathbf{B}(f)\mathbf{V}^H(\Theta_{tx}, \Phi_{tx}) \tag{5.7}$$

  The MIMO matrix is evaluated on a band of 2 GHz[6] centered about 60 GHz, at frequency steps equal to $\Delta f = 10$ MHz. The following squared URA sizes are considered in the simulation: 4, 9, 16, 25 and 36 elements. Moreover, the transmit and receive arrays are assumed to be of equal size.

[5]That is, modeling the reflection coefficients and generating the clusters. See Section 4.2.

[6]In [23] it is reported that the maximum continuous bandwidth allocated for the 60 GHz is 2.16 GHz.

- **Beamforming**. In this step, ABF phased-array beam-switching is applied to the 60 GHz MIMO channel. The joint Tx-Rx beam-pattern is selected following the procedure of Section 5.2.
- **Performance Evaluation**. The beamformed channel $\tilde{H}_{(\mathbf{c},\mathbf{w})}(f) = \mathbf{c}^H \mathbf{H}(f)\mathbf{w}$ is utilized to evaluate the improvement of the system performance introduced by the ABF with respect to the single-input single-output (SISO) channel, that is without beamforming.

Finally, the results are averaged over a total of $N = 1000$ Monte Carlo simulations. All the tools necessary for the simulation have been developed in Matlab.

The simulation parameters are summarized in Table 5.2.

Table 5.2: Simulation parameters

Parameter	*Value/Description*
Room size	$(6.85 \times 3.57 \times 2.47)$ m
TRx position	Uniform RV
TRx orientation	zero-mean Gaussian RV centered about the perfect-pointing direction, RMS 30°
SDCM Parameters	IEEE 802.15.3c parameters for the "Residential Room" environment; log-normal reflection coefficients (see Table 4.3)
Channel Type	LOS/NLOS
Bandwidth	2 GHz $(59 - 61$ GHz)
Δf	10 MHz
URA size	4, 9, 16, 25, 36 elements, equal at Tx-Rx sides
N	1000 Monte-Carlo simulations

It should be noticed that, within the entire system model framework of Figure 3.8, the present evaluation actually concentrates on the channel part alone, showing how some characteristics of the channel after ABF improve with respect to the channel prior to beamforming. This is why the performance evaluation is transparent to the data and aspects such as digital modulation, coding, equalization and carrier recovery: the performance evaluation is carried out without setting up a communication chain.

5.3.2 Beamforming Gain

The beamforming gain is defined as the improvement in terms of average SNR introduced by the Tx-Rx ABF system with respect to the SISO system, where the transceivers feature a single omnidirectional antenna with gain equal to 0 dBi[7]. Mathematically, the beamforming gain is expressed as follows:

$$\begin{aligned} G_{BF} &\triangleq \frac{\overline{SNR}_{BF}}{\overline{SNR}_{SISO}} \\ &= \frac{\frac{\sigma_a^2}{\sigma_n^2 B}\int |\mathbf{c}^H \mathbf{H}(f)\mathbf{w}|^2 df}{\frac{\sigma_a^2}{\sigma_n^2 B}\int |H(f)|^2 df} \\ &= \frac{\int |\mathbf{c}^H \mathbf{H}(f)\mathbf{w}|^2 df}{\int |H(f)|^2 df} \end{aligned} \tag{5.8}$$

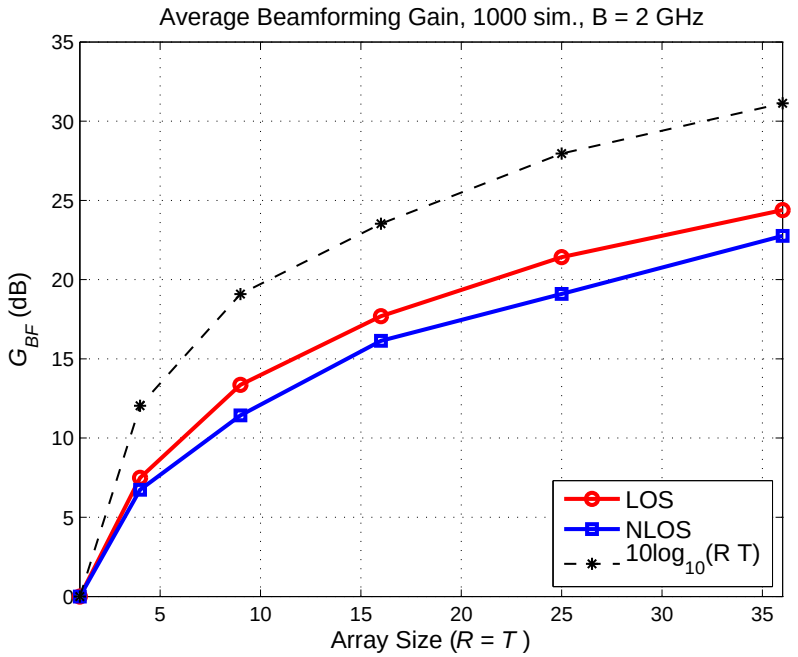

Figure 5.8: Beam-switching beamforming gain vs. array size, LOS/NLOS scenarios.

The simulation results are illustrated in Figure 5.8 as a function of the Tx-Rx array size (equal for the transceivers), both in LOS/NLOS scenarios. From the simulation, it is clearly seen that the beamforming gain improves proportionally to the number of antenna elements $R = T$. It is interesting to notice that the trend is very similar for the LOS and NLOS cases. This fact indicates that the behavior of the beam-switching ABF is similar in both scenarios: it locks on the direction of the direct

[7]The antenna elements of the beamforming arrays are also assumed to be omnidirectional radiators of gain 0 dBi.

path in the LOS case, and it directs the Tx-Rx beam-patterns towards the strongest reflection in the NLOS case. In turns, this means that the 60 GHz channel, on the average, exhibits a dominant ray both in LOS and NLOS scenarios.

In the considered scenario, the gap between the LOS and NLOS curves ranges from 0.7 to 2.5 dB, depending on the size of the Tx-Rx arrays. This behavior may be explained by the fact that, in NLOS environments, the ABF does not lock on a single ray but on a cluster of rays of comparable power. Hence, the scattered components combine constructively and distructively across the spectrum, leading to an increased fading. Moreover, in some NLOS realizations the ABF could spatially filter out clusters that feature a comparable power to the dominant one, thus rejecting useful energy.

Furthermore, NLOS channel realizations feature a lower average channel gain due to the lack of the LOS path[8]. From the simulations, it is seen that the lack of the LOS ray results in an average power penalty of approximately 5 dB. Henceforth, the expected average SNR penalty after Tx-Rx ABF and in the absence of the direct path ranges from 5.7 to 7.5 dB in the considered environment.

The observed average beamforming gain is compared to the theoretical array gain, represented in Figure 5.8 with a dashed line, which is the gain introduced by the Tx-Rx arrays in conditions of perfect pointing and only one ray (flat-fading channel). For a $T \times R$ system, the theoretical array gain is given by $10\log_{10}(RT)$ [34]. From the simulation results it is seen that there is a consistent gap between the ABF beam-switching and the theoretical array gain, ranging from approximately 4.5 to 6.5 dB.

Finally, from Figure 5.8 it can be seen that the poor link budget problems which the 60 GHz technology has to tackle, both in LOS and NLOS scenarios, can be effectively mitigated by introducing the Tx-Rx ABF based on beam-switching. This concept is elaborated through an example in the following case-study.

Beamforming gain at 60 GHz: case study

Let us consider a typical application scenario for 60 GHz indoor wireless communications and let us derive the link budget with and without beam-switching ABF. A transmit power of $P_{TX} = 20$ dBm is assumed with a transmission bandwidth equal to 2 GHz. The signal power in dB at the receiver output has the following expression:

$$P_{RX} = P_{TX} + G_h - PL(d) + G_{BF} \tag{5.9}$$

where PL is the path loss at a distance d, G_h is the average gain introduced by the SISO channel and G_{BF} is the beamforming gain. The path loss is readily determined through the Friis formula [26]:

$$PL(d) = 20\log_{10}\left(\frac{\lambda_0}{4\pi d}\right) \tag{5.10}$$

[8]Recall Section 4.1: the LOS is conventionally assigned a value of 1, and the subsequent rays follow the channel power delay profile.

where a path-loss exponent of $n = 2$ was assumed[9]. At $f_0 = 60$ GHz and at a distance of $d = 10$ meters, the path loss calculated by (5.10) equals approximately -88 dB. The gain introduced by the SISO channel is determined by running the simulation with only one antenna per transceiver, and it is shown to be equal to 2 dB for the LOS case and about -3 dB in the NLOS case[10]. Therefore, there is an average penalty of 5 dB on the average SNR when the LOS path is not present. The average received signal power is calculated by (5.9) and equals -66 and -71 dBm for the LOS and NLOS cases, respectively.
Assuming a temperature of 290 K, the noise spectral density is given by $kT = -114$ dBm/MHz, which results in $P_N = -81$ dBm considering the large transmission bandwidth. The receiver noise figure is assumed equal to 5 dB, factoring in for a total noise power of -76 dBm.
With the aforementioned values, the average SNR at the receiver output without beamforming equals 10 dB and 5 dB for the LOS and NLOS cases, respectively. From Figure 5.8 it can be inferred that, assuming a target average SNR of 20 dB, 3×3 ABF arrays would be needed in the LOS case and 4×4 URAs would be necessary for the NLOS case.

In Section 3.2.1 it was claimed that the narrowband assumption could be regarded as valid for the considered transmission bandwidth. Figure 3.5 illustrated that the beam-pattern of the phased-array can be considered practically constant across the spectrum, therefore allowing for the adoption of the narrowband Steering Vector Model (SVM). In order to provide further evidence of the validity of this approximation, the average beamforming gain was simulated considering both the narrowband SVM and the broadband SVM. The results are illustrated in Figure 5.9. From Figure 5.9 it is clearly seen that the results are almost identical. The narrowband approximation for the steering vectors, therefore, does not impact on the final average simulation results.

5.3.3 Coherence Bandwidth

The coherence bandwidth B_C may be defined as the range of frequencies over which the channel can be considered "flat", that is the frequency interval over which two frequencies are likely to experience comparable or correlated amplitude fading. This parameter is very important in the design of radio systems since it gives an indication on the amount of Inter-Symbol Interference (ISI) introduced by the channel, i.e. its time dispersion [29]. If the transmit bandwidth is greatly smaller than the coherence bandwidth, then the received signal can be retrieved undistorted with very simple equalization (ideally, without equalization). In the opposite case, however, the transmitted signal will experience severe multipath fading, and the complexity

[9] In [14], the path loss exponent is reported to range from 1.4 to 2 in the LOS case and from 2 to 4 in the NLOS case.

[10] These values derive from the choice of assigning power equal to 1 to the LOS component and smaller values for the secondary rays, spread about the exponentially-decaying power delay profile. See chapter 4 for further details.

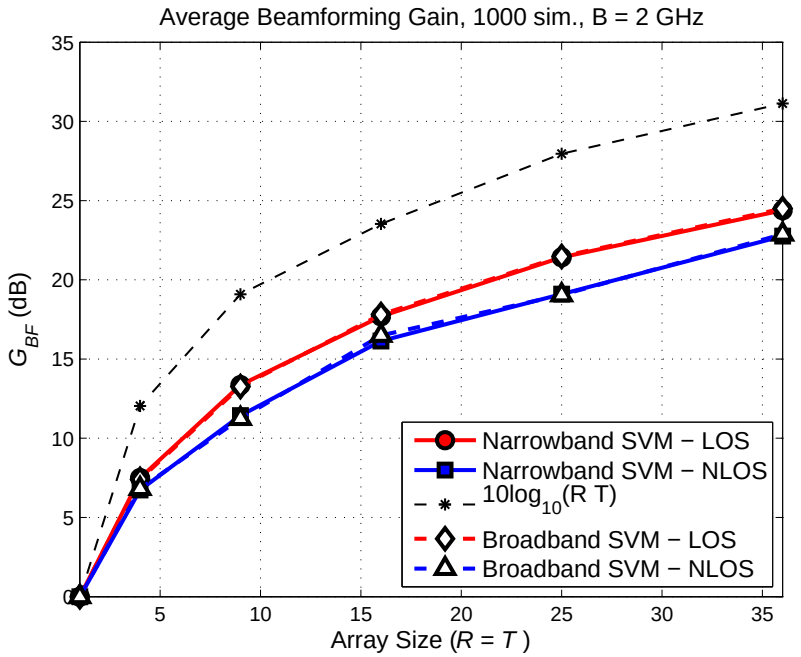

Figure 5.9: Comparison between the average beamforming gain obtained with the narrowband Steering Vector Model (SVM) and the broadband SVM.

of the system will increase to counter the distortion introduced by the broadband channel.

As seen from (5.3), the Tx-Rx ABF is not designed to remove the ISI, and all the multipath energy is treated as useful energy. However, due to the spatial filtering properties of the arrays, some multipath components are inevitably attenuated by the Tx-Rx ABF. In this context, the coherence bandwidth can be considered a useful indicator to illustrate how the beam-switching ABF impacts on the frequency selectivity of the end-to-end channel.

The coherence bandwidth is calculated via Root-Mean-Square (RMS) delay spread, denoted with τ_{RMS}, which is the square-root of the second moment of the power delay profile:

$$\tau_{RMS} = \sqrt{\overline{\tau^2} - \overline{\tau}^2} \tag{5.11}$$

where

$$\overline{\tau} = \frac{\sum_k |\alpha_k|^2 \tau_k}{\sum_k |\alpha_k|^2} \tag{5.12}$$

where α_k and τ_k are the complex-valued amplitude and the ToA of the k-th ray, respectively; k indexes the rays of the beamformed channel, that is the multipath components of the SISO channel weighted by the Tx-Rx beamformers, depending on their DoD/DoA (see Equation (4.14)). At this point, the coherence bandwidth is obtained through $B_C \approx 1/\tau_{RMS}$ [29].

The simulation results are presented in Figure 5.10. First of all, it is seen clearly that the 60 GHz channel is inherently frequency-selective. In fact, for single-element antennas at both communication sides ($R = T = 1$), it can be seen that the coherence bandwidth of the SISO channel, on average, is respectively about 200 - 250 MHz for the LOS and NLOS cases. Since the transmission bandwidth is in the order of 10 times broader, the 60 GHz channel should be clearly considered as frequency-selective.

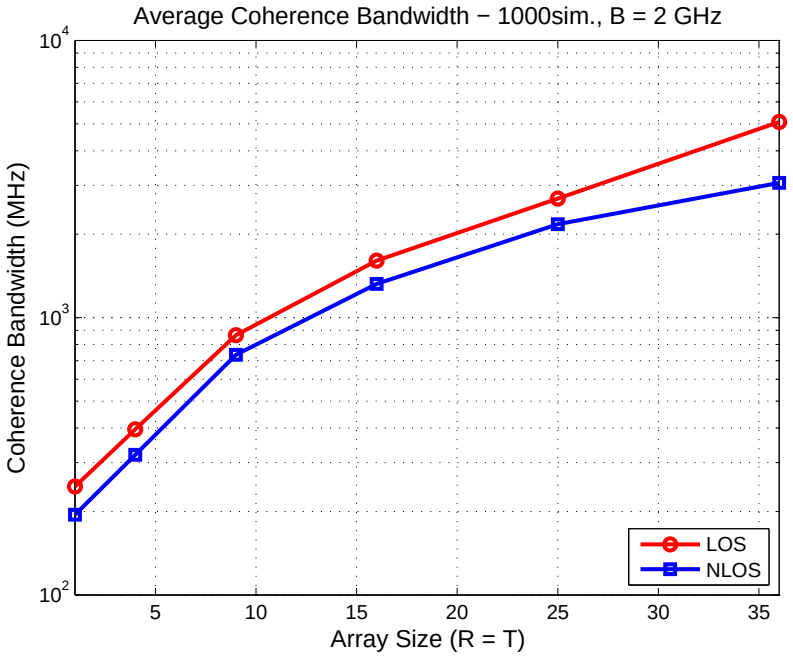

Figure 5.10: Beam-switching coherence bandwidth vs. array size, LOS/NLOS scenarios.

From Figure 5.10 it is also seen that, on the average, the frequency-selectivity of the beamformed channel is mitigated by the introduction of the Tx-Rx ABF based on beam-switching. The effects are more evident for larger arrays, and the improvement occurs both in LOS and NLOS environments with a quite similar trend.

Figure 5.11 illustrates the results in terms of RMS delay spread and percentage improvement. Once again, it is seen that the trend for the LOS and NLOS cases is very similar, as confirmed by the improvement in percentage. It is interesting to notice that the impact is greater for small arrays, up to 9 elements, while the additional improvement in percentage introduced by larger arrays is rather small.

Finally, Figure 5.12 illustrates the empirical Cumulative Distribution Function (CDF) of the experimental values. With this representation, it is possible to investigate the probability that the coherence bandwidth of the beamformed channel falls below a given probability threshold (commonly referred to as *outage probability*). Some empirical values are listed in Table 5.3. A few conclusions can be drawn. First, it can be seen that for low thresholds (that is, when severely frequency-selective

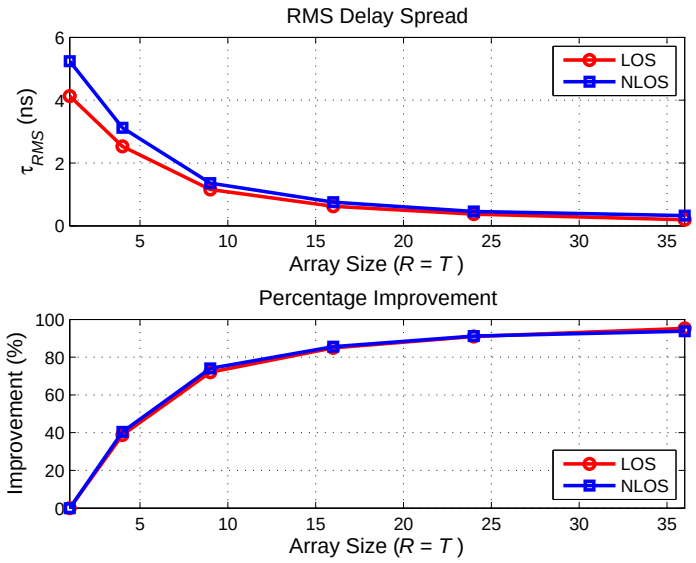

Figure 5.11: Beam-switching RMS delay spread vs array size, LOS/NLOS scenarios.

channel realizations occur) and for both scenarios, the impact of Tx-Rx ABF is rather small, for all URA sizes. On the other hand, for higher thresholds the impact of the array size and of the channel nature is greatly enhanced, as inferable from Table 5.3. The greatest levels of coherence bandwidth are obtained when one of the following conditions occur: either the channel realization features a modest multipath (the most delayed components have a very low power) or the multipath components are well separated in the angular domain, and thus are filtered out by the Tx-Rx beamformers.

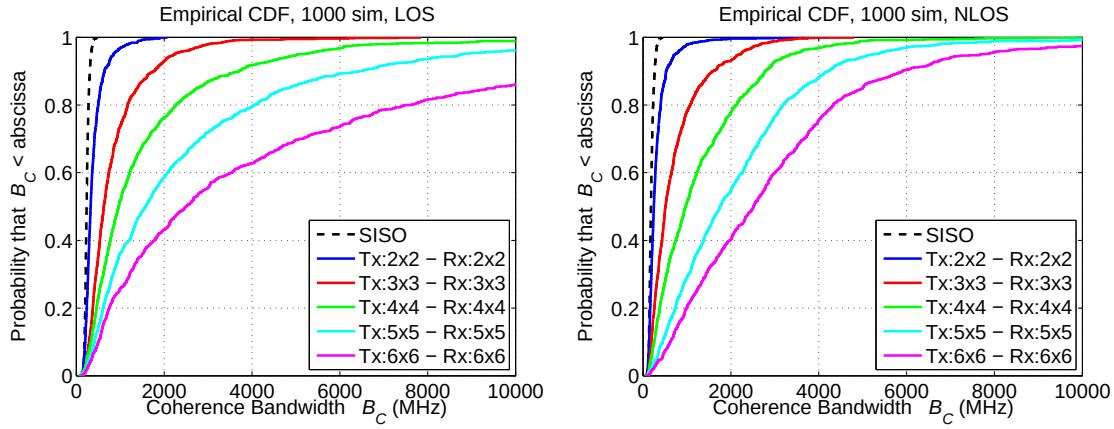

(a) LOS case (b) NLOS case

Figure 5.12: Coherence bandwidth empirical CDF vs array size. a) LOS case; b) NLOS case.

The ultimate conclusion of the investigation on the coherence bandwidth is that the

Table 5.3: Coherence bandwidth in MHz for different outage probabilities.

	LOS			*NLOS*		
	10%	50%	90%	10%	50%	90%
SISO	185	235	306	133	181	264
Tx:2 × 2 - Rx:2 × 2	204	326	644	139	246	526
Tx:3 × 3 - Rx:3 × 3	289	625	1778	189	513	1580
Tx:4 × 4 - Rx:4 × 4	335	966	3700	253	966	2770
Tx:5 × 5 - Rx:5 × 5	414	1582	6408	451	1756	4200
Tx:6 × 6 - Rx:6 × 6	500	2495	12620	619	2517	5900

introduction of the Tx-Rx ABF based on beam-switching mitigates the multipath components of the 60 GHz channel thanks to the spatial filtering performed by the beamformers. On average, this results in a reduced frequency-selectivity of the beamformed channel with respect to the channel without beamforming. Better average results are witnessed for large arrays and the LOS propagation scenario. Nonetheless, the Tx-Rx ABF is not designed to remove the ISI. As a result, the reduction of fading depends on the angles of arrival/departure of the multipath components, hence different frequencies may experience different delays, and the transmission bandwidth may be larger than the coherence bandwidth. Moreover, depending on each single channel realization, the impact of the array size and of the channel type can be high or low, as shown in Figure 5.12. The analysis indicates that the coherence bandwidth behavior is highly dependent on the specific channel realization, therefore proper solutions to tackle the ISI problem must be included in the 60 GHz system design (e.g. equalizer, OFDM, FFT processing).

5.3.4 Average Spectral Efficiency

The spectral efficiency of a communication system can be defined as the information rate that can be allocated in a given bandwidth [29]. The mathematical expression of the average spectral efficiency of the channel after Tx-Rx ABF is the following:

$$\overline{C}_{BF} = \frac{1}{B}\int_B \log_2\left(1+\frac{\sigma_a^2}{\sigma_n^2}|\tilde{H}_{(\mathbf{c},\mathbf{w})}(f)|^2\right)df, \quad (bit/s/Hz) \tag{5.13}$$

where σ_a^2/σ_n^2 is the SNR at the input of the receiver ad B is the transmission bandwidth. The average spectral efficiency is then averaged over $N = 1000$ Monte Carlo simulations.

The performance achieved by the Tx-Rx ABF over the 60 GHz MIMO channel is then compared to that of the following optimal beamforming scheme over the same channel:

Dominant Eigenmode Transmission (DET) beamforming. SNR maximization yields the optimal beamforming solution [9], referred to as Dominant Eigenmode

Transmission (DET). With this scheme, transmission occurs only along the eigenmode corresponding to the largest eigenvalue of $\mathbf{H}(f)\mathbf{H}^H(f)$, denoted as $\lambda_{max}(f)$. The DET spectral efficiency is given by [56]:

$$\overline{C}_{DET} = \frac{1}{B}\int_B \log_2\left(1 + \frac{\sigma_a^2}{\sigma_n^2}\lambda_{max}(f)\right) df, \quad (bit/s/Hz) \tag{5.14}$$

With this scheme, the MIMO subchannel with the greatest gain is exploited for transmission and reception. The number of parallel subchannels provided by the MIMO channel depends on the its spatial correlation and thus on the matrix spatial rank. Maximum system capacity is obtained by exploiting all parallel subchannels with independent signals and optimally loading the transmission power across the corresponding eigenmodes (water-filling [9]). In this manner, spatial multiplexing gain is achieved. However, since DET beamforming does not feature multiple signals (it is not a MIMO scheme: the end-to-end channel is rank-one), only one eigenmode is used for communication and no spatial multiplexing gain can be obtained. In the presence of a frequency-selective channel, the transmit power is equally loaded across the spectrum and allocated along $\lambda_{max}(f)$. The optimal Tx-Rx beamforming vectors are given by the left and right eigenvectors corresponding to the principal singular value of the MIMO channel matrix [56].

In [57] it is reported that DET beamforming, besides maximizing the SNR and thus attaining the optimum array gain, provides full spatial diversity gain. Indeed, the DET receive beamformer can be proved to be a Maximum Ratio Combiner (MRC) in that it optimally weights the signal copies received at each antenna branch so as to combat fading and maximize the system performance. The amount of spatial diversity that can be exploited depends on the spatial correlation of the channel: it decreases if the signal copies are highly correlated and increases in the opposite case[11] [57, 58]. Differently from DET beamforming, the considered ABF scheme cannot provide gain along the antenna branches but only operate on their phases: the signal combining is therefore not optimal and full spatial diversity cannot be achieved. Furthermore, since the channel is frequency-selective, optimum beamforming schemes require optimal weight computation across the entire transmission spectrum. Therefore, DET beamforming provides optimum array gain at each subcarrier while the beam-switching ABF, being a narrowband phased-array scheme, uses the same Tx-Rx weight vectors on all frequency tones.

It should be noticed that DET beamforming requires a digital and frequency-selective implementation, hence it cannot be considered a feasible Tx-Rx ABF solution within the scope of this thesis. The DET scheme is included here in order to provide an upper-bound comparison with the performance of the Tx-Rx analog beamforming based on beam-switching.

Figures 5.13 throughout 5.17 present the simulation results as a function of the input SNR for the considered beamforming schemes and for the SISO channel.

From the simulations it is clearly seen that the Tx-Rx beam-switching improves the

[11] Antenna spacing plays a fundamental role to achieve spatial diversity.

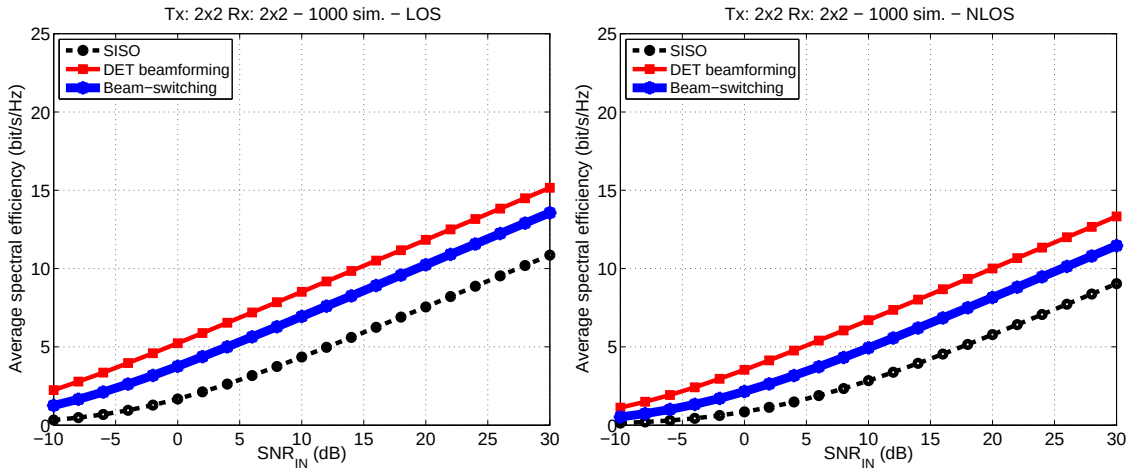

(a) LOS case (b) NLOS case

Figure 5.13: Average spectral efficiency for Tx:2 × 2 - Rx:2 × 2.

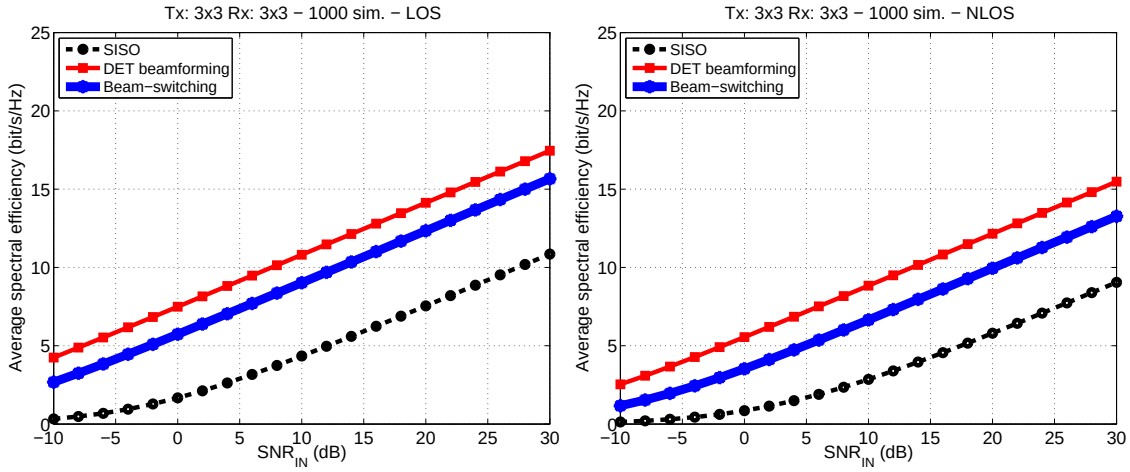

(a) LOS case (b) NLOS case

Figure 5.14: Average spectral efficiency for Tx:3 × 3 - Rx:3 × 3.

system performance with respect to the SISO channel. The improvement is more evident for large arrays, ranging from about 2.5 to 8.5 bit/s/Hz (for the 4×4 and 36×36 configurations, respectively) both for the LOS and NLOS cases. Moreover, it is seen that the ABF curve is basically a shifted version of the SISO curve, indicating that the improvement introduced by the ABF is due to the beamforming gain, which increases the output SNR. This is confirmed by comparing the spectral efficiency curves with the beamforming gain results of Figure 5.8. The NLOS case achieves a lower spectral efficiency due to the lack of the direct path, and once again the trend is seen to be similar to that of the LOS case. Figures 5.13 throughout 5.17 confirm that the ABF for the NLOS case implies a SNR penalty ranging from 5 to 7.5 dB with respect to the LOS case.

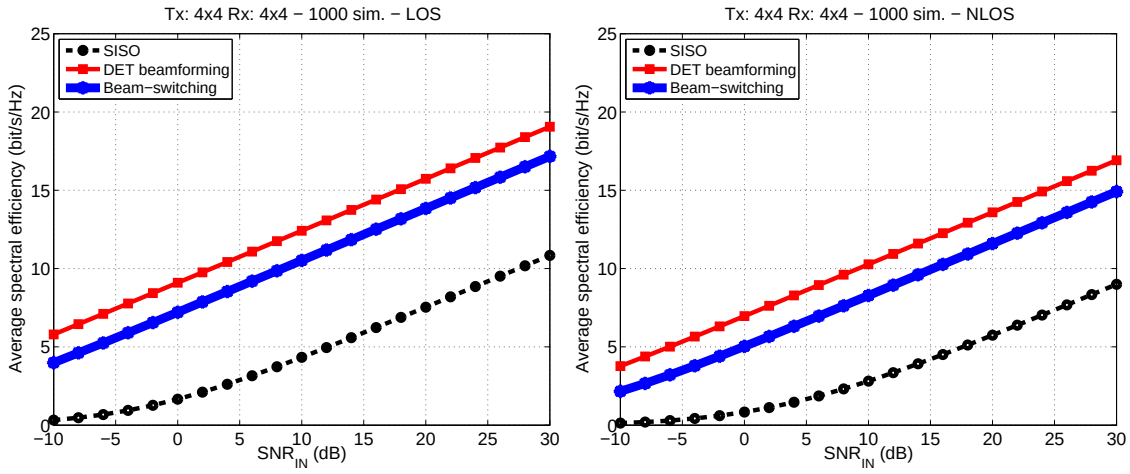

(a) LOS case (b) NLOS case

Figure 5.15: Average spectral efficiency for Tx:4 × 4 - Rx:4 × 4.

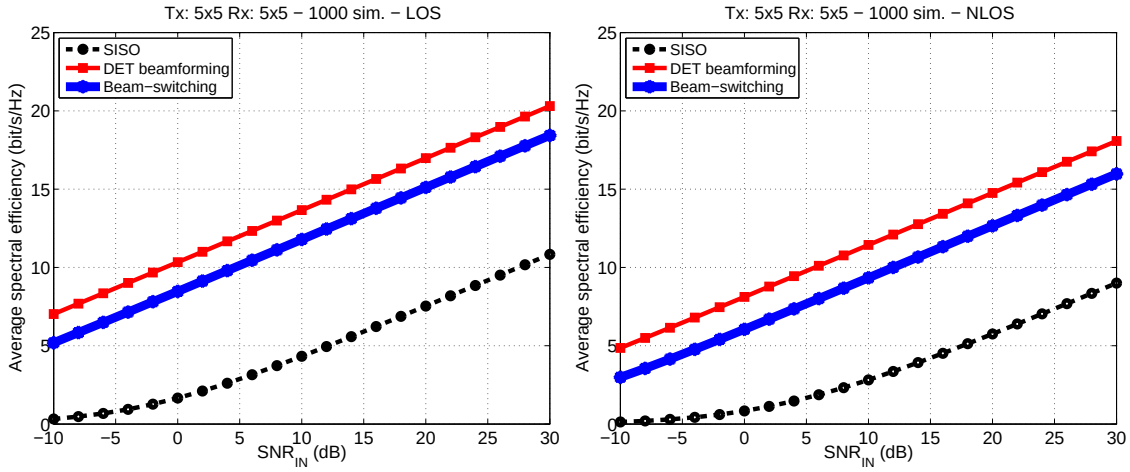

(a) LOS case (b) NLOS case

Figure 5.16: Average spectral efficiency for Tx:5 × 5 - Rx:5 × 5.

Furthermore, it is interesting to notice that the performance of the Tx-Rx ABF based on beam-switching is not distant from that of the optimal DET beamforming, for all SNR regimes. The trend is exactly the same for both schemes, indicating that the DET approach provides an increased beamforming gain, thus improving the output SNR. The SNR penalty for choosing the Tx-Rx ABF based on beam-switching over the DET beamforming is seen to be about 6 dB in all simulation scenarios.

Figure 5.18 presents the simulated values of average spectral efficiency vs. the URA size for $SNR_{IN} = 10$ dB for the Tx-Rx ABF scheme and the DET beamforming. Notice that the behavior is equal at all SNR regimes since the performance curves are parallel, as represented in Figures 5.13- 5.17. As expected, large arrays yield better performance, and it is interesting to notice that the gap between the optimum

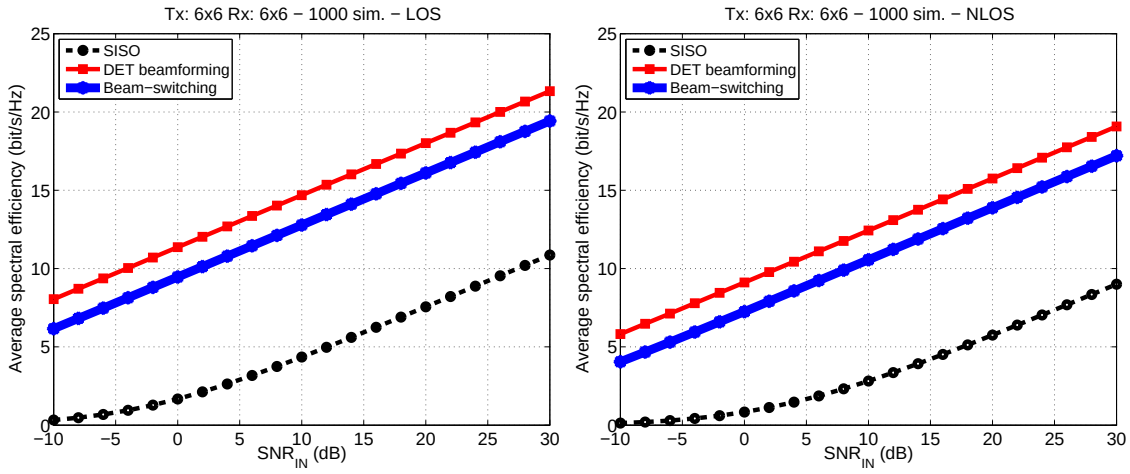

(a) LOS case (b) NLOS case

Figure 5.17: Average spectral efficiency for Tx:6 × 6 - Rx:6 × 6.

beamforming and the beam-switching is almost constant for all URA sizes and channel types, ranging from 1.6 to 1.8 bit/s/Hz[12]. This behavior suggests that the main difference between the two approaches resides in the beamforming gain, which is increased for the DET case thanks to an optimal power allocation across the spectrum.

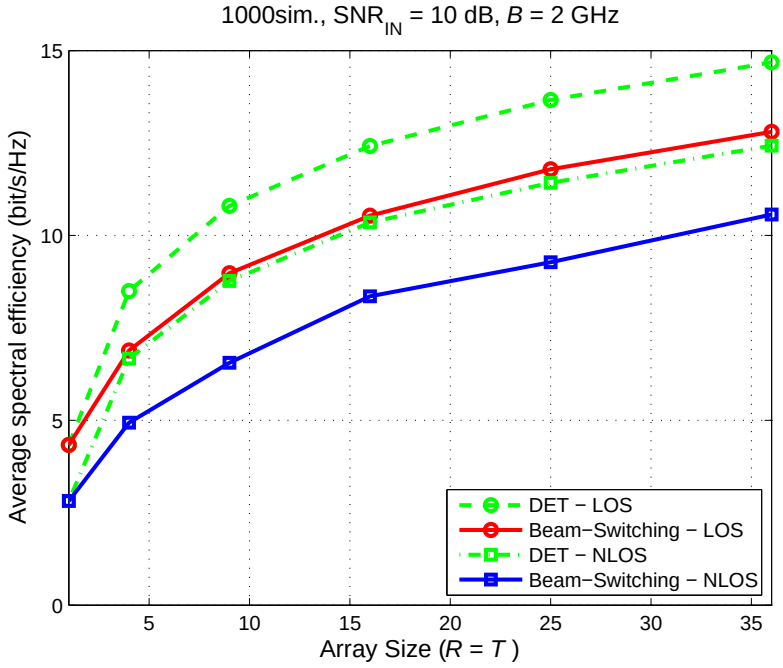

Figure 5.18: Average spectral efficiency vs. array size, $SNR_{IN} = 10$ dB.

[12]This gap should not be underestimated, considering the broad transmission bandwidth.

The comparison between the Tx-Rx ABF based on beam-switching and the digital multi-antenna schemes provides significant insight on beamforming over the 60 GHz channel. It is seen that the difference between the optimal DET beamforming and the ABF approach mainly consists in a SNR penalty of 6 dB, which in turns corresponds to average spectral efficiency levels about 1.8 bit/s/Hz lower. NLOS scenarios imply an additional power penalty of 5 - 7.5 dB on the average, observed both for the ABF case and the DET beamforming. Nonetheless, in the evaluation of the ABF technique, the algorithm complexity should be accounted for. The beam-switching is implemented in analog architecture, with scalar complex-valued weights that must be selected among a pre-defined beam-vector codebook. On the other hand, the DET beamforming features a digital architecture, which is less efficient in terms of power consumption and computational complexity [6]. Moreover, the beam-vectors are frequency-selective, and must be computed by means of SVD across the entire spectrum, making DET beamforming hardly suitable to low-cost 60 GHz radios [6].

Despite featuring simple analog design and reduced computational complexity, the beam-switching ABF has two main limitations. First, the duration of the exhaustive search process may lead to significant time-delay (for large arrays) and therefore outdated feedback. Secondly, the fact of using pre-defined fixed beams makes the beam-switching ABF poorly flexible. An alternative ABF approach is sought for in the subsequent section.

5.4 Alternative Analog Beamforming Approach

In this section, a ABF solution alternative to the ABF scheme based on beam-switching is investigated. The beam-switching technique discussed above exhibited a 6 dB SNR penalty with respect to the optimal DET beamforming, both in LOS/NLOS cases and for all URA sizes. This gap could be filled by overcoming the following limitations:

- **Procedure duration**. The number of steps in the exhaustive search process is $T \cdot R$. For the considered URA sizes, this translates into 16, 81, 256, 625 and 1296 steps during which the channel is assumed time invariant. For large arrays, the procedure adds significant time-delay and may lead to outdated feedback;
- **Quantized spatial resolution**. The beam-vector codebook of a R-element URA features R pre-defined pointing directions spanning the whole 3-D space. The pointing directions are fixed and cannot be refined to adapt to a specific channel realization (poor flexibility).

Improved ABF solutions should therefore feature the calculation of the Tx-Rx beam-vectors in order to overcome the fixed steering directions and the duration of the exhaustive search process, being at the same time suitable to the analog design with

scalar weights. In the following, the derivation of a beamforming scheme maximizing the average SNR at the receiver output is outlined.

The average SNR at the receiver output can be expressed in the following manner:

$$\begin{aligned}\Omega(\mathbf{c},\mathbf{w}) &= \frac{\sigma_a^2}{\sigma_n^2 B}\int_B |\mathbf{c}^H\mathbf{H}(f)\mathbf{w}|^2 df \\ &= \frac{\sigma_a^2}{\sigma_n^2 B}\mathbf{c}^H\left(\int_B \mathbf{H}(f)\mathbf{w}\mathbf{w}^H\mathbf{H}^H(f)df\right)\mathbf{c} \\ &= \frac{\sigma_a^2}{\sigma_n^2 B}\mathbf{c}^H\mathbf{P}\mathbf{c} \end{aligned} \tag{5.15}$$

where $\mathbf{P}$ is a positive-definite aggregate matrix containing the total multipath energy across the transmission bandwidth. The maximization of $\Omega(\mathbf{c},\mathbf{w})$ with respect to $\mathbf{c}$ is readily obtained [29]:

$$\begin{aligned}\tilde{\mathbf{c}} &= \arg\max_{\mathbf{c}}\left\{\mathbf{c}^H\mathbf{P}\mathbf{c}\right\} \\ &= \max\mathrm{eig}\left\{\mathbf{P}\right\}\end{aligned} \tag{5.16}$$

where the operator $\max\mathrm{eig}(\cdot)$ identifies the principal eigenvector of a given square matrix. Similarly, considering a feedback transmission (the transceivers swap their role), the average SNR at the system output is given by:

$$\begin{aligned}\Omega(\mathbf{c},\mathbf{w}) &= \frac{\sigma_a^2}{\sigma_n^2 B}\int_B |\mathbf{w}^H\mathbf{H}^H(f)\mathbf{c}|^2 df \\ &= \frac{\sigma_a^2}{\sigma_n^2 B}\mathbf{w}^H\left(\int_B \mathbf{H}^H(f)\mathbf{c}\mathbf{c}^H\mathbf{H}(f)df\right)\mathbf{w} \\ &= \frac{\sigma_a^2}{\sigma_n^2 B}\mathbf{w}^H\mathbf{Q}\mathbf{w} \end{aligned} \tag{5.17}$$

The optimal beam-vector $\tilde{\mathbf{w}}$ is therefore found as follows:

$$\begin{aligned}\tilde{\mathbf{w}} &= \arg\max_{\mathbf{w}}\left\{\mathbf{w}^H\mathbf{Q}\mathbf{w}\right\} \\ &= \max\mathrm{eig}\left\{\mathbf{Q}\right\}\end{aligned} \tag{5.18}$$

Based on the equations above, an alternative Tx-Rx ABF procedure is proposed, referred to as *beam-refinement*. The procedure is carried out through the following steps:

- **Initialization**: the transmitter beam-pattern is set to $\mathbf{w} = \frac{1}{\sqrt{T}}\mathbf{1}_T$.
- **Forward transmission** (see Figure 5.19): the receiver estimates the aggregate matrix $\mathbf{P}$ and computes $\tilde{\mathbf{c}}$ via eigendecomposition, as in equation 5.16.
- **Feedback transmission** (see Figure 5.20): the transceivers swap role. The transmitter estimates the aggregate matrix $\mathbf{Q}$ and computes $\tilde{\mathbf{w}}$ via eigendecomposition, as in equation 5.18.

The channel estimation blocks in Figures 5.19 and 5.20 are assumed ideal, therefore perfect CSI is available at both communication ends. Furthermore, the channel is assumed to be symmetric. The beam-refinement ABF is simulated with the same simulation setup of the Tx-Rx beam-switching, reported in Table 5.2.

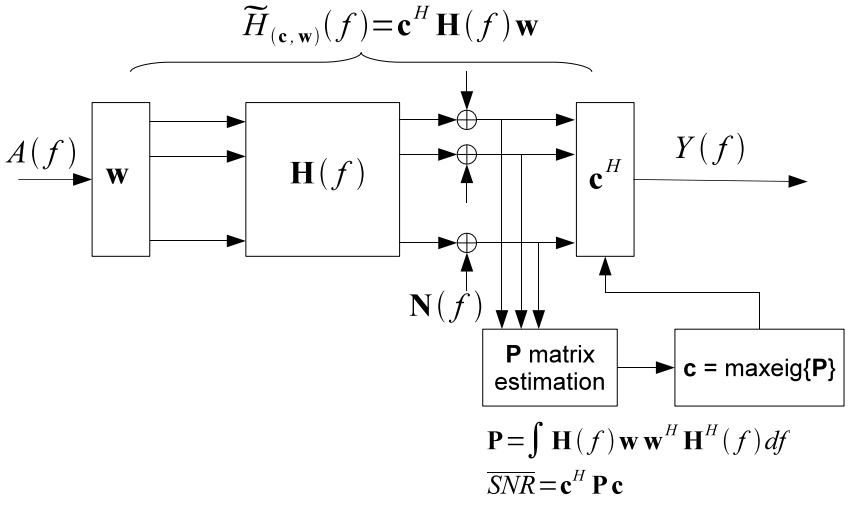

Figure 5.19: Beam-refinement: forward transmission.

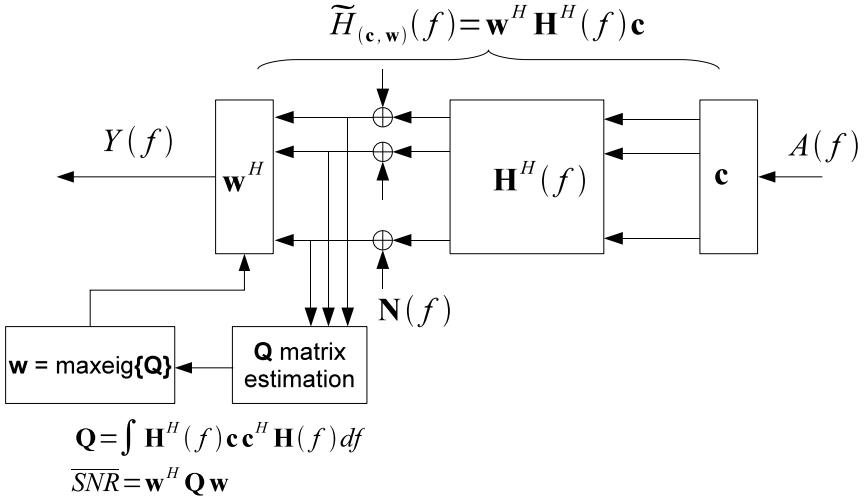

Figure 5.20: Beam-refinement: backward transmission.

The simulation results are presented in Figure 5.21 in terms of beamforming gain and average spectral efficiency and compared to the performance of the Tx-Rx ABF based on beam-switching. It is clearly seen that the beam-refinement ABF yields improved performance with respect to the Tx-Rx beam-switching. This is most

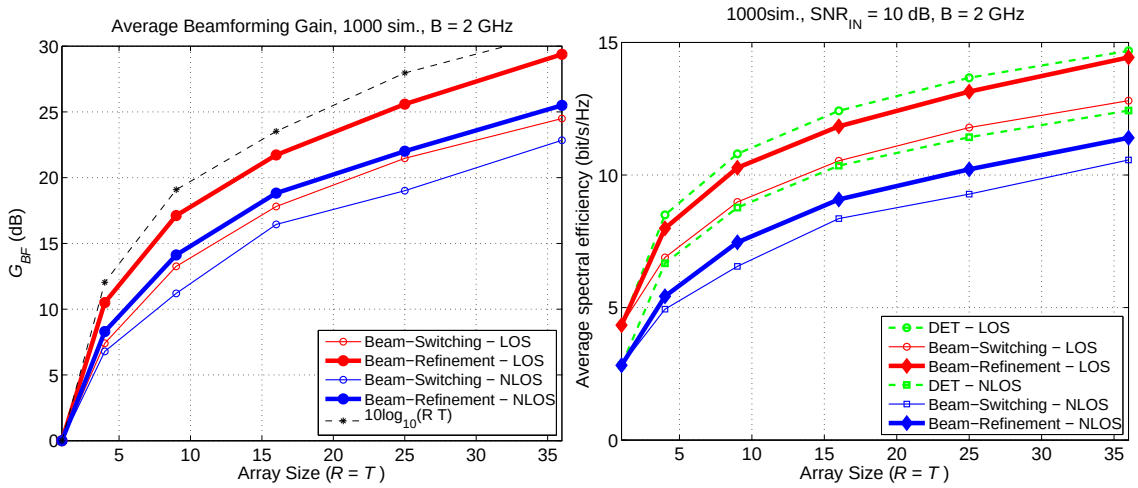

(a) Beamforming gain.

(b) Average spectral efficiency.

Figure 5.21: Performance of the ABF scheme based on beam-refinement compared to Tx-Rx beam-switching ABF.

probably due to the fact that the refined beam-vectors are not constrained within a codebook, but are computed so as to adapt to a specific channel realization.

From Figure 5.21a it can be seen that the beam-refinement achieves greater beamforming gain levels. The improvement occurs both for the LOS and NLOS cases and better results are obtained with larger arrays, exactly as for the case Tx-Rx beam-switching ABF. The improvement in terms of average SNR at the receiver output ranges from 3.1 to 4.8 dB for the LOS scenario, respectively for Tx-Rx URAs of size 2×2 and 6×6. In the NLOS environment the increase in beamforming gain is lower, ranging from 1.6 to 2.7 dB. From Figure 5.21a it is also seen that the beam-refinement ABF achieves performance levels closer to the theoretical array gain. Furthermore, the values of beamforming gain attained by the beam-refinement ABF are quasi-optimal: the SNR penalty with respect to DET beamforming can be as low as 1 dB for the LOS case and 3 dB for the NLOS case[13]. The same conclusions can be drawn from Figure 5.21b, where the results in terms of average spectral efficiency are presented. The beam-refinement attains quasi-optimal performance levels for the LOS case and exhibits a consistent improvement with respect to the beam-switching ABF in the NLOS scenario.

The simulation results of Figure 5.21 show that the beam-switching scheme can be outperformed by overcoming its quantized spatial resolution, that is the Tx-Rx beam-vectors are properly computed instead of selected from the beam-vector codebook. Moreover, the procedure duration is also reduced in the beam-refinement ABF: the entire procedure takes always three steps regardless of the array size. Nevertheless, the beam-refinement scheme does not come free from drawbacks. In-

[13]The SNR penalty of the beam-switching ABF with respect to optimal DET beamforming was derived in Section 5.3.4.

deed, from the block schemes of Figures 5.19 and 5.20 it can be seen that the estimation of the aggregate matrices $\mathbf{P}$ and $\mathbf{Q}$ is very challenging since it has to be performed before the combiner, i.e. at RF level. This feature is a major problem, and makes the beam-refinement technique extremely hard to design in the analog architecture. Hence, in this case it was shown that the increased performance values obtained through a more sophisticated beamforming procedure imply very complex, and therefore costly, design and implementation. Given that the improvement in terms of beamforming gain is less than 5 dB in the best case, i.e. LOS scenario with 6×6 URAs, the beam-refinement scheme can be hardly considered a satisfactory candidate to replace the simpler Tx-Rx ABF procedure based on beam-switching.

5.5 Conclusion

In this chapter, the performance of a Tx-Rx analog beamforming scheme was evaluated on the 60 GHz MIMO channel described in the previous chapter. The considered ABF scheme was based on the average SNR maximization via beam-switching, i.e. the best Tx-Rx beam-vector pair that yields the greatest average SNR is selected among a set of pre-defined Tx and Rx beam-vectors using of an exhaustive search process. The evaluation was carried out by means of Monte Carlo simulations, investigating the impact of the channel type (LOS/NLOS) and of the URA size on the system performance.

The performance parameters were the beamforming gain, the average spectral efficiency and the coherence bandwidth of the beamformed channel. It was seen that the Tx-Rx ABF scheme based on beam-switching improves the SNR of the system and mitigates the channel multipath components. Better results are obtained with large arrays and in the LOS scenario. For the considered scenarios, in the NLOS case the beam-switching ABF exhibited a SNR penalty ranging from 5 dB to 7.5 dB, of which 5 dB are due to the lack of the power of the direct path and the remaining to the lower ABF performance in the NLOS case. The average spectral efficiency was evaluated and compared to that of optimal DET beamforming. The Tx-Rx ABF system was shown to attain performance levels reasonably close to those of optimal DET beamforming (about 6 dB for all scenarios), despite featuring a much reduced complexity.

Finally, an alternative Tx-Rx beamforming solution was investigated, featuring the computation of the Tx-Rx beam-vectors so as to maximize the average SNR. This approach overcomes the quantized spatial resolution of the beam-switching ABF scheme, and it was shown to attain improved performance levels (quasi-optimal for the LOS case). However, it was also noticed that this refined approach is hardly suitable to the analog implementation, and it introduces a large amount of design and computational complexity.

Lastly, the investigation indicated that the Tx-Rx ABF scheme based on beam-switching constitutes a valid cost-performance trade-off for the considered 60 GHz channel model and array structures, and within the class of analog beamforming.

6 Final Conclusions

The goal of this thesis work was the evaluation of the performance of a joint transmit-receive Analog BeamForming (ABF) solution for the 60 GHz channel. The considered ABF scheme was based on the maximization of the average output SNR by means of Tx-Rx beam-switching. An orthogonal beam-vector codebook was proposed for the beam-switching. The main contributions of the thesis are the following:

- Evaluation of the joint Tx-Rx ABF scheme based on beam-switching over a 60 GHz MIMO channel in terms of beamforming gain, coherence bandwidth and average spectral efficiency;
- Analysis of the impact on the system performance of the array size (for URA geometries) and of the channel type (LOS/NLOS);
- Development of a MIMO Semi-Deterministic Channel Model (SDCM) for 60 GHz indoor propagation based on a combination of ray-tracing and of the available statistical characterization (instrumental to the beamforming evaluation).

The investigation produced the following principal results:

- The Tx-Rx ABF scheme based on beam-switching effectively counters the increased path loss of 60 GHz systems by introducing beamforming gain. Greater performance levels are attained using large arrays and in the LOS scenario;
- Within the class of analog beamforming, and for the considered channel model and array structures, the Tx-Rx ABF scheme based on beam-switching constitutes a valid cost-performance trade-off. The performance penalty with respect to optimal Dominant Eigenmode Transmission (DET) beamforming was shown to be reasonably small, while the computational and design complexity of the beam-switching ABF scheme is much lower.
- The Tx-Rx beam-switching ABF scheme exhibits similar performance trends for the LOS and NLOS cases, featuring a scale-factor in the latter case due to the absence of the direct path.

Future Work

The joint Tx-Rx beamforming evaluation presented in this thesis leaves space for a few continuation possibilities, such as the following:

- The performance penalty due to non-ideal channel estimation should be investigated;

- Time-variant channel models should be introduced, including also the effects of human activity within the propagation environment;
- Realistic antenna-arrays could be evaluated by introducing a model for the single antenna element.

Appendix A: Channel Simulator

This appendix provides a detailed description of some aspects of the semi-deterministic channel model (SDCM) presented in Chapter 4. The structure is the following:

- Geometrical-optics tool;
- DoD-DoA calculation;
- MIMO matrix calculation;
- Simulation set-up for the comparison with the NICT measurements.

Geometrical-Optics Tool

In order to calculate the DoD-DoA correspondence, a simple geometrical-optics tool was developed in Matlab. The propagation environment used in the model is a simple empty room of size $L \times W \times H$ (length × width × height), with no objects, furnitures, windows, or doors (see Figure A1). Neglecting reflections of order higher

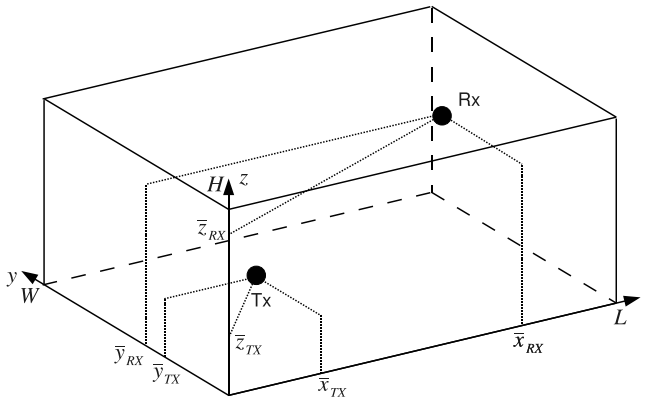

Figure A1: Simulation environment. For the TG3c "Residential room" environment, the room size is 6.85 × 3.57 × 2.47 m.

than the second[1] there are 18 clusters: 1 direct path, 4 first-order reflections from the walls, 1 first-order reflection from the ceiling, 4 second-order reflections from opposite walls, 4 second-order reflections from adjacent walls and 4 second-order reflections from wall-to-ceiling bounces.

Each one of these rays is modeled in the Matlab tool. The (x, y, z) coordinates of each reflection point are calculated given the 3-D positions of the transceivers by

[1] And neglecting all the clusters reflected by the floor, as in [50], where a table was assumed to block all the rays directed towards the floor.

applying basic geometry and trigonometry. The results of the ray-tracing scripts are illustrated in Figure A2. Once the reflection points are calculated, the length

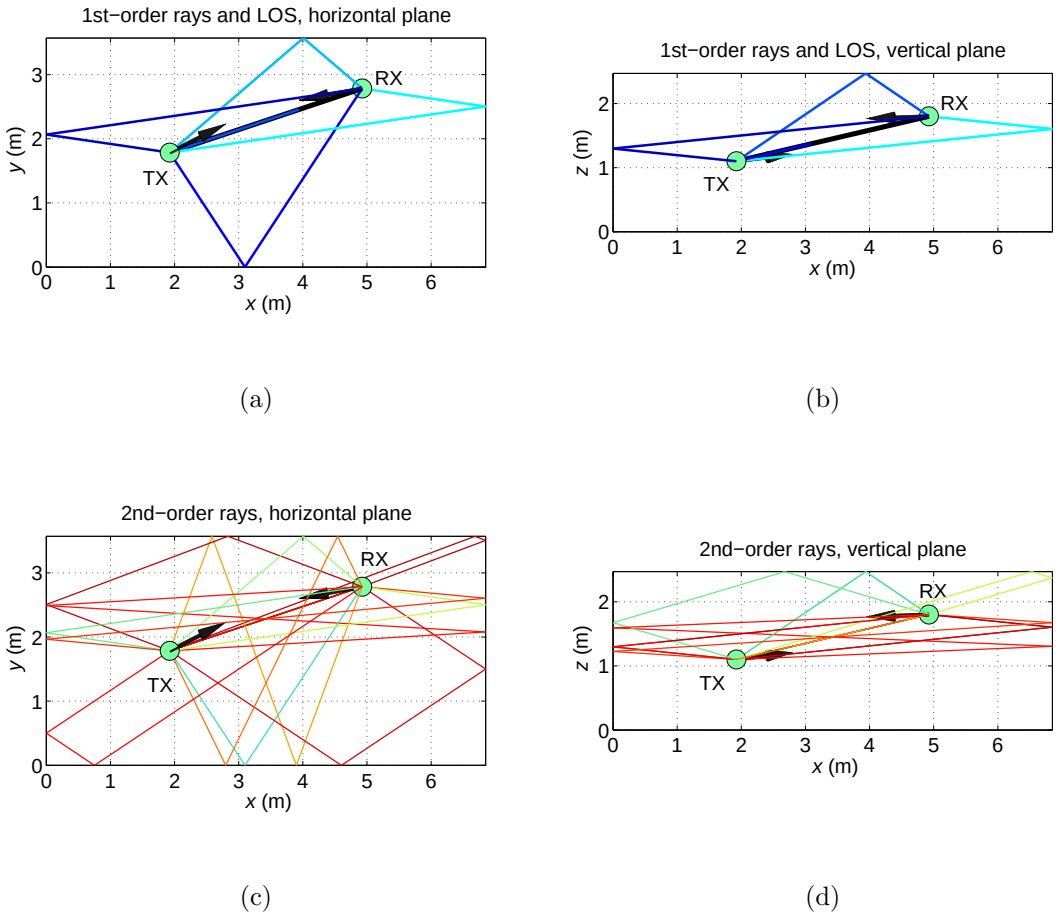

Figure A2: Ray-tracing results. The black thick arrows correspond to the orientation of the transceivers, which is seen not to match the LOS in this simulation.

of each path is readily calculated (Euclidean distance). Assuming a vacuum as the propagation medium (thus isotropic and homogeneous), the times of arrival (ToA) are given by $T^{(i)} = d^{(i)}/c$, $c \approx 3 \cdot 10^8$ m/s.

DoD-DoA Calculation

The DoDs and DoAs must be calculated with respect to the array geometry; as in Figure 3.1 the arrays are assumed to lay on the xy-plane, the MRA direction being the z abscissa. There are three cartesian coordinate systems to be considered: the propagation environment (x, y, z), the Tx array system (x_{TX}, y_{TX}, z_{TX}) and the Rx array system (x_{RX}, y_{RX}, z_{RX}). The relationship between these cartesian systems is illustrated in Figure A3. Since the transceivers are allowed to vary their orientation,

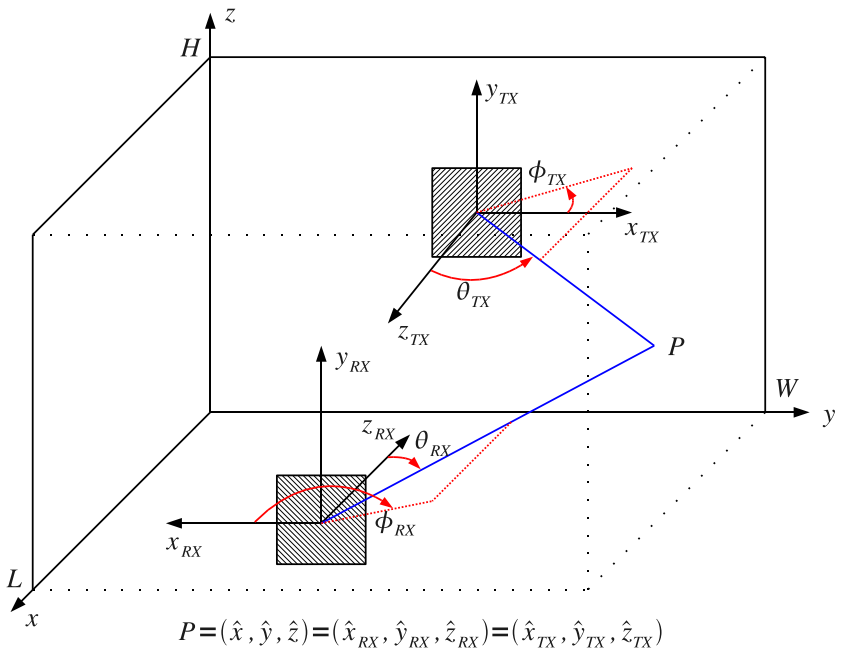

Figure A3: Tx and Rx cartesian subsystems.

the array coordinate systems can rotate horizontally and tilt vertically. In order to calculate the departure/arrival angles, the cartesian coordinates of each reflection point must be translated into the rotated Tx/Rx cartesian system. For a received ray reflected in P (see Figure A3), this is achieved in the following steps:
- obtain the cartesian coordinates of P w.r.t. the un-rotated Rx array: $(\hat{x},\hat{y},\hat{z}) \leftrightarrow (\hat{x}_{RX},\hat{y}_{RX},\hat{z}_{RX})$;
- rotate the Rx coordinate system: rotation occurs on the $x_{RX}z_{RX}$ plane, tilting along $y_{RX}z_{RX}$. Hence, $(x_{RX},y_{RX},z_{RX}) \leftrightarrow (x'_{RX},y'_{RX},z'_{RX})$;
- calculate the cartesian coordinates of P w.r.t. the rotated Rx system: $(\hat{x}_{RX},\hat{y}_{RX},\hat{z}_{RX}) \leftrightarrow (\hat{x}'_{RX},\hat{y}'_{RX},\hat{z}'_{RX})$;
- convert the cartesian coordinates into spherical coordinates.

MIMO Matrix Calculation

The outcomes of the SDCM Matlab tool are grouped in a structure defined as shown in Table A1.

The pseudo-code to generate a realization of the MIMO channel matrix is the following:

```
% SDCM
geo = geometry_setup; % room geometry, Tx and Rx position/orientation
RT = ray_tracing(geo); % deterministic part via geometrical optics
ch  = add_statistics(RT); % statistical part and clustering
```

Table A1: Structured outcomes of the SDCM.

`ch.toa`	$N_R \times 1$ ToA vector
`ch.DoD`	$N_C \times 2^2$ DoD vector
`ch.DoA`	$N_R \times 2$ DoA vector
`ch.amp`	$N_R \times 1$ complex-valued amplitudes vector

```
% defining frequency axis
f_step = 0.01; % frequency-resolution
f = 59:f_step:61-f_step; % 2 GHz bandwidth
Nc = length(f); % number of tones

% generating MIMO matrix
Vtx = steering_matrix(ch.DoD); % Tx steering matrix (T x N_c)
Vrx = steering_matrix(ch.DoA); % Rx steering matrix (R x N_r)
for i = 1:Nc
B = fading_matrix(ch.amp, ch.toa, f(i)); % fading-matrix (R x T)
H(i,:,:) = Vrx * B * Vtx';
end
```

Simulation Setup for the SDCM Accuracy Assessment

In Section 4.2.2 the results of the SDCM were compared to the measurements collected by the NICT in the IEEE TG3c "Residential room" environment [52]. In order to compare the outcomes properly, the experiment setup and the adopted conventions must be equal in both cases.

The propagation environment used by the NICT to collect channel measurements is shown in Figure A4. In the SDCM, the geometry was reduced to an empty room of the same size with no furniture, objects, windows or doors. The 3-D positions of the transceivers are equal in both experiments[3]. In the NICT measurement set-up, the transmitter is an omni-directional radiator, while the receiver is a horn-antenna with 15° HPBW in the vertical and horizontal planes. In order to compare the simulation results properly, an Rx antenna with similar characteristics must be applied to the outcomes of the SDCM[4]. Figure A5 compares the beam-pattern of the horn antenna employed by the NICT with the beam-pattern of the "virtual" antenna designed in Matlab to filter the SDCM results.

Finally, it should be noted that the NICT adopted a different convention than the

[3]The vertical coordinates of the transceiver are both 1.1 m [52].

[4]The outcomes of the SDCM are perfect impulses (Dirac delta-functions) in the time and angular domains. Since these delta-functions are measured (and thus filtered) with an equipment of finite bandwidth and spatial resolution, the results are "stretched" in the two domains.

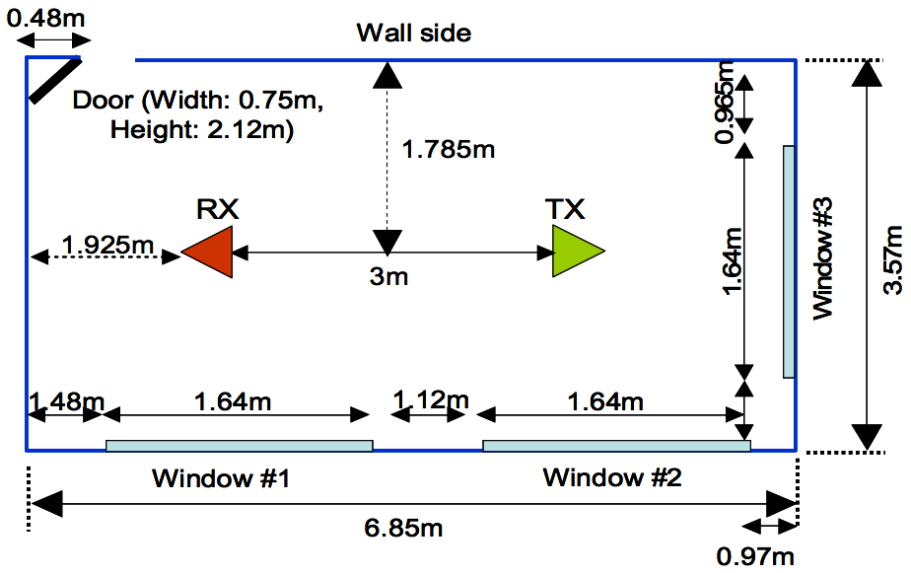

Figure A4: Residential environment used by the NICT for channel measurements (©IEEE 2007).

one used in this dissertation. Indeed, the NICT defines the azimuth as the angle on the zx plane of Figure 3.1, which differs from the definition of azimuth in a standard spherical coordinate system. The outcomes of the SDCM were modified so as to match the convention adopted by the NICT, in order to provide a proper comparison of the results. Nevertheless, in the rest of the thesis, the definition of azimuth and elevation corresponds to the standard spherical system of Figure 3.1.

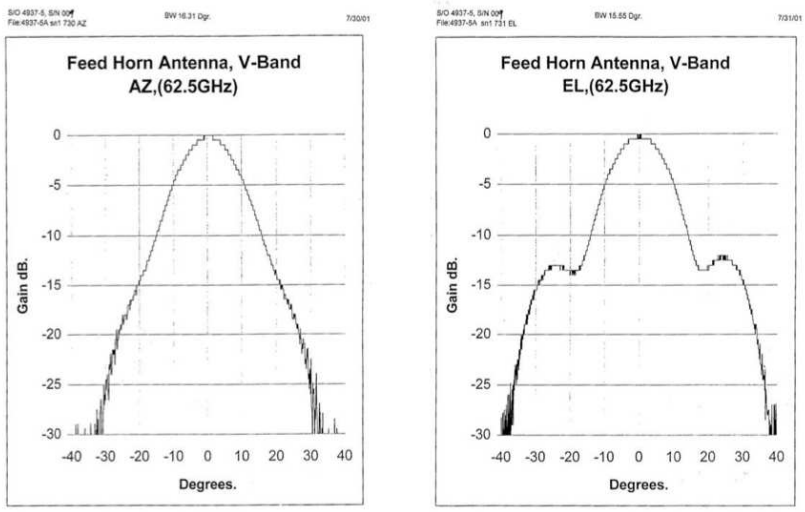

(a) NICT antenna beam-patterns (©IEEE 2007).

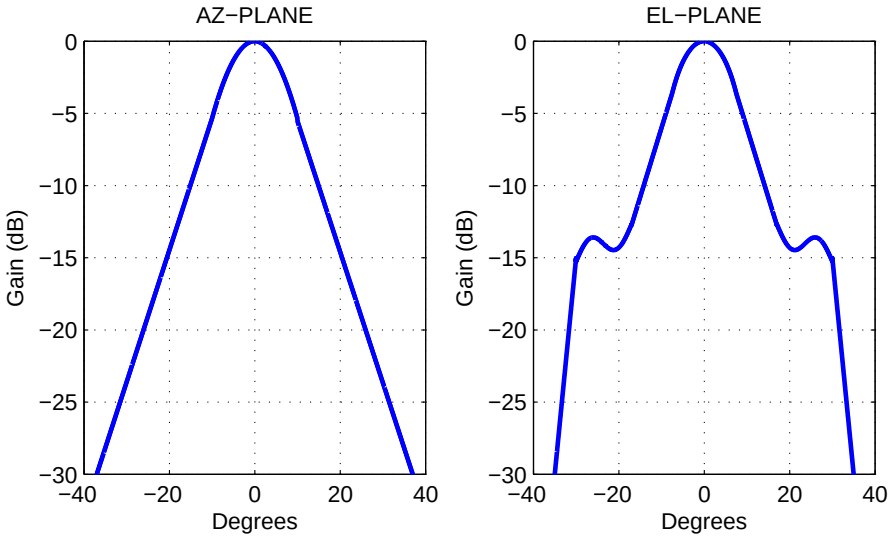

(b) Virtual antenna beam-patterns.

Figure A5: NICT antenna patterns vs. virtual antenna patterns.

Appendix B: Forming Beam-vector Codebooks

This appendix provides a mathematical description on how to define orthogonal beam-vector codebooks for URAs. For a more detailed presentation, including other array geometries, the reader is addressed to [34].

In [34] it is reported that a N-element standard Uniform Linear Array (ULA) can produce N orthogonal beams equally spaced in the direction cosine domain. For this array geometry, the steering vector in the direction cosine domain is defined as follows (see Section 3.2.1):

$$\mathbf{v}_u(u_s) = \begin{bmatrix} e^{j2\pi p_0 u_s} \\ \vdots \\ e^{j2\pi p_{N-1} u_s} \end{bmatrix}, \quad p_n = \left(n - \frac{N-1}{2}\right) d, \quad n = 0, \ldots, N-1 \tag{B1}$$

where u_s is the pointing direction, d the inter-element spacing (equal to $\lambda_0/2$) and p_n the position of the n-th element along the alignment abscissa. The central weight-vector corresponds to the beam-pattern pointing at broadside ($u_s = 0$):

$$\mathbf{w}_0 = \frac{1}{\sqrt{N}}\mathbf{v}_u(0) = \frac{1}{\sqrt{N}}\mathbf{1}_N \tag{B2}$$

The remaining $N-1$ beam-vectors are shifted versions of (B2) by $2m/N$:

$$\mathbf{w}_m = \frac{1}{\sqrt{N}}\mathbf{v}_u\left(\frac{2m}{N}\right), \quad m = -\frac{N}{2}+1, \ldots, \frac{N}{2} \qquad N \text{ even} \tag{B3}$$

$$\mathbf{w}_m = \frac{1}{\sqrt{N}}\mathbf{v}_u\left(\frac{2m}{N}\right), \quad m = -\frac{N-1}{2}, \ldots, \frac{N-1}{2} \qquad N \text{ odd} \tag{B4}$$

The pointing direction of the m-th beam-pattern occurs at $2m/N$, and all other beams have nulls at that point. This occurs because the weight vectors are orthogonal:

$$\mathbf{w}_m^H \mathbf{w}_l = \begin{cases} 1 & m = l \\ 0 & m \neq l \end{cases} \tag{B5}$$

Therefore, for a N-element standard linear array, the beam-vector codebook is given by

$$\mathcal{W} = \begin{cases} [\mathbf{w}_{-N/2+1}, \ldots, \mathbf{w}_0, \mathbf{w}_{N/2}] & N \text{ even} \\ [\mathbf{w}_{-(N-1)/2}, \ldots, \mathbf{w}_0, \mathbf{w}_{(N-1)/2}] & N \text{ odd} \end{cases} \tag{B6}$$

and has dimension $N \times N$. It can be proved that the resulting matrix has a Fourier structure [34].

This concept can be readily extended to the case of URA. Let us consider the case of an $N \times M$ standard URA laying on the xy-plane, as illustrated in Figure 3.1.

For this geometry, we can first decompose the rectangular array into two standard linear arrays: one laying on the x-abscissa with N elements and one laying on the y abscissa with M elements. The first linear arrays features N orthogonal pointing directions spaced by $2/N$, denoted with u_n, while the latter has M orthogonal look-directions u_m with displacement $2/M$. The weight-vector corresponding to the pointing direction (u_n, u_m) is given by the following expression:

$$\mathbf{w}_{n,m} = \text{vec}\left(\mathbf{w}_m \mathbf{w}_n^T\right) \tag{B7}$$

where the vec$(\cdot)$ operator creates a column vector from a matrix by stacking its column vectors below one another. Thus, for a NM-element URA there are NM orthogonal beam-vectors, and the codebook is given by:

$$\mathcal{W} = \begin{cases} \left[\mathbf{w}_{-N/2+1,-M/2+1}, \ldots, \mathbf{w}_{-N/2+1,M/2}, \ldots, \mathbf{w}_{N/2,M/2}\right] & N \text{ and } M \text{ even} \\ \left[\mathbf{w}_{-N-1/2,-M/2+1}, \ldots, \mathbf{w}_{-(N-1)/2,M/2}, \ldots, \mathbf{w}_{(N-1)/2,M/2}\right] & N \text{ odd}, M \text{ even} \\ \left[\mathbf{w}_{-N/2+1,-(M-1)/2}, \ldots, \mathbf{w}_{-N/2+1,(M-1)/2}, \ldots, \mathbf{w}_{N/2,(M-1)/2}\right] & N \text{ even}, M \text{ odd} \\ \left[\mathbf{w}_{-(N-1)/2,-(M-1)/2}, \ldots, \mathbf{w}_{-(N-1)/2,(M-1)/2}, \ldots, \mathbf{w}_{(N-1)/2,(M-1)/2}\right] & N \text{ and } M \text{ odd} \end{cases} \tag{B8}$$

The dimension of the codebook for a NM-element URA is therefore $NM \times NM$, and it can be proved that $\mathcal{W}$ has a Fourier structure [34].

In the following pages, Figures B1 through B5 illustrate the beam-pattern cuts on the horizontal plane for the URA structures considered in this thesis.

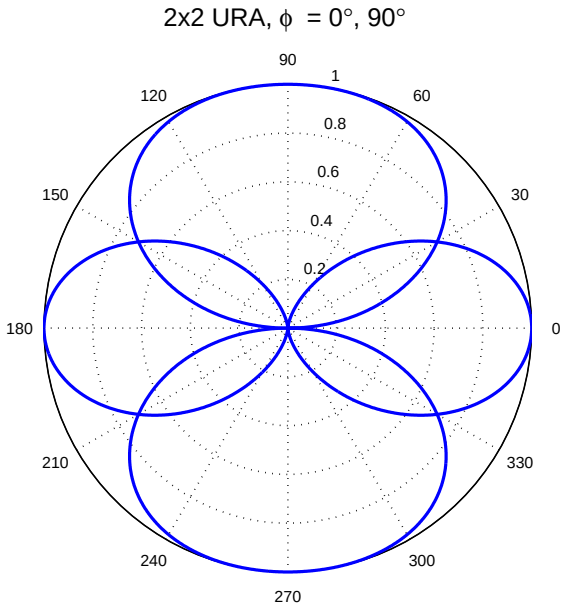

Figure B1: Beam-pattern codebook for a 2×2 URA (pattern cut).

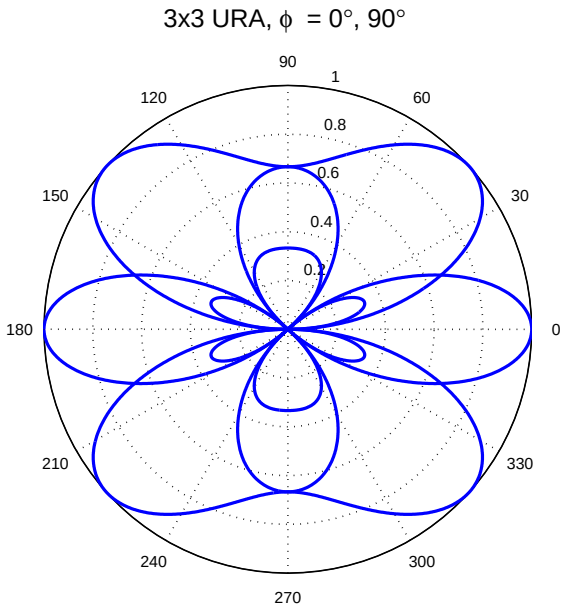

Figure B2: Beam-pattern codebook for a 3×3 URA (pattern cut).

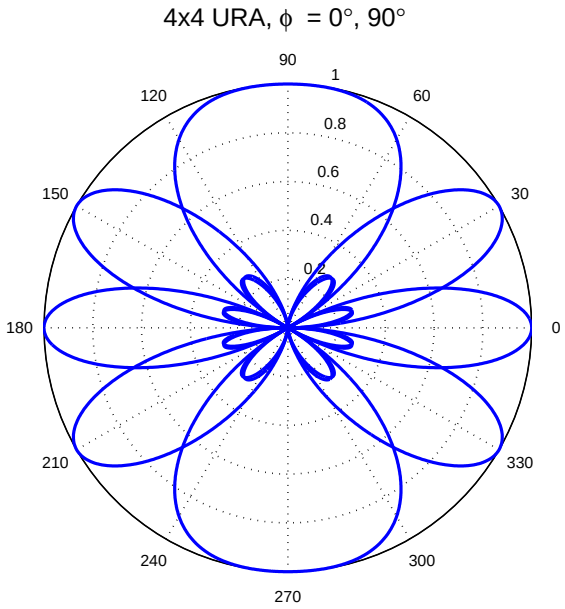

Figure B3: Beam-pattern codebook for a 4×4 URA (pattern cut).

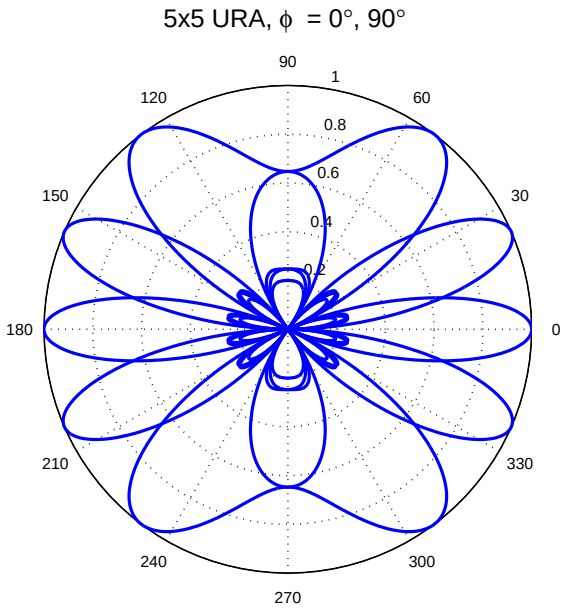

Figure B4: Beam-pattern codebook for a 5×5 URA (pattern cut).

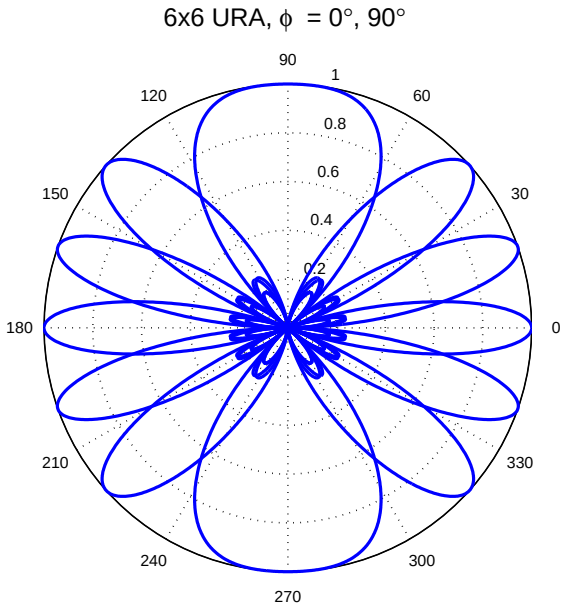

Figure B5: Beam-pattern codebook for a 6×6 URA (pattern cut).

References

[1] P. Smulders, "Exploiting the 60 GHz band for local wireless multimedia access: prospects and future directions," *IEEE Communications Magazine*, vol. 40, no. 1, pp. 140–147, Jan 2002.

[2] S. K. Yong and C.-C. Chong, "An overview of multigigabit wireless through millimeter wave technology: potentials and technical challenges," *EURASIP J. Wirel. Commun. Netw.*, vol. 2007, no. 1, pp. 50–50, 2007.

[3] R. Daniels and R. Heath, "60 GHz wireless communications: emerging requirements and design recommendations," *IEEE Vehicular Technology Magazine*, vol. 2, no. 3, pp. 41–50, Sept. 2007.

[4] M. Peter, W. Keusgen, and J. Luo, "A survey on 60 GHz broadband communication: Capability, applications and system design," in *European Microwave Integrated Circuit Conference, 2008. EuMIC 2008*, Oct. 2008, pp. 1–4.

[5] F. Giannetti, M. Luise, and R. Reggiannini, "Mobile and personal communications in the 60 GHz band: A survey," *Wirel. Pers. Commun.*, vol. 10, no. 2, pp. 207–243, 1999.

[6] J. Nsenga, W. Van Thillo, F. Horlin, V. Ramon, A. Bourdoux, and R. Lauwereins, "Joint transmit and receive analog beamforming in 60 GHz MIMO multipath channels," in *IEEE International Conference on Communications, 2009. ICC '09*, June 2009, pp. 1–5.

[7] H. H. Pham, T. Taniguchi, and Y. Karasawa, "MIMO beamforming for high-bit-rate transmission over frequency-selective fading channels," in *IEEE Eighth International Symposium on Spread Spectrum Techniques and Applications, 2004*, Aug.-2 Sept. 2004, pp. 275–279.

[8] A. Seyedi, "On the capacity of wideband 60GHz channels with antenna directionality," in *IEEE Global Telecommunications Conference, 2007. GLOBECOM '07.*, Nov. 2007, pp. 4532–4536.

[9] A. Pollok, W. Cowley, and I. Holland, "Multiple-input multiple-output options for 60 GHz line-of-sight channels," in *Australian Communications Theory Workshop, 2008. AusCTW 2008*, 30 2008-feb. 1 2008, pp. 101 –106.

[10] T. Zhang and A. Manikas, "Joint transmitter-receiver beamforming over space-time fading channels," in *IEEE International Conference on Communications, 2007. ICC '07.*, June 2007, pp. 4913–4918.

[11] H. Zhang and T. Gulliver, "On the capacity of 60 GHz wireless communications," in *Canadian Conference on Electrical and Computer Engineering, 2009. CCECE '09*, May 2009, pp. 936–939.

[12] A. Arvanitis, G. Anagnostou, N. Moraitis, and P. Constantinou, "Capacity study of a multiple element antenna configuration in an indoor wireless channel at 60 GHz," in *IEEE 65th Vehicular Technology Conference, 2007. VTC2007-Spring.*, april 2007, pp. 609 –613.

[13] A. Saleh and R. Valenzuela, "A statistical model for indoor multipath propagation," *IEEE Journal on Selected Areas in Communications*, vol. 5, no. 2, pp. 128–137, Feb 1987.

[14] S.-K. Yong, "TG3c channel modeling sub-committee final report," Mar 2007, IEEE P208.15 Working Group for Wireless Personal Area Networks (WPANs). [Online]. Available: https://mentor.ieee.org/802.15/documents

[15] L. Boucher, "Frequency allocations and regulations in the 50-to-70-GHz band," in *Asia-Pacific Microwave Conference*, 2000, pp. 116–119.

[16] "IEEE standard for information technology - telecommunications and information exchange between systems - local and metropolitan area networks - specific requirements. part 15.3: Wireless medium access control (MAC) and physical layer (PHY) specifications for high rate wireless personal area networks (WPANs) Amendment 2: Millimeter-wave-based alternative physical layer extension," *IEEE Std 802.15.3c-2009 (Amendment to IEEE Std 802.15.3-2003)*, pp. c1–187, 12 2009.

[17] A. Straiton, "The absorption and reradiation of radio waves by oxygen and water vapor in the atmosphere," *IEEE Transactions on Antennas and Propagation*, vol. 23, no. 4, pp. 595–597, Jul 1975.

[18] P. Smulders, H. Yang, and I. Akkermans, "On the design of low-cost 60-GHz radios for multigigabit-per-second transmission over short distances [topics in radio communications]," *IEEE Communications Magazine*, vol. 45, no. 12, pp. 44–51, December 2007.

[19] [Online]. Available: http://www.rfcafe.com/references/electrical/atm-absorption.htm

[20] C. Anderson and T. Rappaport, "In-building wideband partition loss measurements at 2.5 and 60 GHz," *IEEE Transactions on Wireless Communications*, vol. 3, no. 3, pp. 922–928, May 2004.

[21] C. Anderson, T. Rappaport, K. Bae, A. Verstak, N. Ramakrishnan, W. Tranter, C. Shaffer, and L. Watson, "In-building wideband multipath characteristics at 2.5 and 60 GHz," in *IEEE 56th Vehicular Technology Conference, 2002. Proceedings. VTC 2002-Fall. 2002*, vol. 1, 2002, pp. 97–101 vol.1.

[22] K. Siwiak, "Through wall propagation up to 60 GHz band," TimeDerivative, 10988 NW 14th Street, Coral Springs FL 33071, Tech. Rep., Aug 2006, doc. IEEE 802.15-06-0371-00-003c. [Online]. Available: http://mentor.ieee.org/802.15/documents/

[23] J. Laskar, S. Pinel, D. Dawn, S. Sarkar, P. Sen, B. Perunama, D. Yeh, and F. Barale, "60GHz entertainment connectivity solution," in *IEEE International Conference on Ultra-Wideband, 2009. ICUWB 2009*, Sept. 2009, pp. 17–21.

[24] B. Floyd, S. Reynolds, U. Pfeiffer, T. Beukema, J. Grzyb, and C. Haymes, "A silicon 60GHz receiver and transmitter chipset for broadband communications," in *IEEE International Solid-State Circuits Conference, 2006. ISSCC 2006. Digest of Technical Papers.*, Feb. 2006, pp. 649–658.

[25] S. Pinel, S. Sarkar, P. Sen, B. Perunama, D. Yeh, D. Dawn, and J. Laskar, "A 90nm CMOS 60 GHz radio," *ISSCC 2008, Digest of Technical Papers*, pp. 130–601, Feb. 2008.

[26] H. Friis, "A note on a simple transmission formula," *Proceedings of the IRE*, vol. 34, no. 5, pp. 254–256, May 1946.

[27] S. Collonge, G. Zaharia, and G. Zein, "Influence of the human activity on wideband characteristics of the 60 GHz indoor radio channel," *IEEE Transactions on Wireless Communications*, vol. 3, no. 6, pp. 2396–2406, Nov. 2004.

[28] H. Hashemi, "The indoor radio propagation channel," *Proceedings of the IEEE*, vol. 81, no. 7, pp. 943–968, Jul 1993.

[29] J. Proakis, *Digital Communications (5th International Edition)*, 5th ed. McGraw-Hill, 2008.

[30] H. Singh, S.-K. Yong, J. Oh, and C. Ngo, "Principles of IEEE 802.15.3c: Multi-gigabit millimeter-wave wireless PAN," in *Proceedings of 18th International Conference on Computer Communications and Networks, 2009. ICCCN 2009*, Aug. 2009, pp. 1–6.

[31] [Online]. Available: http://www.wirelesshd.org

[32] ECMA TC48 - high rate wireless communications. [Online]. Available: http://www.ecma-international.org/memento/TC48-M.htm

[33] [Online]. Available: http://wirelessgigabitalliance.org/specifications/

[34] H. L. V. Trees, *Optimum Array Processing (Detection, Estimation, and Modulation Theory, Part IV)*, 1st ed. Wiley-Interscience, 3 2002.

[35] L. C. Godara, *Smart Antennas (Electrical Engineering & Applied Signal Processing Series)*, 1st ed. CRC, 1 2004.

[36] P. S. Naidu, *Sensor Array Processing*. Boca Raton, FL, USA: CRC Press, Inc., 2009.

[37] Balanis C., *Antenna Theory: Analysis and Design*, 2nd ed. Wiley, 1996.

[38] H. Yang, P. Smulders, and M. Herben, "Frequency selectivity of 60-GHz LOS and NLOS indoor radio channels," in *IEEE 63rd Vehicular Technology Conference, 2006. VTC 2006-Spring.*, vol. 6, May 2006, pp. 2727–2731.

[39] K. Sayrafian, B. Neekzad, J. Perez, and J. Baras, "Ray-tracing simulation of the NICT indoor channel measurements," National Institute of Standard and Technology (NICT), Tech. Rep., Jul 2006. [Online]. Available: http://mentor.ieee.org/802.15/documents

[40] A. Maltsev, R. Maslennikov, A. Sevastyanov, A. Khoryaev, and A. Lomayev, "Experimental investigations of 60 GHz WLAN systems in office environment," *IEEE Journal on Selected Areas in Communications*, vol. 27, no. 8, pp. 1488–1499, October 2009.

[41] H. Yang, P. F. M. Smulders, and M. H. A. J. Herben, "Channel characteristics and transmission performance for various channel configurations at 60 GHz," *EURASIP J. Wirel. Commun. Netw.*, vol. 2007, no. 1, pp. 43–43, 2007.

[42] N. Moraitis and P. Constantinou, "Indoor channel measurements and characterization at 60 GHz for wireless local area network applications," *IEEE Transactions on Antennas and Propagation*, vol. 52, no. 12, pp. 3180–3189, Dec. 2004.

[43] K. Sato, T. Manabe, T. Ihara, H. Saito, S. Ito, T. Tanaka, K. Sugai, N. Ohmi, Y. Murakami, M. Shibayama, Y. Konishi, and T. Kimura, "Measurements of reflection and transmission characteristics of interior structures of office building in the 60-GHz band," *IEEE Transactions on Antennas and Propagation*, vol. 45, no. 12, pp. 1783–1792, Dec 1997.

[44] J. Kunisch, E. Zollinger, J. Pamp, and A. Winkelmann, "MEDIAN 60 GHz wideband indoor radio channel measurements and model," in *IEEE VTS 50th Vehicular Technology Conference, 1999. VTC 1999 - Fall*, vol. 4, 1999, pp. 2393–2397 vol. 4.

[45] S. Collogne, G. Zaharia, and G. El Zein, "Experimental investigation of the spatial and temporal characteristics of the 60 GHz radio propagation within residential environments," in *International Symposium on Signals, Circuits and Systems, 2003. SCS 2003*, vol. 2, July 2003, pp. 417–420 vol. 2.

[46] H. Xu, V. Kukshya, and T. Rappaport, "Spatial and temporal characteristics of 60-GHz indoor channels," *IEEE Journal on Selected Areas in Communications*, vol. 20, no. 3, pp. 620–630, Apr 2002.

[47] P. Almers, E. Bonek, A. Burr, N. Czink, M. Debbah, V. Degli Esposti, H. Hofstetter, P. Kyösti, D. Laurenson, G. Matz, A. F. Molisch, C. Oestges, and H. Özcelik, "Survey of channel and radio propagation models for wireless MIMO systems," *EURASIP Journal on Wireless Communications and Networking*, vol. 2007, pp. 1–19, 2007.

[48] Q. Spencer, B. Jeffs, M. Jensen, and A. Swindlehurst, "Modeling the statistical time and angle of arrival characteristics of an indoor multipath channel," *IEEE Journal on Selected Areas in Communications*, vol. 18, no. 3, pp. 347–360, Mar 2000.

[49] W. Peter, W. Keusgen, and R. Felbecker, "Measurement and ray-tracing simulation of the 60 GHz indoor broadband channel: Model accuracy and parameterization," in *The Second European Conference on Antennas and Propagation, 2007. EuCAP 2007*, nov. 2007, pp. 1–8.

[50] A. Maltsev, "Channel models for 60 GHz WLAN systems," May 2009, doc. IEEE 802.11-09/0334r2. [Online]. Available: https://mentor.ieee.org/802.11/documents

[51] H. Özcelik, N. Czink, E. Bonek, and T. U. Wien, "What makes a good MIMO channel model," in *Vehicular Technology Conference, 2005*, 2005, pp. 156–160.

[52] B. Neekzad, K. Sayrafian-Pour, J. Perez, and J. Baras, "Comparison of ray tracing simulations and millimeter wave channel sounding measurements," in *IEEE 18th International Symposium on Personal, Indoor and Mobile Radio Communications, 2007. PIMRC 2007*, sept. 2007, pp. 1–5.

[53] A. Sayeed, "Deconstructing multiantenna fading channels," *IEEE Transactions on Signal Processing*, vol. 50, no. 10, pp. 2563–2579, Oct 2002.

[54] H. Krim and M. Viberg, "Two decades of array signal processing research: the parametric approach," *IEEE Signal Processing Magazine*, vol. 13, no. 4, pp. 67–94, Jul 1996.

[55] S. Imata, M. Nohara, and K. Kashliki, "Study of inter-base station beam switching considering asymmetric broadband transmission in cognitive radio," *IEEE 19th International Symposium onPersonal, Indoor and Mobile Radio Communications, 2008. PIMRC 2008*, pp. 1–6, Sept 2008.

[56] A. Paulraj, R. Nabar, and D. Gore, *Introduction to Space-Time Wireless Communications*. Cambridge University Press, 2003.

[57] I. Santamaría, V. Elvira, J. Vía, D. Ramírez, J. Pérez, J. I. nez, R. Eickhoff, and F. Ellinger, "Optimal MIMO Transmission Schemes with Adaptive Antenna Combining in the RF Path," in *Proceedings of the 16th European Signal Processing Conference (EUSIPCO)*, Lausanne, Switzerland, 25-29 August 2008.

[58] J. Andersen, "Array gain and capacity for known random channels with multiple element arrays at both ends," *IEEE Journal on Selected Areas in Communications*, vol. 18, no. 11, pp. 2172 –2178, nov 2000.